Title
MOCVD Growth Methods to Achieve High-Efficiency Long-Wavelength microLEDs Extending to Red Emission

Author
White, Ryan Christopher

Publication Date
2021

UNIVERSITY OF CALIFORNIA

Santa Barbara

MOCVD Growth Methods To Achieve High-Efficiency Long-Wavelength MicroLEDs Extending To Red Emission

A dissertation submitted in partial satisfaction of the
requirements for the degree Doctor of Philosophy
in Materials

by

Ryan C. White

Committee in charge:
Professor Steven P. DenBaars, Chair
Professor Shuji Nakamura
Professor James S. Speck
Principal Development Engineer Stacia Keller

March 2022

The dissertation of Ryan C. White is approved.

Shuji Nakamura

James S. Speck

Stacia Keller

Steven P. DenBaars, Committee Chair

December 2021

To Gina and Scotch

Partners in Revolution

Acknowledgements

I want to give a special recognition to a few people who have made it possible to even write this dissertation. Many people have sacrificed quite a bit of their time and effort at various points in my life in order to get me to this point, and the influences they've had on me is immeasurable. From my parents and family throughout childhood, science teachers I've had at various points in school, mentors during research, and friends along the way, all have made what would otherwise be impossible into a reality. To my partner Gina, my parents Carolyn and John, my brothers Matthew and Nicholas, my third grade science teacher Mr. Cassell, my undergraduate research advisor at UNC Dr. Scott Warren, the dozens of graduate students I've worked with at UCSB, my research mentor Mike Iza, my thesis advisor Dr. Steve DenBaars, and my thesis committee, thank you. You all made it possible.

VITA OF RYAN CHRISTOPHER WHITE

March 2022

EDUCATION

Bachelor of Science in Chemistry, University of North Carolina, Chapel Hill, May 2017 (magna cum laude)

PUBLICATIONS

"MOCVD Growth Methods To Achieve High-Efficiency Long-Wavelength MicroLEDs Extending To Red Emission ," Unpublished thesis submitted in partial fulfillment of the requirements for the Doctor of Philosophy degree in Materials, University of California, Santa Barbara, 2021. 171 pp.

White, R. C. *et al.* MOCVD growth of thick V-pit-free InGaN films on semi-relaxed InGaN substrates. *Semicond. Sci. Technol.* (2020). doi:10.1088/1361-6641/abc51c

White, R. *et al.* Morphological improvement and elimination of V-pits from long-wavelength all-InGaN based uLEDs grown by MOCVD on compliant substrates. 46 (2021). doi:10.1117/12.2578655

White, R. C. *et al.* Realization of III-Nitride c-Plane microLEDs Emitting from 470 to 645 nm on Semi-Relaxed Substrates Enabled by V-Defect-Free Base Layers. *Crystals* **11**, 1168 (2021).

White, R. C. *et al.* Ingan-based microled devices approaching 1% eqe with red 609 nm electroluminescence on semi-relaxed substrates. *Crystals* **11**, 1–9 (2021).

AWARDS

National Science Foundation: Graduate Research Fellowship Program Recipient, 2017

Ronald E. McNair Scholars Cohort, University of North Carolina: Chapel Hill, 2016

Dialectic and Philanthropic Societies Senator, University of North Carolina: Chapel Hill, 2018

FIELDS OF STUDY

Major Field: Materials Science and Engineering

Studies in Semiconductor Physics with Professor James Speck

Studies in Metal Organic Chemical Vapor Deposition with Professors Steven P. DenBaars and Shuji Nakamura

Abstract

MOCVD Growth Methods to Achieve High-Efficiency Long-Wavelength microLEDs Extending to Red Emission

by

Ryan C. White

Despite the high efficiency and long development time of blue-emitting gallium nitride (GaN)-based μLEDs using metal-organic chemical vapor deposition (MOCVD) growth methods, high-performance devices emitting at the longer visible wavelengths have seen comparatively far less research and investment. Difficulties surrounding the growth of high-In layers by MOCVD makes device improvement increasingly difficult as the wavelength increases, requiring higher In content active regions, causing structural degradation and poor electrical performance. In this work, first higher power and efficiency of green-emitting LEDs is achieved through MOCVD design along with advanced characterization and device physics. Experimental results, modelling, and advanced design are employed in tandem to achieve higher power and lower operating forward voltage. The knowledge generated and advances made in the green LED design are then leveraged into realization of red-emitting InGaN/GaN μLEDs. Few examples of InGaN/GaN devices emitting in the red spectral regime currently exist with only a few realized proof of concept devices. Here, by employing semi-relaxed InGaN substrates, true red μLEDs using an InGaN growth structure can be achieved. Initially, a method to significantly improve material quality from the starting substrate is established, fully eliminating large-scale extended defects known as V-defects initially present in the substrate. On this newly improved material, red-emitting μLED devices with appreciable external quantum efficiency (EQE) can then be realized. Growth conditions in the active region and p-type regions are both thoroughly explored in order to increase light output power of the device and in turn improve EQE. These developments then finally result in realization of a red-emitting device nearing 1% peak EQE.

Preface

III-Nitride LEDs have a rich history, beginning with their discovery almost thirty years ago and leading to a lighting and energy electronics revolution. Since their initial conception, development of blue InGaN/GaN LEDs has led to a wide array of technologies, as well as efficiencies approaching their physical limits. However, green-emitting microLED development has lagged behind their blue counterparts, with red-emitting microLED development all but nonexistent outside a few research groups. While other material system solutions exist for long-wavelength emission, the ability to cover the entire visible spectrum using one material can simplify production and device integration into later products. Especially relevant for RGB applications, efficient long-wavelength emitting LEDs in the green emission region and beyond are in high demand and have seen limited development. Notably, red-emitting III-nitride LEDs have been especially difficult to achieve with appreciable emission, stalling progress toward an RGB system covered by one material system. Here, we hope to change that.

Table of Contents

Chapter 1

Introduction and Background

1.1 Background and Applications

Gallium nitride (GaN) is a direct wide-bandgap (WBG) semiconductor, making it ideal for light output at low wavelength/high energy. Based on its direct-gap band structure with a wide bandgap of 3.4 eV, GaN is a prime material for use in highly efficient solid-state light-emitting diodes (LEDs) and laser diodes (LDs) [1]. This WBG energy corresponds to a light emission of 364 nm, extended slightly beyond the visible spectrum into the shallow ultraviolet (UV) spectrum, but still very close in energy to the blue, high-energy region of the visible light spectrum. In addition to its natural band gap energy being close to the visible spectrum, the band gap of the material can also be continuously narrowed through addition of other group III atoms, notably In to form indium gallium nitride (InGaN) alloys. The resulting InGaN alloy band gap and unit cell lattice parameter is a weighted average of the two pure III-V materials, according to Vegard's Law. For InGaN, the smaller bandgap, larger size indium nitride (InN) unit cell and larger band gap, smaller size GaN unit cell, are averaged together to create an alloy with a smaller band gap but larger lattice constant. As a result, the emission from the InGaN material with the smaller band gap will shift into the visible spectrum and the larger lattice constant will generate some stress and strain from lattice-matching to underlying GaN during growth. As more In is added, both of these effects compound, resulting in longer-wavelength visible emissions with increased stress and strain.

Complications to the growth of GaN and its associated alloys- the already mentioned InGaN alloy along with AlGaN and occasionally InAlGaN- do exist, especially in growth of high alloy-content regions. At high In content such as in the In QW active regions managing generated strain becomes increasingly difficult leading to relaxation. Additionally, higher In leads to morphological issues, such as increased large-scale defect generation and rough, inhomogenous interfaces. However, the material system as a whole has fundamentally high optoelectrical performance and efficiency in the visible spectrum, making overcoming these complications a matter of engineering a more effective growth architecture and process [2]. Since the system will be fundamentally limited by non-native substrate selection, In desorption, strain, and defect generation, the growth conditions can nearly always be improved, especially with using thin film mechanics to overcome issues arising from strain. Similarly, growth of high-In InGaN films also results in a number of detrimental high In effects to the electrical performance as the In mole fraction increases in addition to morphology issues. As the In content increases, the number of nonradiative recombination centers (NRCs) similarly increases as a result of defects like In clustering or impurity incorporation, both of which lead to significantly reduced electrical performance. With lower required In content in the QW, blue-emitting devices have seen widespread applications, where they can be combined with a yellow phosphor to create white lighting sources. Despite highly efficient devices in the blue emission regime, longer wavelength devices in the green regime and beyond suffer from much lower quantum efficiencies and as a result have been employed in a more limited capacity [3]. By overcoming these issues GaN-based light emitting diodes (LEDs) and blue laser diodes (LDs) have been widely applied in display screen technologies, general and automotive illumination, and telecommunications. [4].

1.2 Strain Effects for c-plane GaN

Issues inherent to c-plane InGaN/GaN growth become more pronounced for long-wavelength as In content is increased and results in increased strain. Of the issues in c-plane devices, strain is arguably the most pronounced and significant as it leads to a domino effect of negative consequences. The strain in the crystal lattice induces a polarization, known as a piezoelectric polarization, that drastically affects the electrical performance of devices. The respective positive and negative polarization charges at the top and bottom interfaces causes electron and hole accumulation, respectively, at these interfaces. These charges then create a 2-dimensional electron gas (2DEG) and a corresponding positively charged depletion region at these interface sites, where the charge density is equal to the polarization discontinuity at the interface, compensating the polarization charge [5]. Generally, these regions of high charge density are detrimental to performance by reducing carrier mobility and acting as scattering centers, reducing the electrical efficiency of the devices. Additionally, the sheet carriers themselves create an electric field that alters the electronic structure of the region, leading to a number of secondary effects.

The most notable of these effects is the quantum confined Stark effect (QCSE). An electric field across a semiconductor leads to band bending, separating charges and creating triangular potential barriers in the QW. The QCSE describes the spatial separation of the electron and hole wavefunctions due to this electric field and the opposing signs of charges, leading to reduced electron/hole wavefunction overlap and resulting in decreased radiative recombination rates [6]. For the case of GaN/InGaN structures, an electric field arises from the opposing polarization-generated sheet charges at the QW interfaces [7] and the respective wavefunctions spatially shift toward the majority carrier side. The piezoelectric field can be fully compensated with a reverse bias electric field applied to the device, which can then be photoexcited in order to observe emission free from QCSE. Compared to the device operated in forward bias, in reverse bias the device is blueshifted [6] indicating the forward or zero-bias device possesses a smaller effective band gap. This emission shift represents the “shrinking” of the effective band gap arising from band tilt due to piezoelectric polarization. In effect, the QCSE directly both redshifts and reduces the radiative emission rate of LED devices through spatial separation of charge carriers, requiring higher carrier density to achieve similar radiative emission rates. As an additional second-order consequence of the strain and QCSE, the spatial separation of charges results in carrier screening at moderate to high carrier densities. This entails the creation of an additional "screening" electric field between the spatially separated positive and negative charges that accumulate in the QW regions. This created field then opposes the piezoelectric field, resulting in blue-shifting of the emission wavelength at higher current density [8]. In sum, the mechanical strain generated during epitaxy leads to the QCSE and subsequent carrier screening, with the net effect of a blueshift in the emission with increasing current density.

A combination of strain polarization effects then leads to a droop in efficiency at higher current density. The QW regions themselves are typically highly efficient, as they can be optically pumped and show no efficiency droop [9]. This droop is only seen in forward bias electrical injection, indicating droop is related to transport rather than radiative efficiency. Because of the large QCSE and resulting inefficiency, larger carrier density is required for the same radiative emission intensity. At high carrier density, Auger recombination becomes the dominant recombination mechanism, resulting in an inverse dependence on carrier density for efficiency, causing droop in this regime [8]. Strong polarization fields arising from strain also result in leakage current from electron injection [9] necessitating higher current density for the same emission, which activates the Auger processes. This efficiency droop is the final result of the domino effect of material strain and the resulting polarization. Ultimately, the chain reaction of effects created by strain lead to a significant impact on device efficiency, and these results are further intensified for long-wavelength devices.

In addition to the electronic effects, negative mechanical effects are created by the large and abrupt lattice constant mismatch between the thick GaN buffer and the InGaN epilayer generating a large biaxial compressive stress [10]. To mitigate the issues arising from lattice mismatch, substrates consisting of relaxed InGaN with a larger lattice constant can be employed. Relaxed substrates employ a larger lattice constant compared to GaN, which leads to a reduction in this biaxial compressive stress for the subsequently grown InGaN epilayers, most notably the QWs [11]. During growth, the incorporation efficiency of In in an InGaN alloy steadily decreases with increasing stress and lattice mismatch due to the deformation energy from alloying the In atoms [12, 13, 14]. This reduction in In incorporation efficiency with stress and strain is known as the compositional pulling effect. In the same vein, a reduction in strain directly leads to a higher In incorporation in the InGaN epilayer itself as a result of a reduction in this compositional pulling effect [15]. As further evidence for this effect, a decrease in the measured piezoelectric field at equal In mole fractions can be seen for substrates with relaxed lattice constants compared to conventional ones [16]. Strain reduction from use of relaxed substrates generates comparatively higher crystal quality in the high-In QW, resulting in higher photoluminescence (PL) efficiency than growth on conventional substrates like sapphire [17, 18].

To partially mitigate this strain issue, substrates consisting of relaxed InGaN are being explored, and have been used in a variety of strain-relieving applications previously. These relaxed substrates employ a larger substrate lattice constant, which leads to a smaller lattice mismatch and subsequent reduction in biaxial compressive stress for the InGaN QWs [11]. Stress reduction then leads to higher In incorporation in the active region by reducing the compositional pulling effect [17, 18, 19]. Increasing the In content in the active region while reducing the strain yields a number of advantages, such as QCSE reduction and reduced defect formation, that would result in a better device efficiency for a high-In, long-wavelength device. The advantages of relaxed substrates over conventional growth are critical for long-wavelength LEDs.

1.3 High-Indium Considerations for Material Quality and Device Design

The crystal quality of the alloy suffers with increasing In content due to a variety of issues, notably the large difference between desorption temperature of In and Ga and significant and increasing lattice mismatch between the underlying GaN buffer layer and the InGaN QWs [20]. As a result of the significant difference in desorption temperature, InGaN layers with over 20% In content will have to be grown at a low temperature (LT), resulting in rougher surfaces from generated defects that act as nonradiative recombination centers. Though high In content leads to a reduced effective band gap and the longer wavelength emission desired, it also leads to significant morphological issues that reduce efficiency. The poor structural quality of these high-In layers then significantly hinders the development of efficient long-wavelength emitting devices [21, 22]. Further, high In content InGaN alloys are inherently unstable at commonly employed growth temperatures, resulting in phase separation occuring between the InN and GaN components of the InGaN alloy [23]. This phase separation, especially prevalent in thick layers of InGaN, can be analyzed as preferentially separating into different regimes of In concentration, or more accurately into different strain regimes, as a result of the compositional pulling effect caused by lattice strain [24]. This compositional pulling results in nonlinear band gap variation with In concentration, which can be regarded as a bowing parameter in Vegard's Law.

High growth rates have been shown to incorporate comparatively more In, but the In further segregates into clustered nanostructures as Ga has a longer surface diffusion time, leading to areas of In-rich material. Further, with a fast growth rate, In atoms do not have sufficient time to re-evaporate away from the growth interface as they would with a low growth rate [25]. In clustering and the resulting poor interface diminishes device performance as a result of nonradiative recombination, leading to pockets of extremely high carrier density and sharply reducing performance through efficiency droop [26]. In contrast, during higher temperature growth, In pockets created from lower temperature growth are instead evaporated, creating a much flatter surface with significantly lowered nonradiative recombination. Flat interfaces are preferentially formed at a higher growth temperature due to the higher migration length of Group III materials, allowing the surface to more easily planarize during growth with high temperature (HT) [27]. However, some In fluctuations still occur in the grown InGaN layers as a result of fundamental kinetic differences between Ga and In adatoms [28]. Successful growth of high-quality InGaN material then becomes a balance between using low enough growth temperature for sufficient In inclusion to achieve the desired emission wavelength and high enough temperature for smooth morphology and low defect generation.

It is worth noting that in c-plane growth one can also redshift the emission wavelength at the expense of an EQE penalty by deliberately employing the QCSE [29] or achieve similar effects by using a wide QW [30]. While neither of these solutions are ideal, if the efficiency penalty is less than that of a higher-In device, the QCSE would prove a net gain by maintaining crystal morphology while also achieving longer wavelength emission.

Due to the rapid advancements of micro-light-emitting didoes (μLEDs) for next-generation display applications, significant research attention has been spent on developing full-color μLED displays [31, 32, 3]. Among the three required colors, the use of III-nitride based red μLEDs remains a critical challenge, even though monochromatic III-nitride blue μLEDs have demonstrated remarkable device performances, and green μLEDs have also demonstrated reasonably high performance [33, 34, 35]. As a result, several novel approaches, including quantum-dot color conversion and III-nitride nanorods, have been discussed to realize full-color μLED displays [36, 37, 38, 39]. Recently, there are reports that reveal the possibility of III-nitride red LEDs by employing strain engineering in the active region, and reasonable progress has been achieved in terms of the optical and electrical performance improvements for devices created using this approach [40, 41, 42, 29]. Alternatively, the AlInGaP material system is one of the most mature, developed red emitters, yet it suffers from poor thermal performance and significant efficiency loss due to the high surface recombination as the device dimensions shrink [43].

While semipolar and nonpolar planes have been used to mitigate or negate piezoelectric strain effects by orienting growth away from the polarization direction [44], with demonstrated devices [45], substrate cost and availability issues are exacerbated along with their smaller size leading to a much lower throughput, quite unattractive for commercial applications. Additional growth difficulties and increased sensitivity to growth conditions also lead to a less robust growth process, exacerbating the issues preventing large-scale commercial application for μLEDs. Working examples of long-wavelength green [46] and red [47] InGaN-based LEDs have been previously shown on c-plane grown devices; however, these devices increasingly lag behind their blue counterparts in both power and efficiency with increasing wavelength. Additionally, relatively very little development has occurred for red LEDs after only modest grains in performance [29], owing to its currently low power and efficiency. Growth approaches to improving c-plane device quality have been established: native GaN substrates will significantly reduce defect generation compared to sapphire substrates due to decreased lattice mismatch [48], and growth at higher temperatures, H_2 carrier gas, and NH_3 concentrations will significantly reduce impurity incorporation from growth sources [49]. Unfortunately, while these effects usually yield improvement in their own right, the high cost and small size of GaN substrates prevent their being an effective solution to defect generation. Similarly, the high In content of long-wavelength devices makes high growth temperatures difficult as In will desorb.

Despite these issues inherent to it, c-plane growth on conventional substrates is still a very attractive method for GaN device design despite intrinsic polarizations and their related effects. The widespread availability, relatively large size, and low cost of the substrates required for c-plane growth make the potential for application enormous. Moreover, the strain and polarization physics are reasonably well understood after decades of development, giving significant insight to many initial or conventional issues that may arise. As a result, these well-understood principles of growth design can be employed immediately. Additionally, since a comparatively large window of growth conditions can be employed during c-plane growth, many unconventional approaches can be employed using this growth plane. Relaxed InGaN buffers and substrates [17], InGaN metamorphic buffers [18], or other general high-In growth techniques can be employed more effectively in the c-plane orientation as relaxation is suppressed due to the inactive basal plane slip system [50]. Despite its drawbacks, the ability to examine a wider variety of growth schemes, wide substrate availability, and well understood material physics cause c-plane GaN to remain an attractive material system for development.

1.4 Defects and Morphology

Conventional growth of GaN on sapphire substrates includes a large thermal and lattice mismatch (14.3%) [51] inducing threading dislocations (TDs) with a high density as well as misfit dislocations (MDs) with lower density as a result of compressive strain. These TDs affect the growth microstructure of the material [52] and are generated in densities on the order of 10^8 cm^{-2} during growth, significantly reducing the crystal quality due to the high defect density. Fortunately, these dislocations are electrically inactive for both the edge and mixed-character TDs found in GaN, [53] allowing for high dislocation densities to be present in the material while maintaining the capability for high-performance electronic devices. Additionally, since these dislocations are less mobile by two orders of magnitude compared to other III-V semiconductor materials, their effect on long-term crystal degradation from dislocation movement is negligible [54]. Rather than forming electrical pathways, the threading dislocations instead act as nonradiative recombination centers [55] and sites of high-In fluctuation for mixed character TDs [56]. Higher growth temperatures will naturally reduce the amount of defects generated in the material during growth in general, but will result in significantly lower In incorporation due to the lower evaporation temperature of InN compared to GaN [27]. Similarly, employing hydrogen carrier gases during growth also would reduce defects; however, it also significantly etches away the In from InGaN alloys [57]. As a result, InGaN growth is difficult both due to the difficulty of growing a ternary alloy as well as the restrictions on growth conditions posed by In during growth.

Threading dislocations can also generate V-pits, which predominately arise with a TD at its core and propagate epitaxially, becoming wider depending on growth conditions [58, 24]. V-pits have 6 inclined {10-11} semipolar facets and lead to severe morphological deformation, causing a large surface roughness and resulting in poor interface quality [59, 60]. Moreover, when V-pits are formed in the buffer material early in the growth they are likely to propagate through the active region junction and form a p-n leakage pathway for devices [61]. The V-pits have also have higher charge injection on the sidewalls compared to the c-plane, making them an attractive leakage pathway [62] that could potentially bypass the active region [63]. While the V-pit is nucleated at a threading dislocation site, the pit propagation is controlled by reduced Ga incorporation efficiency and therefore a lower growth rate on the {10-11} planes compared to the c-plane [52, 64]. Since then the propagation of the V-pit is controlled by Group III metal incorporation, it is kinetically governed, and conditions that affect the surface mobility of the Ga or In adatom will directly affect the propagation of the V-pit as epitaxy continues. Kinetic barriers to filling the pit, in sum, are the cause of its propagation. Likewise if these kinetic barriers can be overcome through growth conditions, the V-pits will be filled and the surface will planarize.

One major challenge to growth of high-brightness long-wavelength visible LEDs is the formation and propagation of V-pits during growth in an uncontrolled manner. These

V-pits are undesirable since they create poor crystal morphology and nucleate at unpredictable times, causing the negative electrical effects previously mentioned on the resulting devices. It is important to point out, that intentionally forming V-pits engineered specifically to bypass barriers within the active region itself can be beneficial for device performance [21]. These "intentionally engineered V-defects" are generated in a short-period superlattice (SP-SL) grown immediately prior to the MQW region and are later filled with p-GaN. This overgrown p-type GaN region enhances lateral hole injection into the QW, creating a "3-dimensional" junction interface. This form of intentionally engineered V-defect has been used to realize record performance in devices with emission ranging from green to red [36, 65]. By contrast, when V-pits are present in the substrate or n-type base layers, well before the active region, they may propagate through the QWs and p-type region forming leakage paths.

In our case, for work on both red and green long-wavelength LEDs, V-pits were seen as a defect in devices, as any potential benefits they may offer had not been optimized or examined here. For green-emitting devices on conventional patterned sapphire substrates, the V-defects were typically generated unintentionally before the active region as a morphological and electrical defect as a result of the growth conditions employed. For red-emitting μLEDs on relaxed InGaN substrates, the V-pits are present even in the initial substrate, propagating throughout the entire structure rather than being confined to the active region. Since the pits are present initially, there is no opportunity to use more conventional methods to prevent their nucleation, only to eliminate them after they form.

Chapter 2

Methods for Growth, Characterization, Processing, and Packaging

2.1 Growth and Substrates

Samples were grown by atmospheric pressure MOCVD using a Nippon-Sanso two-flow reactor. Details of the reactor design have been thoroughly examined previously [66]. Growth employed triethylgallium (TEGa), trimethylaluminum (TMAl) trimethylindium (TMIn), and ammonia (NH_3) as the precursors for GaN, AlGaN, and InGaN growth. For n- and p-type dopants, disilane (Si_2H_6) and Bis(cyclopentadienyl) magnesium (Cp_2Mg) are used as precursors, respectively. Nitrogen and hydrogen are both employed as carrier gasses.

Substrates used throughout the studies on green LEDs were typical patterned sapphire substrates (PSS) available commercially from Crystal Optech. These consist of polished Al_2O_3 patterned with cones. Growth is performed on the patterned side of these substrates. Single-side polished (SSP) sapphire was also used, consisting of the polished wafer without the patterned cones. Generally, PSS was used for device growth, as these substrates have been shown to provide superior crystal quality and lower threading dislocation density [67] leading to better device performance. Occasionally, SSP substrates were used for devices, but mainly these substrates are employed for calibrations or test structure growths, as the patterning can cause optical interference during some measurements.

Substrates used throughout the studies on red μLEDs are provided by SOITEC, a private company, and are referred to hereafter as "InGaNOS" substrates. The substrates are polished sapphire patterned with 490x490 μm^2 InGaN mesas spaced by 10 μm cuts between them forming a grid. The lattice constant and amount of substrate relaxation can be altered based on the defined substrate mesa size and In content. This technology enables partially relaxed InGaN patterns from 490x490 μm^2 down to few μm^2 and large lattice parameters up to 3.219 . The substrate mesas are 150 nm thick and have a nominal lattice constant of 3.205 for all samples examined here, with a buried oxide (BOX) underneath between the sapphire and mesas. These substrate templates employ a nominal In content of 4% with 54% relaxation, and the relaxation can be tuned using SOITEC's proprietary Smart-Cut technology. Structurally, the epi-ready InGaNOS substrates contain a native V-defect density of around 5x10^8 cm^{-2}, and an x-ray rocking curve FWHM of 2600 arcsec for the (0002) reflection. More specific details on substrate processing and fabrication, as well as fundamental structural and optical quality characterization can be found in in prior work[15].

2.2 Chip and Device Design

Three types of chip design were used extensively throughout these projects, with the particular details of each design layout being specific to the research needs of each project. However, some commonalities existed between all iterations of the μLED chip layout. Device mesa sizes present on each design layout were 5x5, 10x10, 20x20, 40x40, 60x60, 80x80, and 100x100 μm^2 square mesas with rounded corners, as well as 0.1 mm^2 "standard LED" size devices arranged in rows by size and labelled. Contact alignment lithography and associated masks were used for some project aspects, specifically where later dicing and packaging was not needed and off-mesa contacts were not used. Generally, however, a stepper mask was employed for non-contact lithography for the vast majority of device applicaitons.

Contact alignment masks consisted of devices arranged in rows separated by 500μm, typically too close for later dicing and singulation. On-mesa contacts and pads were used for all device sizes, a full metal coverage p-contact on top of the device, allowing for simple, fast, and high-yield device fabrication. This design only contained 3 lithography layers- mesa, n-contact, and p-contact- in order to create the completed device using full metal coverage. If using a TCO as a p-contact, the device design can be achieved in only 2 lithography layers, as the n-contact can be co-deposited with the p-pad. Additionally, this lithography mask contained areas for device test structures such as linear and circular transmission line measurements (TLM and CTLM) for further chip-level characterization. This simple design was used to produce test devices and structures quickly and with high yield.

Stepper alignment masks can be seen in fig. **??** and fig. 2.2, with both designs used for different project purposes. The first of these design layouts consisted of devices arranged by size in rows separated by 1.5 μm, with a "plus sign" marking equidistant between each device in a grid. These "plus sign" markings represent the alignment marks for later dicing and device singulation. In this case, the devices are assumed to use a TCO as the p-contact layer, so only thin metal contact wires exist on the mesa top. Instead of full metal coverage, the contact pads are located off the mesa on opposing sides of the device, with a wire running vertically up the sidewall from the pad to the mesa top. These lithography masks also contained areas for device test structures, notably CTLM in this case. This design contained 3 or 4 lithography layers- mesa, dielectric, contacts, and an optional CTLM etch for one mask design. Since the contacts pads are off-mesa by design with a sidewall wire, dielectric isolation must be used for the p-pad to prevent short circuiting. A short circuit condition can be caused by both the wire touching the exposed sidewall and failing to inject current into the p-type region or by current simply traveling between the pads using only the n-type layer, ignoring the device completely. Additionally, this dielectric layer allows for a decrease to light absorbtion by the contact on the sidewall. Contact metals are co-deposited from use of the p-side TCO. If desired, a final lithography layer could be performed to etch the remaining TCO from the inner ring portion of the p-CTLM test structure, allowing the sheet resistance and specific contact resistivity to be probed. The second of these design layouts has functionally identical devices, but arranged so the devices are separated by 1μ and aligned a substrate grid. This layout also lacks dicing marks as the devices are packed much closer. These stepper designs were used to produce a large amount of test and development

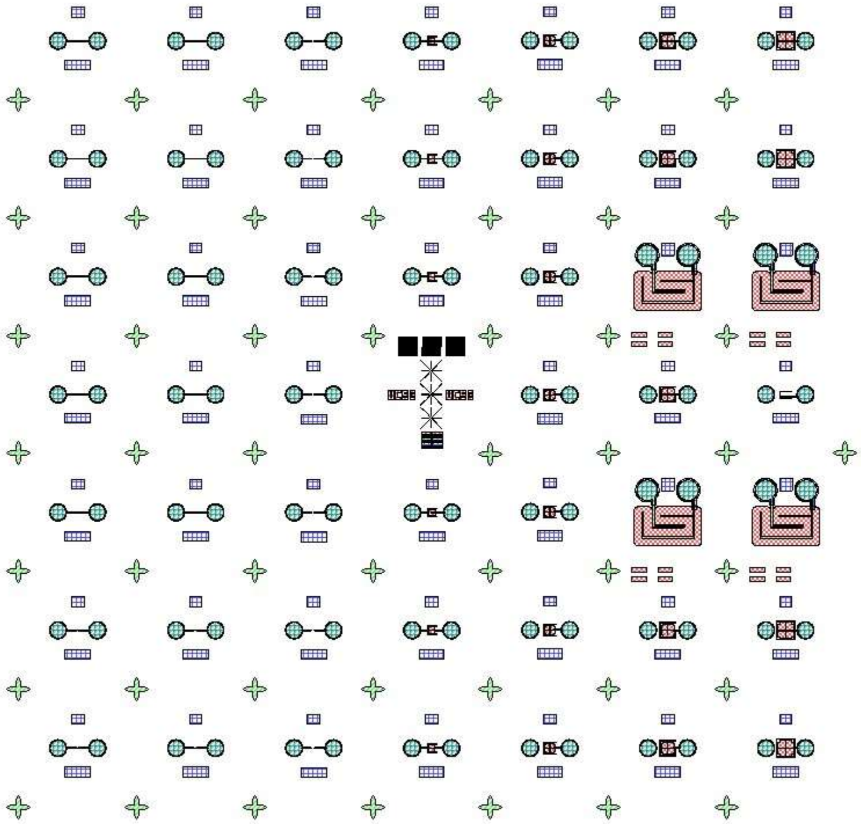

Figure 2.1: First lithography mask used for device development.

devices with the ability to later singulate and package, while also allowing for a large amount of robust on-chip measurement and characterization.

2.3 Process Flow and Packaging

Prior to further testing, all LED and μLED growths, or any other growth containing a p-type layer employing a Mg dopant, must be activated *ex-situ* in a separate thermal processing oven. In order to create conductive p-type regions, hydrogen must be driven out

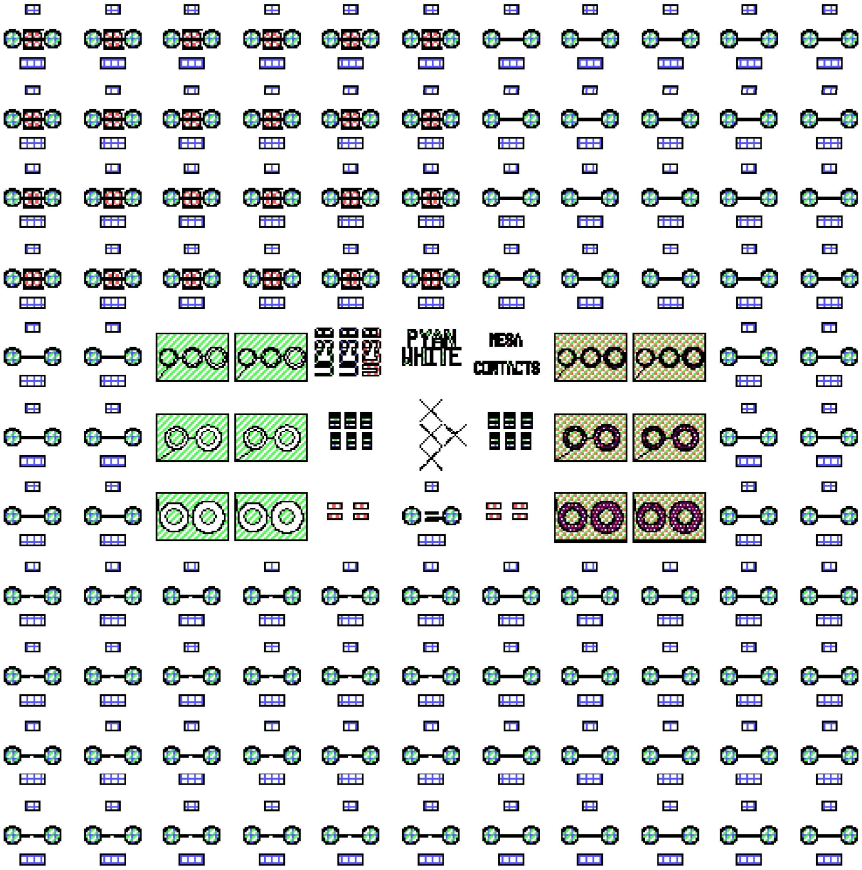

Figure 2.2: Second lithography mask used for device development.

of the p-type region. This is accomplished by enclosing the as-grown samples in a thermal processing oven at 600°C uninterrupted for 15 minutes followed by cooling at ambient temperature. For fabrication of devices from as-grown epi, mostly identical μLED fabrication processes are employed for all samples, with only a few notable differences based on chip design or particular device considerations. First, all samples were submerged in heated aqua regia at 120°C for 10 minutes, repeated three times. Following this acid treatment, rinsing and a standard solvent clean was performed to remove any surface impurity contamination, remaining surface Mg, or other growth residues.

For all devices employing contact lithography, first the device mesas are defined using reactive-ion etching (RIE) employing $SiCl_4$ to etch the III-Nitride epi down to the n-GaN layer while leaving behind some Si as a contact layer. Next, lithography is performed to define the n-contact area, and a 300/1000/300/2000 Ti/Al/Ni/Au metal stack is deposited as a contact using electrion beam deposition. After deposition, samples are soaked in heated NMP and excess contact metal is lifted off. Finally, the last lithography is performed to define the p-contact area, and a 300/2000 Cr/Au metal stack is deposited using electron beam lithography. The lift-off procedure in NMP is then repeated. Final devices can then be tested. A full process traveller can be found in Appendix A.

For all devices employing stepper lithography, after sample cleaning and acid treatment, 110 nm of indium tin oxide (ITO) was deposited as a transparent conducting oxide (TCO) layer using electron beam deposition for use as a p-contact. Device mesas are first defined with lithography, then using RIE, first with a methane/hydrogen/argon plasma to etch the ITO layer, then using $SiCl_4$ as a self-aligned etch of the III-Nitride epi down to the n-GaN layer. After etching, the second lithography is performed to define the area for an omnidirectional reflector (ODR), consisting of three periods of silicon dioxide (SiO_2) and tantalum oxide (Ta_2O_5) layers followed by an aluminum oxide Al_2O_3 capping layer was deposited using ion beam deposition (IBD). The samples are then submerged in heated NMP and excess dielectric is lifted off The thicknesses of each of these ODR layers are determined by the particular wavelength of light emitted by the sample. The periodic SiO_2 and Ta_2O_5 layers act as a sidewall reflector while the Al_2O_3 layer acts as a contact sticking layer, allowing dielectric isolation and good contact adhesion. Next, atomic layer deposition (ALD) was used as a sidewall passivation, depositing 50 nm of SiO_2 at 300°C in a blanket deposition. After ALD, the third lithography is performed to define the contact pad areas. These defined areas of SiO_2 were removed using buffered hydrofluoric acid (BHF) to allow contact deposition onto the GaN. Common contact pads for the p- and n-side were composed of 5000/1000/5000 of Al/Ni/Au and deposited using electron-beam deposition. Samples are again submerged in NMP to lift off any excess metal. As an optional last step if necessary, a fourth and final lithography can be performed, defining the inner-circle areas of the CTLM test structures for later etching. The RIE methane-hydrogen-argon etch can then be repeated to remove the TCO from the CTLM rings. Final deices can then be tested. A full process traveller can be found in Appendix A.

Packaging of the processed on-chip devices was performed manually. Devices were singulated using a dicing saw and cleaned with standard solvents. Selected devices were then mounted to the surface of conductive silver headers with Dow Corning OE 6550 optical epoxy and baked to cure the mounting epoxy. Next, Au wire bonds were attached with a wire bonder using a ball bond at the device contact pad and attached to the header leads. Optical epoxy was then added as a lens and encapsulating material and baked to cure, completing the device. From basic light extraction modelling, the light extraction efficiency (LEE) of the package is estimated to be approximately 30%. Absorption in the InGaNOS substrate will also further reduce the LEE of the complete packaged device. Electrical testing of the finished devices was performed using a Keithley source generator and light collection was performed using a Instrument Systems integrating sphere.

Chapter 3

Developing the Green Gap for Efficient Lighting Sources

3.1 Project Aims and Goals

Green LEDs in the "Green Gap" region of emission suffer heavily from droop effects caused from worsened strain and high-In effects, making them far less efficient than their blue counterparts and as a result have received comparatively little development progression. Despite their lack of development, green-emitting LEDs have a use in crucial RGB display and color-mixed white lighting applications. In order for green III-N LEDs to be effectively used in lighting and RGB display applications, the efficiency must be improved to achieve adequate brightness at operating current densities. For this project, attempts are made increase the internal quantum efficiency (IQE) of a standard-size LED (0.1 mm^2) above 54%, as well as the EQE of the device above 46%, requiring development both to the internal electronic structure of the devices and with light extraction and packaging. Taking into account the operating voltage of the device as well as the quantum efficiency of creating photons from recombining charge carriers, attempts to increase the power conversion efficiency (PCE) to 35% are made. These efficiency metrics are then defined as being at an operational current density of 35 A/cm^2, typical for device applications.

In this section, three major areas of LED development to improve device efficiency to the level set out in our metrics are explored. Our research in this area predominately focused on reduction of excess forward voltage under device operation, reduction and management of polarization barriers affecting charge transport and efficient radiative recombination, and the reduction and engineering of defects, especially large-scale V-defects. Each of these development areas improves the resulting device in a slightly different- but realted- way. Reduction of forward voltage improves the wall plug efficiency (WPE) and power conversion efficiency, as less electrical power would be used to achieve the same intensity brightness even when the quantum efficiency (whether measured by IQE or EQE) is equivalent between samples. Reduction and management of polarization barriers then compliments these developments by increasing the rate of radiative recombination from charge transport benefits, resulting in improvements to the IQE of the device itself. Finally, reduction of defects, especially V-defects, then improves the morphology of the device by reducing the number of nonradiative recombination centers, further improving the efficiency by generating greater light output power at equal current density injections.

3.2 Improving Operating Voltage

One of the first main areas of focus in developing these green emission LEDs is reduction of forward voltage under operation. Despite the decreasing band gap energy with increasing In content for green emission, the required forward voltage for operation increases with wavelength causing a significant drop in WPE. Voltage reduction was achieved through systematic examination of the previously developed “state of the art” [45] LED architecture (fig. 3.1) for barriers to electrical transport as a source of excess voltage. Through examining this structure, AlGaN-containing layers, a thin pre-well superlattice (SL), and thick quantum barriers (QBs) are identified as sources of excess voltage. This added voltage was specifically notable when comparing LEDs with varying QW numbers (fig. 3.2), adding a “per well” voltage penalty due to transport barriers in the active region. Wholesale removal of the AlGaN electron blocking layer (EBL) appeared to have no negative impact on EQE, but lowered the operating voltage by reducing the overall resistance of the device from the reduced amount of high-resistivity AlGaN present. While leakage current from electron overshoot into p-GaN may be present in lower-In blue LEDs with much shallower QWs from the reduced In content, for green LEDs there appears to be little impact or evidence of electron overshoot. As a result, removal of the EBL on results in beneficial electrical effects. Additionally, increasing the number of periods of the InGaN/GaN SL showed to drastically reduce the operating voltage as well, eventually settling on 45 periods (fig. 3.3). The pre-well superlattice is thought to act as a “defect filter” for the buffer layers, causing dislocation annihilation at the InGaN/GaN interfaces to reduce the dislocation density and bury incorporated impurities that form nonradiative recombination centers [68]. Next, the p-contacts were changed from more resistive ITO to a Pd/Au metal stack and their ohmic character was confirmed with circular transmission line measurements (CTLMs) for ohmic behavior (fig. 3.4) as non-ohmic (Schottky) contacts will result in added voltage at the contact proportional to injected current density. Removing the EBL, optimizing the p-contact, and enlarging the superlattice all improve charge transport to the QW, reducing the operating voltage of the device.

Within the active region itself, both the AlGaN cap and the low temperature (LT) / high temperature (HT) GaN QB are also optimized to reduce the "per well" voltage penalty present in the green LED structures. Firstly, the Al content in the AlGaN caps immediately after the QWs is reduced, following the same logic as when removing the EBL. Since a higher Al content leads to higher resistance in the device, it also subsequently increases the required forward voltage. While the benefits of using some Al in the AlGaN cap are unquestionable [69] for strain and In retention considerations, the 30% Al content used also adds significant voltage. By reducing the Al content to 10%, significant reduction in forward voltage can be achieved (fig. 3.5) without sacrificing the capping improvements of AlGaN layers. Additionally, thinning the GaN barrier from 10 nm to 6 nm also improves forward voltage, as less GaN is present to add less resistance to charge transport between wells. Combined, these improvements reduce the "per well" voltage penalty significantly (fig. **??**), in addition to the baseline voltage improvements in the LED structure through the contacts, SL, and EBL. These improvements were combined to create a new optimized structure, which possessed much lower forward voltage due to removal of transport barriers

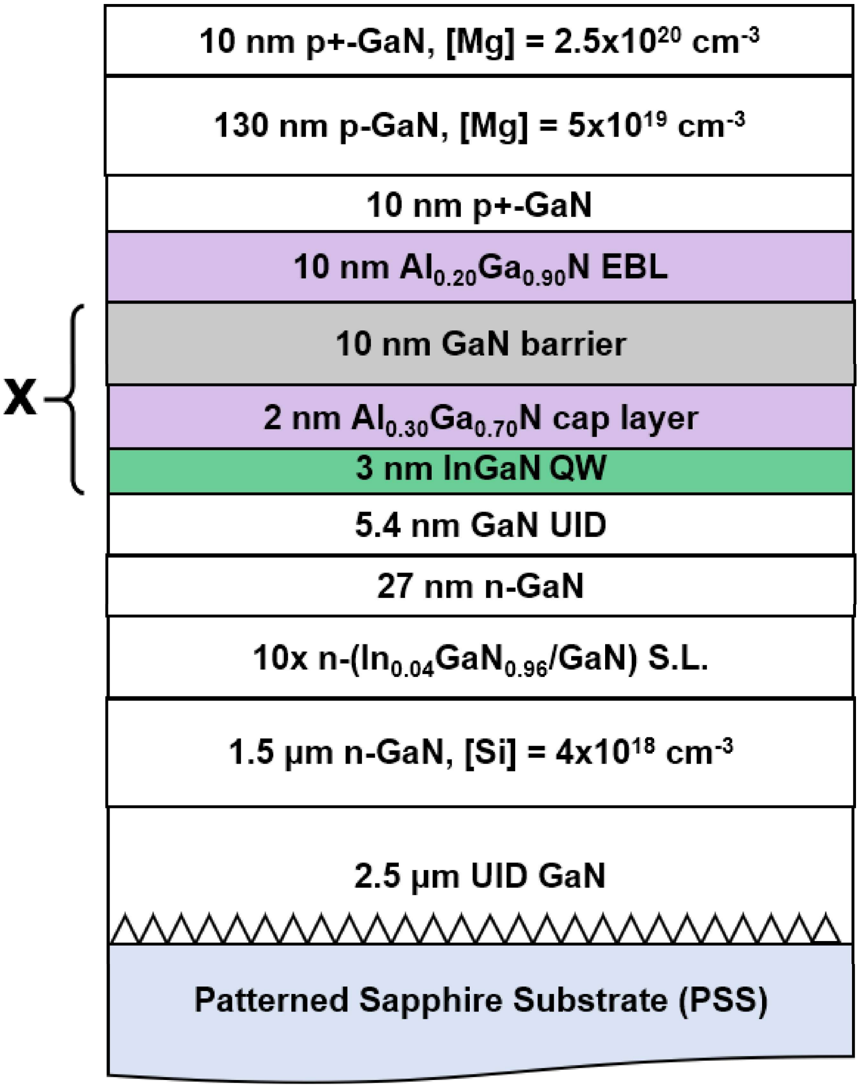

Figure 3.1: Initial "state of the art" green LED before any voltage optimizations.

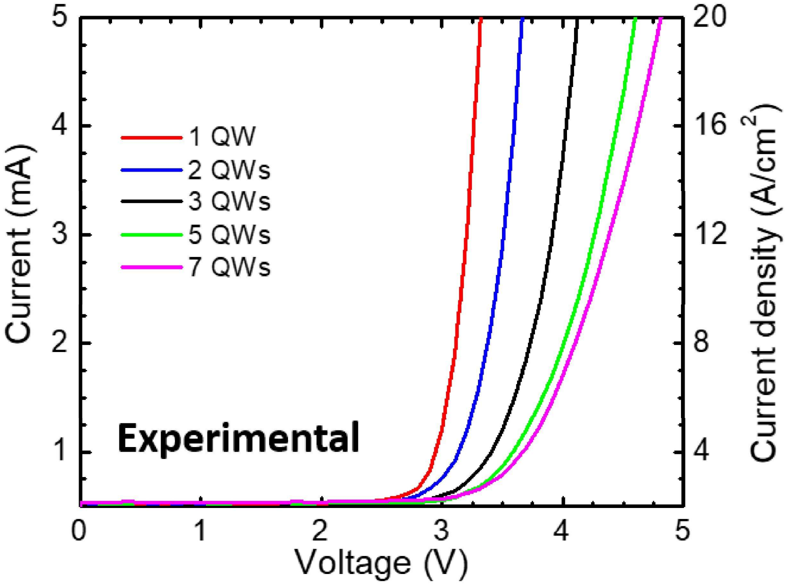

Figure 3.2: Current-Voltage curves for unoptimized LEDs with varying QW numbers. Significant added voltage per well can be seen.

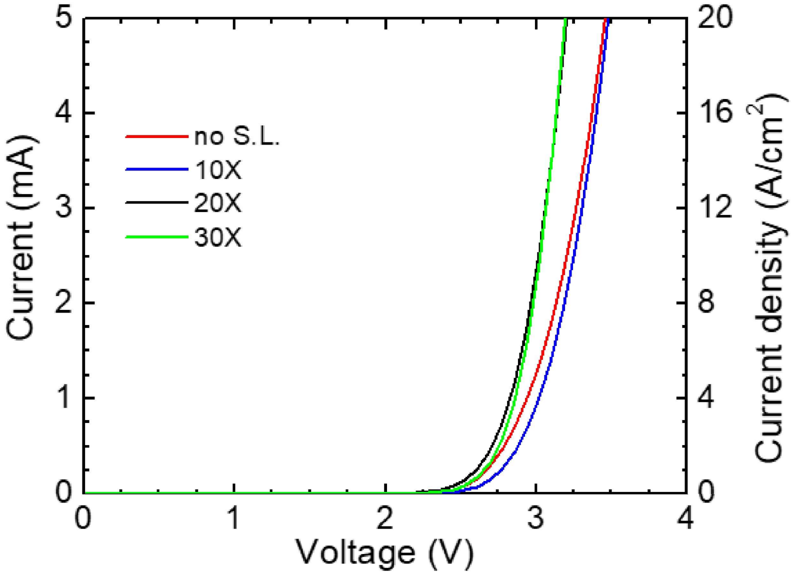

Figure 3.3: Current-Voltage curves for LEDs with varying SL periods. Operating voltage reduced with increasing SL period.

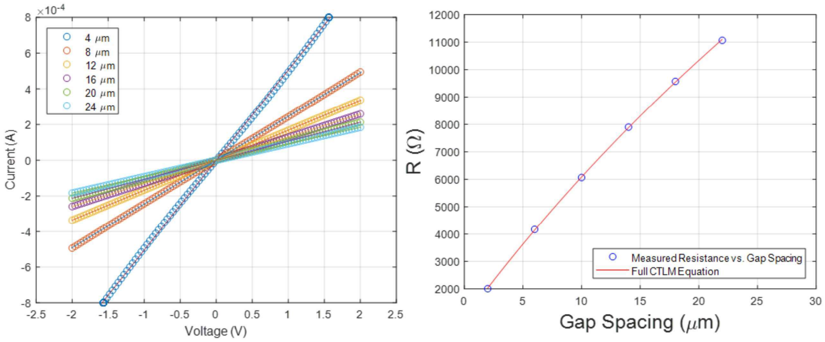

Figure 3.4: CTLM of ohmic p-contact. (left) IV curve of many gap sizes. Linear IV implies ohmic contact (right) Extracted resistance vs gap spacing used to determine specific contact resistivity.

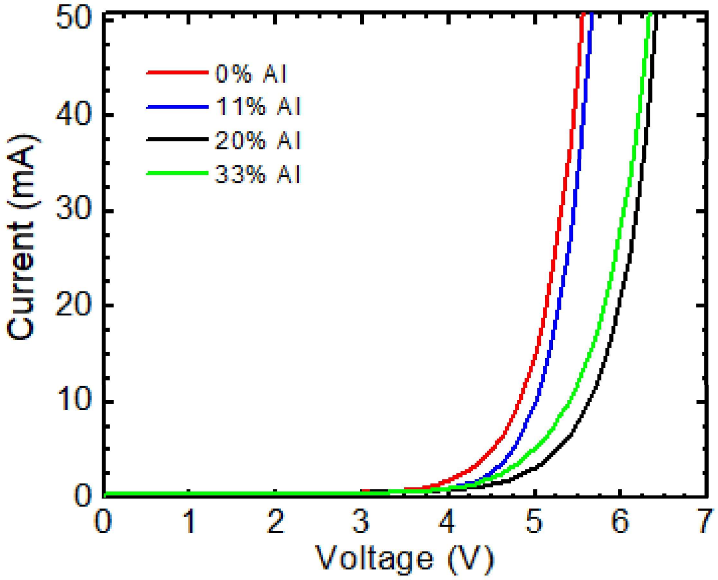

Figure 3.5: Current-Voltage curves for LEDs with varying Al content in AlGaN capping layers. Higher forward voltage trends with increasing Al content.

and importantly, a lower “per well” voltage penalty (fig. **??**).

Fluctuations of In, especially at the InGaN/GaN interface, are detrimental to device performance when the fluctuations are large; however, when fluctuations are small they can provide transport benefits. Charge carriers are transported through the regions containing lower polarization barriers, ultimately collecting in regions of high In content. This creates pockets of high carrier density in the smaller-bandgap regions (fig. 3.8a) where they localize at lower potential regions before radiatively recombining (fig. 3.8b) [26]. For these high-In regions, the spatial separation of the charge carrier wavefunctions is lessened due to small length scales of high-In fluctuations and there is higher local carrier screening due to high carrier density [70]. As a result, the In fluctuations also have an effect on the IQE

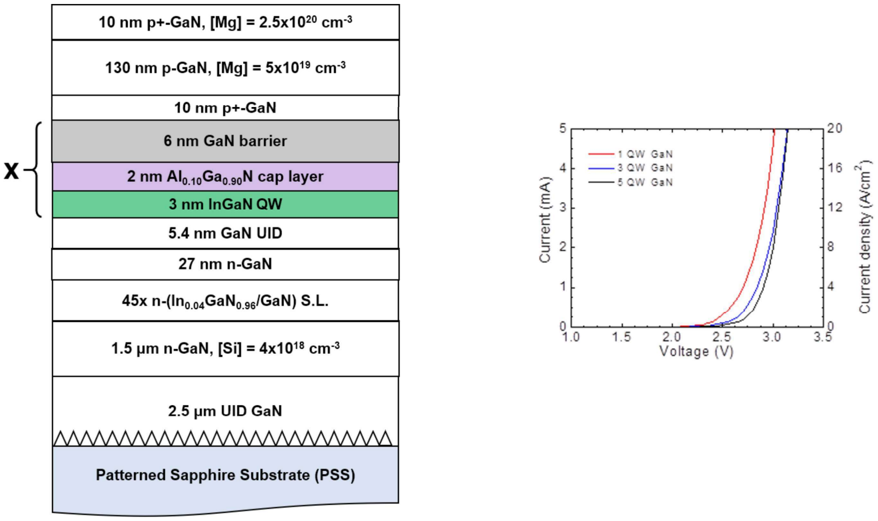

Figure 3.6: Current-Voltage curves for optimized LED active regions with varying QW numbers. Significantly reduced voltage penalty per well.

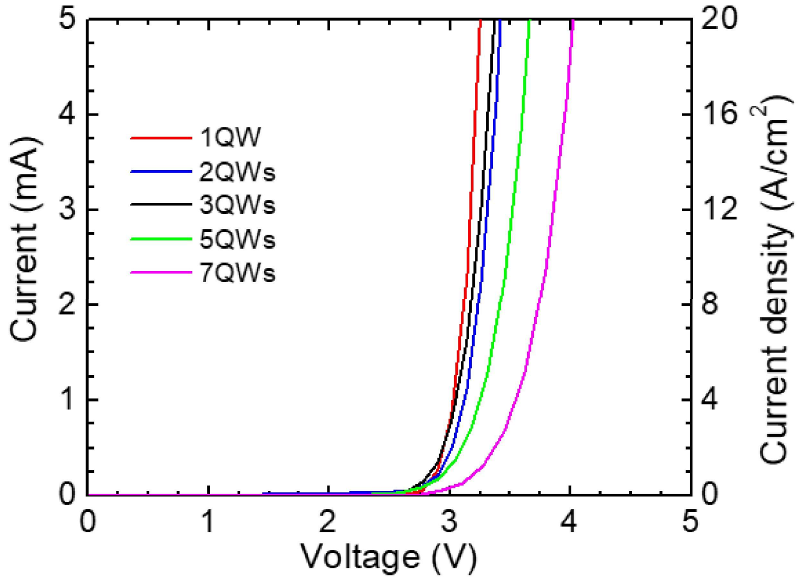

Figure 3.7: Optimized low-voltage LED structure (right) Current-Voltage behavior of varying QW number LEDs with this structure. Much lower voltage penalty seen compared to initial performance. Significantly reduced "per well" voltage penalty.

of the device. Ultimately, the necessary voltage for a given current density is lowered from these transport benefits [71, 72, 45]. Since carriers travel through a low barrier (low-In) region and localize in a low potential (high-In) region, the In fluctuations form a percolation path requiring a lower forward voltage for a given amount of current [70]. In general, the smaller fluctuations of In provide transport improvements in devices ultimately leading to similar performance but at lower voltages, ultimately improving the WPE. This theory was used to describe phenomena in the QWs, but also informed experiments introducing In to the GaN QBs, intending to employ this percolative transport effect to further reduce voltage. While this experiment was successful in reducing operating voltage at a given current density it also induced a 10-30 nm emission shift due to the lessened strain polarization (and subsequent red shift from the QCSE) (fig. 3.9) at 4% In, meaning lower growth temperatures would be required for the same emission wavelength, reducing efficiency and ultimately offsetting any improvements. In light of this result and differing material physics that would need to be accounted for, InGaN barriers were not pursued further.

3.3 Increasing Power at Lower Voltages

Immediately after improving the efficiency of green LEDs through reducing the excess forward operating voltage, attention is turned to reclaiming absolute optical power lost during efficiency improvements and systematic approaches to improving the quality of each layer with alternative growth schemes. The active region is focused as the biggest source of potential improvement, as barriers and capping layers had previously been shown

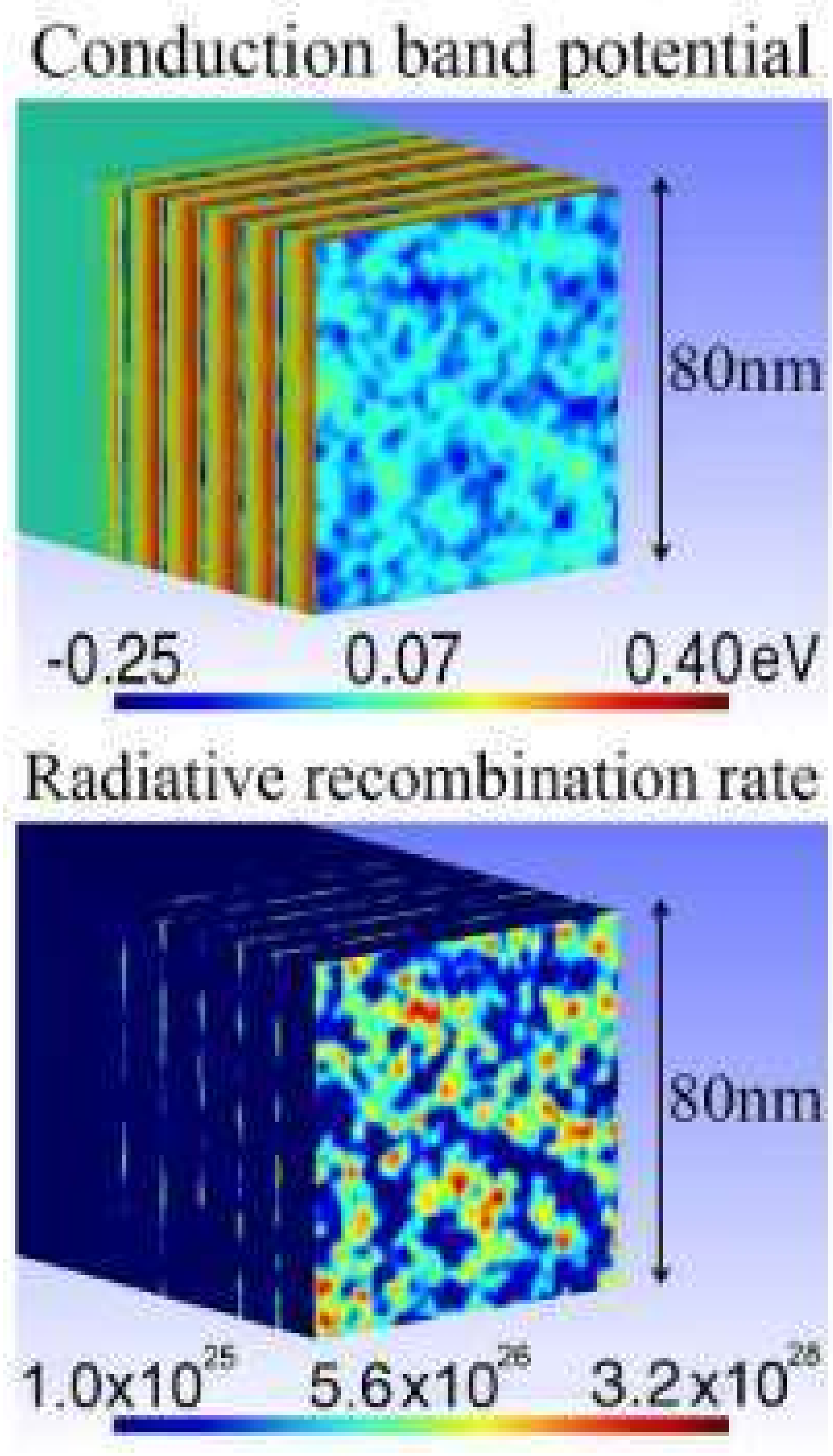

Figure 3.8: Simulated (top) conduction band potential and (bottom) radiative recombination rate in a high-InGaN well. Spatial fluctuations can be seen for both cases, indicating 3D percolative transport is present.

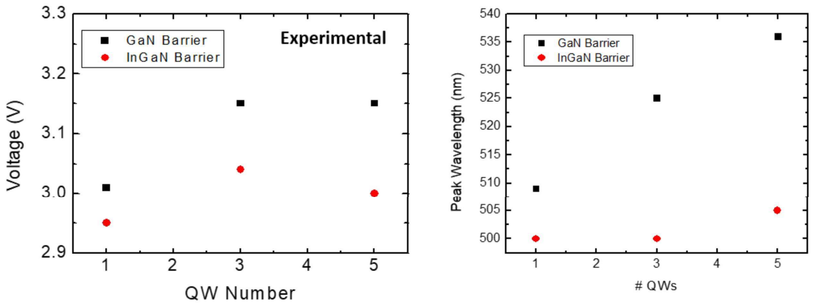

Figure 3.9: Experimentally measured voltage and (right) wavelength at 20 A/cm^2 current density for LEDs with different QW numbers. The "per well" voltage penalty is reduced but at the expense of shorter wavelength.

to drastically affect both power and efficiency. Initially, the AlGaN cap, LT and HT GaN barriers were examined in terms of their growth rate while maintaining equal composition, thickness and temperature. The guiding principle was that a faster moving growth interface would ultimately expose the QWs to higher temperatures for less time and can suppress In desorption and desorption-redeposition leading to disorder. First examining a faster AlGaN cap growth rate, a small amount of power and efficiency (fig. 3.10) is lost by increasing the growth rate at equal composition, but a notable red shift in wavelength is also present. This could be explained by superior In retention in the well from the faster moving growth interface, explaining the emission redshift. Additionally, the faster growth rate could also lead to lower material quality immediately adjacent to the QW, also explaining the small power reduction. Next, examining the growth rate of the LT GaN barrier immediately following the AlGaN cap, it is increased in order to reduce the time the QW and cap are exposed to high temperatures. Increasing this growth rate of the LT barrier led to a monotonic increase in power and efficiency (fig. 3.11) with only a small wavelength blueshift. Finally, a

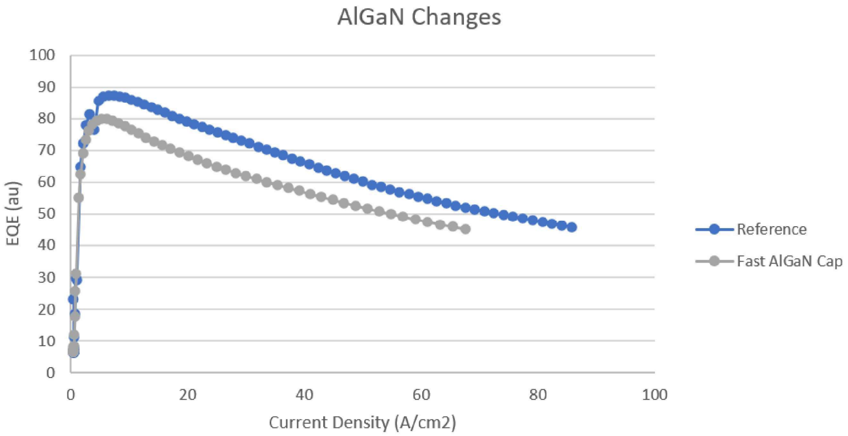

Figure 3.10: EQE vs. Current Density measurements for green LEDs with varying AlGaN cap growth rate

slower growing QW is examined in an attempt to improve material quality, but this resulted in much lower power and a wavelength blue shift (fig. 3.12). In all these cases, a faster moving growth interface is leveraged to better protect the sensitive high-In active region

In addition to growth rates, the effect of altering layer growth schemes with doping in QBs was examined, employing In surfactants or p-InGaN in the p-GaN region, and H_2 carrier gas in the QWs. Employing Si doping in the QBs has been widely suggested to improve material quality, [73] interface quality, [74] encourage radiative recombination in active wells, [75] and suppress detrimental spiral growth at dislocations in the QWs [76]. These doped barriers are intended to provide a greater localization effect [77] to both move the junction interface closer to the p side and by reducing the QCSE in the well immediately following doping, improving the radiative efficiency. While introducing increasing Si doping leads to worsened crystal morphology from Si antisurfactant behavior (fig. 3.13), significant improvement both in current-voltage behavior and in light output power was

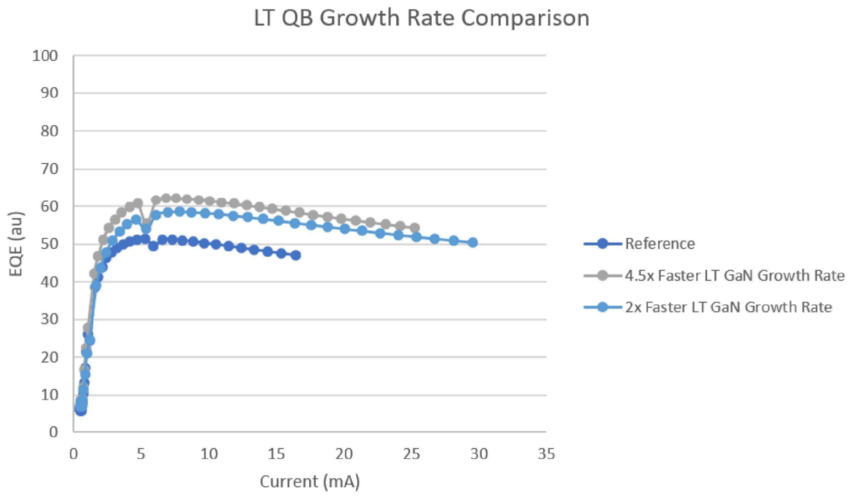

Figure 3.11: EQE vs. Current Density measurements for green LEDs with varying LT GaN growth rate.

Figure 3.12: EQE vs. Current Density measurements for green LEDs with varying QW growth rate.

also seen (fig. **??**). Both results point to improving barrier conductivity with Si doping and improved radiative emission as expected and were utilized in further design. Employing a very small amount H_2 gas during growth of the QWs was also tested, hoping to improve crystal morphology and decrease impurity inclusion. Even employing the lowest hydrogen flow available in the reactor (100 sccm), far too little In was incorporated for the QWs to be useful for green LEDs. Though some etching was expected, the level seen was far too severe for further use. Using both p-InGaN and/or an In surfactant in the p-region of the LED is also theorized to improve device efficiency, as p-InGaN would induce downward band-bending and subsequent hole accumulation as well as surface quality improvements from surfactant behavior. However, the In had apparent surfactant effect on surface morphology (fig. 3.15) or contact resistance. This trend continued for p-InGaN, which surprisingly saw no notable improvements over the reference sample across a range of In contents in both morphology (fig. 3.16) and electrical contact performance. As a result, neither of these methods were applied further.

Finally, what was dubbed the “ultralattice” in the active region was employed: four low-In blue wells with a final green “emitting well” at the top. These lower wells are low-In blue wells rather than all green wells in order to retain better material quality, which would worsen with higher In content. It has been theorized that the lower wells in the active region are relatively inactive during LED operation due to poor hole mobility and large hole effective mass. As such, it is anticipated that the only emitting well is that closest to the p-side of the device, while the rest remain relatively inactive in terms of radiative emission. Unexpectedly, the “ultralattice” device showed electroluminescence (EL) both green and

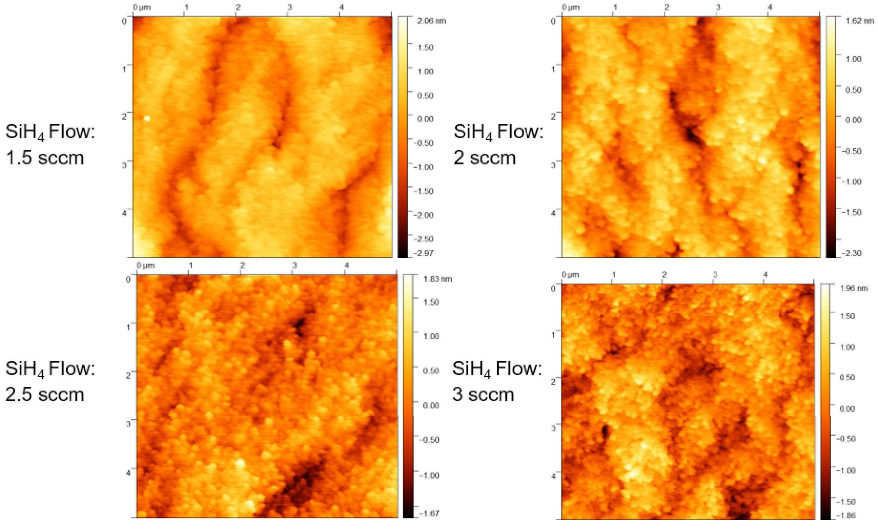

Figure 3.13: AFM images to show morphology of Si doped QBs.

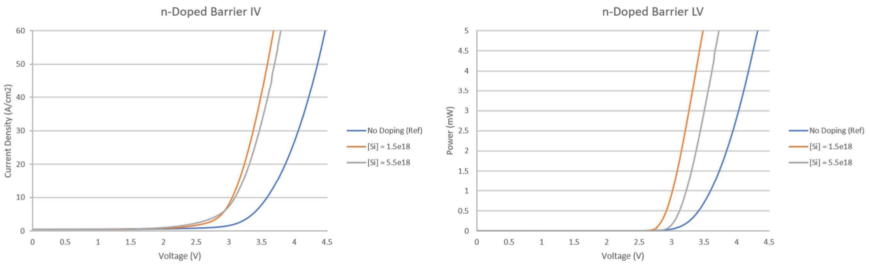

Figure 3.14: AFM images to show morphology of Si doped QBs.

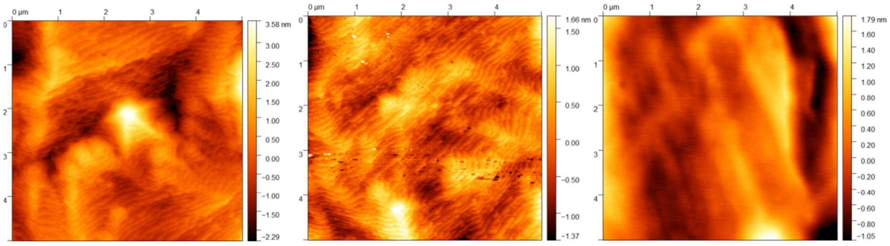

No TMI

95 sccm TMI

190 sccm TMI

Figure 3.15: AFM images to show morphology of In surfactant p-GaN.

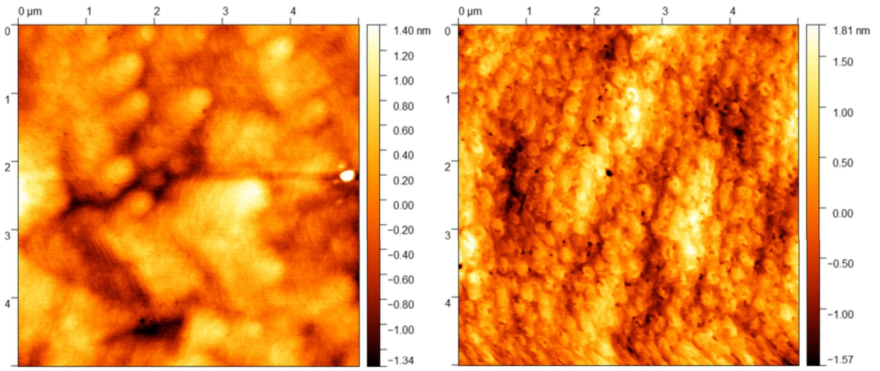

Reference p-GaN

900°C

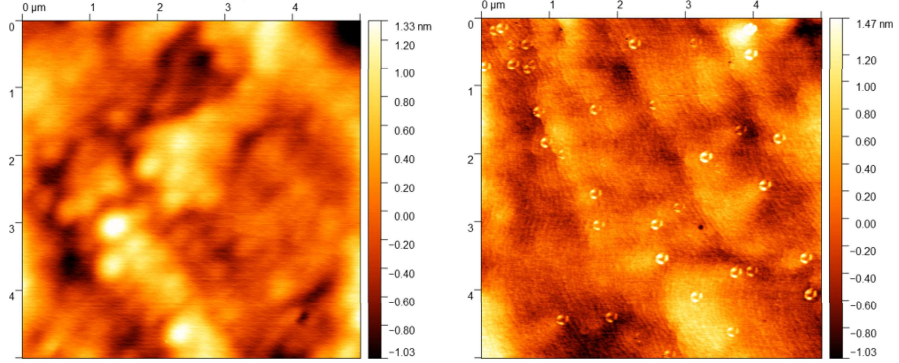

940°C

960°C

Figure 3.16: AFM images to show morphology p-InGaN at different temperatures/In contents

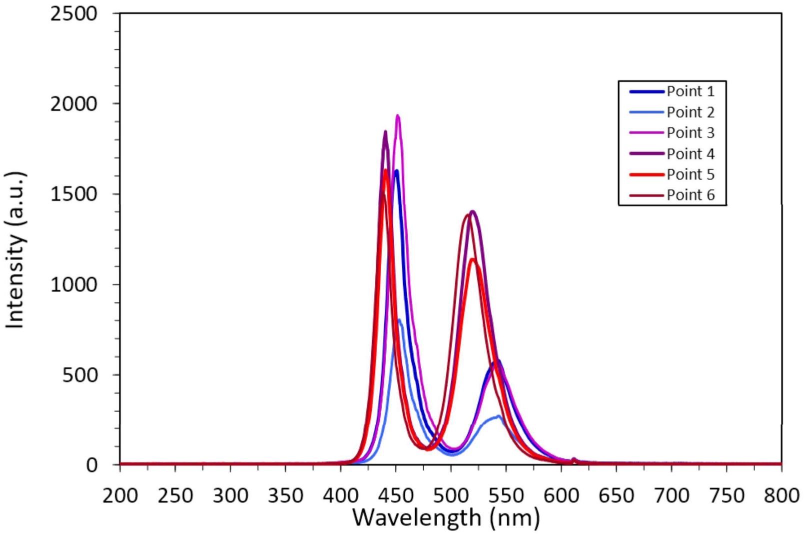

Figure 3.17: EL spectra of “ultralattice” LED at various wafer points. Approximately 2:1 intensity for blue:green emission in 3QW LED.

blue emission of nearly proportional intensity (fig. **??**), indicating both the lower wells and the "emitting well" were both sites of significant radiative recombination. It is postulated that V-pits generated under the active region propagate through it to the p-GaN, allowing holes to be injected into lower wells in relatively equal proportion to the top well even with n-doped QBs to move the junction. This result then prompted significant further exploration into V-pits and their effect on device performance.

3.4 V-pit Control and V-Injector Sea Change

I examined several SL growth conditions to ascertain their effect on V-pit size and density, including Si doping, temperature/In content, period number/thickness with a constant total SL thickness, and InGaN per period. While all these conditions were compared,

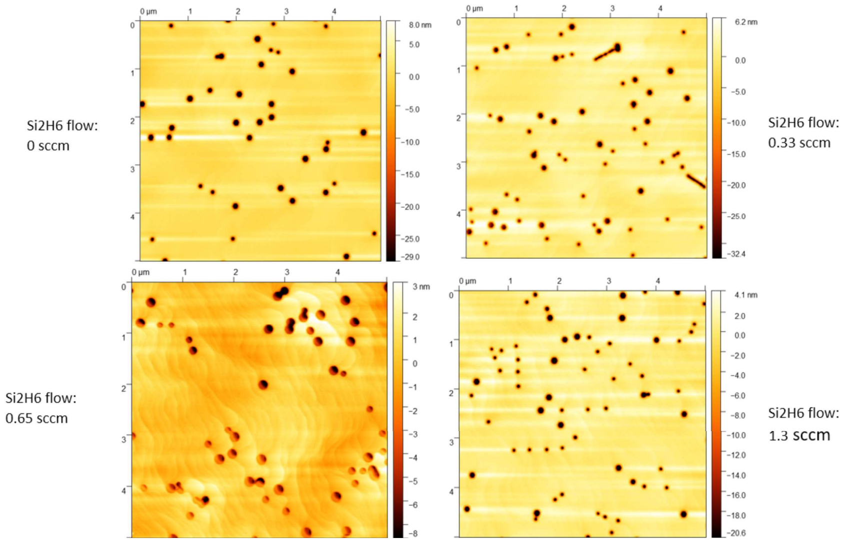

Figure 3.18: AFM taken on SL surface with varying Si doping. Inconclusive effect on density and size.

these experiments were inconclusive in terms of their effect on pit size or pit density (fig. 3.18, 3.19, 3.20, 3.21). In contrast, growth rate and V/III ratio showed some impact on pit size and density (fig. 3.22, 3.23) somewhat as expected. Since the (10-11) planes of the V-pit sidewalls are slower growing, the V-pit growth is kinetically controlled, and therefore the growth rate is expected to exert strong control over V-pit size. Additionally, V/III ratio should affect Ga adatom mobility during growth, with less NH_3 during growth (lower V/III ratio) allowing for greater lateral mobility of surface adatoms. While reducing the growth rate did successfully reduce the V-pits, the V/III ratio was again inconclusive in the relatively small window examined. Moving forward, these experiments will inform the reduction or production of V-defects as necessary. More important than the results themselves, the principles underlying them are further applied to other experiments and projects in order to achieve continued success.

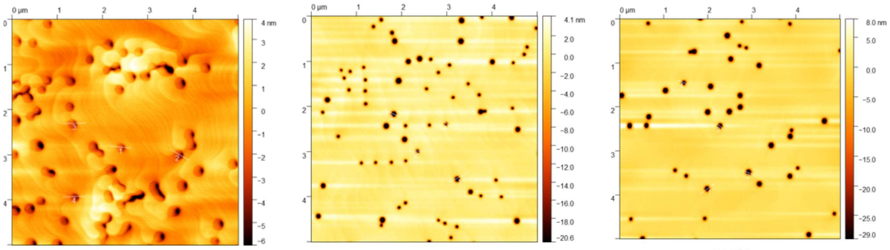

900°C

907.5°C

915°C

Figure 3.19: AFM taken on SL surface with varying growth temperature and resulting In content. Inconclusive effect on density and size.

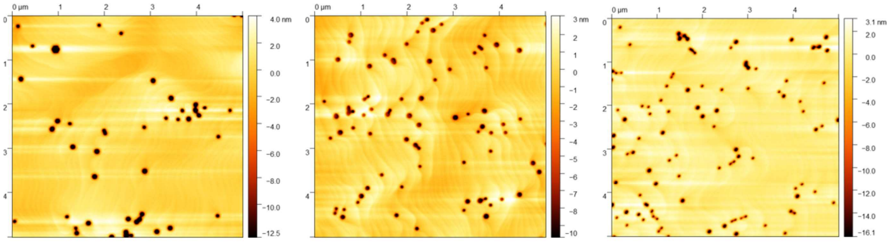

50x 1.5/1.5nm InGaN/GaN

30x 2.5/2.5nm InGaN/GaN

15x 5/5nm InGaN/GaN

Figure 3.20: AFM taken on SL surface with varying period thickness. Overall SL thickness held constant. Inconclusive effect on density and size.

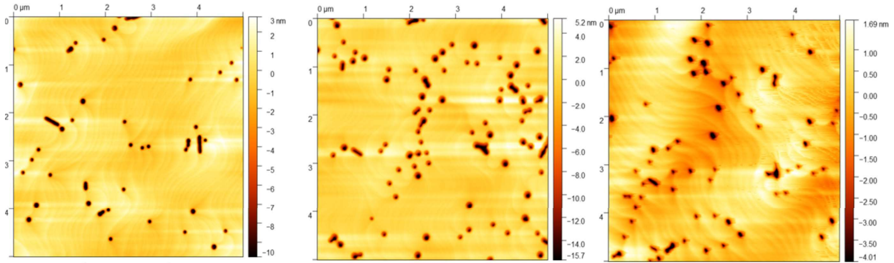

2.5/5 nm InGaN/GaN

3.75/3.75 nm InGaN/GaN

5/2.5 nm InGaN/GaN

Figure 3.21: AFM taken on SL surface with varying InGaN per period. Overall SL thickness held constant Inconclusive effect on density and size.

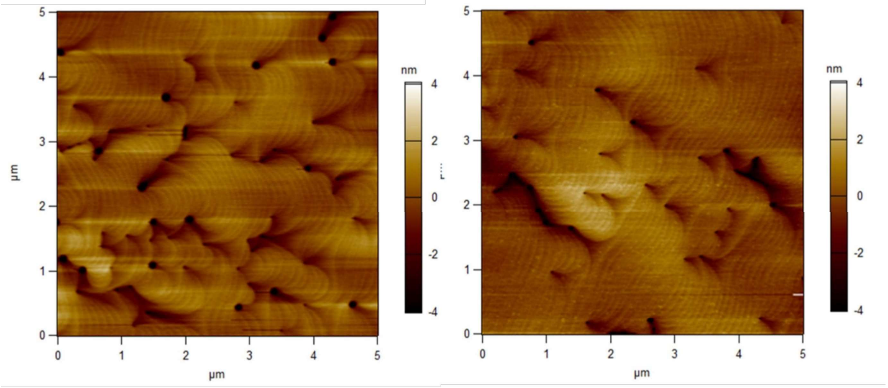

Reference

Reduced GR by factor of 2

Figure 3.22: AFM taken on SL surface with varying growth rate. Growth rate reduction reduces the density of pit formation.

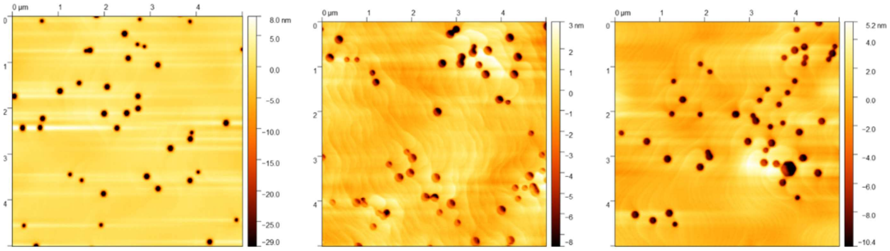

3 SLM NH3

4 SLM NH3

5 SLM NH3

Figure 3.23: AFM taken on SL surface with varying NH_3 flow and resulting V/III ratio. Inconclusive effect on density and size.

V-pits have been shown to significantly improve the performance of green and yellow devices [65] through superior charge injection, lower polarization barriers, [78] and 3D charge injection when properly engineered [79] only immediately below the active region. When material degradation and leakage issues such as that caused by V-pits originating in the n-GaN buffer can be avoided, V-pits can be employed immediately before the active region for much higher performance. When nucleated at the beginning of the active region, the void they create is later filled with p-GaN, allowing holes to flow through the conventional c-plane interface as well as through the side of the V-pit into an active region (or below if nucleated below) (fig. 3.24)[62]. V-pit sidewalls are made from the (10-11) planes, making their growth rate much slower and only subject to partial polarization. Pseudo-QWs form on these planes, much thinner and lower In content than the c-plane QWs, improving transport [63] through the V-pit sidewall into the active region [62] while also acting as a local potential barrier [80] to the threading dislocation. If generated homogenously and with an optimized size and density, these V-pits could provide significant device improvement.

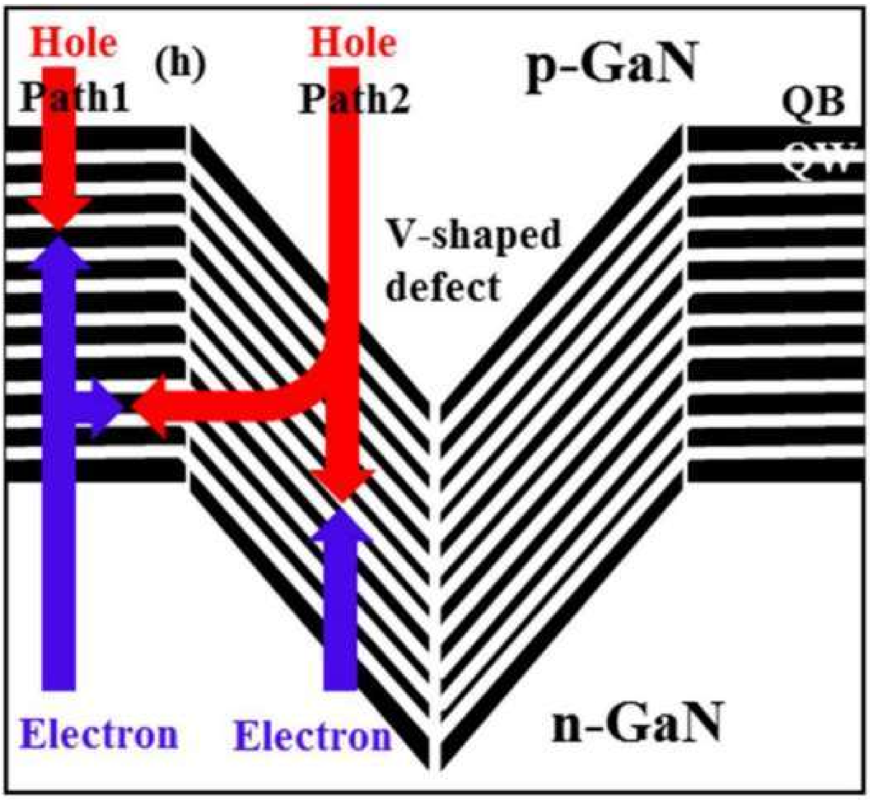

Figure 3.24: Schematic representation of injection through (1) the conventional c-plane and (2) the V-pit sidewall into the active region.

Chapter 4

Red Emission from III-Nitride Materials

4.1 Project Aims, Goals, and Prior Perspectives

Despite highly efficient blue devices, longer wavelength InGaN-based optical devices (i.e. green, yellow, red) suffer from much lower quantum efficiencies due to the difficulty in incorporating indium at compositions exceeding 25% without serious morphological issues [21, 81]. This same drawback is also present in the realization of blue- and green-emitting devices, where incorporating more In into the active region results in a litany of strain effects and morphological degradation considerations. High-In effects on material growth and device performance are exponentially worsened with increasing In content, making development of high-power, efficient, red-emitting InGaN-based devices a much more difficult task than for previous blue and green devices. However, despite their lack of technological maturity, long-wavelength emitting III-N devices may possess some device performance benefits with further development based on their fundamental material properties in addition to their application cost benefits.

To-date, the efficiency of InGaN-based red LEDs (>600 nm) is still very low (2.9% EQE), [82] preventing the realization of several applications using all nitride-based LEDs and μLEDs. Currently, many applications use phosphide materials, notably AlInGaP, for the red-emitting long-wavelength components. Red-emitting phosphide material systems have contrastingly seen significant development spanning multiple decades, resulting efficient devices operating at these wavelengths. However, phosphide systems are unable to emit at the shorter blue and green wavelengths necessary to create RGB displays with only a single material system. Conversely, InGaN-based systems have seen robust development in the shorter blue and green wavelength regimes, but are only in the very early development stage for red-emitting devices. As a result, both material systems are used in tandem for a single application, driving up production cost compared to a single material system covering the entire visible range. With enough development, III-N based materials can emit at wavelengths covering the entire visible range, and potentially outperform AlInGaP materials even in the long-wavelength regions.

For our work on InGaN-based devices emitting at long wavelengths, a few fundamental advantages of III-N materials for long-wavelength applications over AlInGaP are first established. While many issues have been solved for AlInGaP in its development, III-N possesses some fundamental material property advantages in terms of surface recombination [3] and thermal performance. For work on creating long-wavelength emitting devices, employing relaxed substrates are focused to avoid detrimental strain-related effects from the high In content required in the active region. Strain reduction carries two major benefits:

the reduction of the strain-generated polarization effects and increased In incorporation in the QW through reduction of the compositional pulling effect. To establish these benefits, an all-InGaN structure must be used for coherent lattice-matching to the substrates, which carries a number of material quality considerations. One first major thrust of device development is creating low-defect material suitable for high-performance devices, requiring significant optimization of MOCVD growth conditions. In this case, rudimentary device creation allows for some insight to improvements in material quality. Once sufficient crystal quality can be achieved, device development and optimization can begin, allowing for realization of devices with increasingly long wavelengths. Finally, red-emitting μLEDs with high efficiency are realized and heavily characterized after development of the p-side structure and active region.

The significant reduction in material quality with increasing In content is due to several material issues, such as the large lattice mismatch between the GaN buffer layer and the InGaN QWs [83], the low miscibility of In in InGaN at growth temperatures, [84] and alloy fluctuations or phase separation [28]. To increase the indium composition and obtain red wavelength emission, a lower growth temperature of InGaN QWs is required due to poor In incorporation from desorption at higher temperature. Lower growth temperatures typically result in generation of defects and material deterioration [83]. Moreover, growth on the c-plane of GaN results in a large piezoelectric polarization in the direction of charge transport which is applied across the active region. The piezoelectric polarization then leads to the QCSE, where the electron and hole wavefunctions separate within the QWs, causing further reduction in the IQE [85]. Alternative GaN orientations such as semipolar and nonpolar have shown promise to push towards longer wavelength by reducing the effective polarization in the direction of charge flow, but a challenge remains in scalability of such substrates as they remain available only in very small sizes at very high prices [86, 87, 88, 89].

Requiring high In content active regions results in a number of growth issues, namely relaxation and phase separation, making optimization of strain conditions, material quality and In incorporation necessary for realizing red emission. One method to realizing a stable device architecture free from these issues is to grow the entire device out of InGaN of varying In content rather than primarily GaN with an InGaN active region. Special consideration will have to be taken for all-InGaN based devices. Namely, H_2 would have to be used sparingly if at all, as it will etch In leaving behind poor crystal morphology and only GaN. Temperatures would also have to be highly controlled at all steps, as they not only affect general crystal quality but also In content- parameters which may have independent effects. Building on previous knowledge and recent developments in green LEDs, V-pit engineering will play an increasingly important role, as they can be detrimental or advantageous depending on their location and are generated at threading dislocation sites which are more prevalent in strained InGaN. As evidenced by the ultralattice device experiments, these lead to injection closer to the n-side of the device and/or leakage. To first order, removing these V-pits from our buffer layers is desired to improve performance, possibly employing them in the future for 3D injection in the active region. Finally, strain considerations must be minded for all-InGaN devices, as high-In content layers will undoubtedly receive less compressive strain from better lattice matching, the reverse is true for pure GaN which will be in tension due to its smaller lattice constant than any InGaN alloy. This tension may lead to cracking if too large or may be advantageous in further offsetting strain.

4.2 Comparison of III-Nitride and AlInGaP Devices

Fundamental behavior of identical devices fabricated from III-N and AlInGaP materials was compared in order to gain insight to the potential material advantages III-N despite its significantly shorter development time. The c-plane III-Nitride LED wafer was grown on patterned sapphire substrate using atmospheric MOCVD with the epitaxy details and structure have been reported elsewhere [42, 40]. The commercial AlInGaP wafer was grown on a GaAs substrate and provided by Seoul Viosys Co. The device fabrication followed the same procedures in previous reports [90, 91]. To realize similar light extraction efficiency in the two sets of devices, atomic-layer deposition (ALD) sidewall passivation was employed to enhance the light output power and other device performance, but additional sidewall roughening techniques were not used [90, 91, 92, 93].

EL images of the InGaN red µLEDs, with sizes ranging from 100×100 to 10×10 μm^2, were captured at a variety of current densities (fig. 4.1a) to visually show the emission pattern. Identical response time was used for each sample to ensure identical hue perception on all images, and white balancing was used to most accurately portray the emission wavelength. Even with these conditions, saturation of the camera results in emission that appears near-white under high current density injection. All the EL images showed homogeneous light emission with no noticeable current crowding issues in the current density

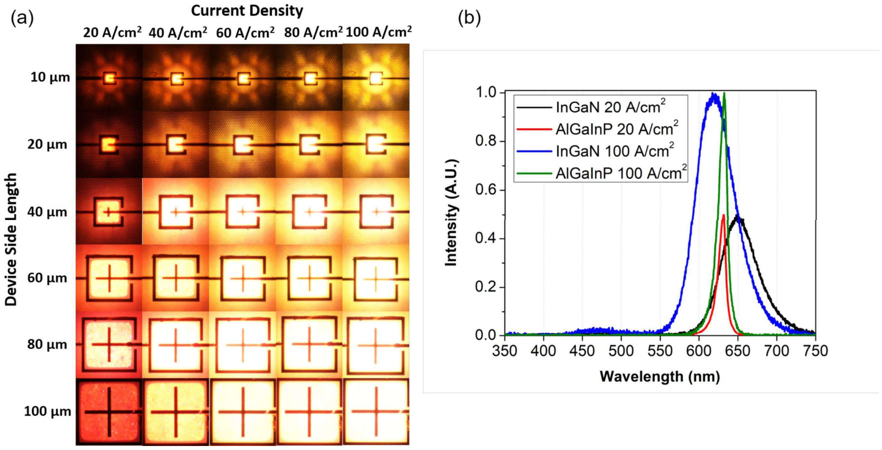

Figure 4.1: (a) Electroluminescence images of InGaN μLEDs with sizes ranging from 100×100 to 10×10 μm^2, at different current densities. The images were captured at the identical response time to preserve the same hue perception. (b) Emission spectra of selected 100×100 μm^2 devices at 20 and 100 A/cm^2 for both material systems

range examined, indicating good current spreading characteristics even for the larger μLEDs [94, 95]. However, the InGaN-based devices do demonstrate appreciable blueshift in color with increasing current injection, ranging from deep red to amber emission even by eye as the current density was increased from 20 to 100 A/cm^2. In contrast, the AlInGaP which had very little wavelength shift with increasing current density.

To further analyze the optical performance of InGaN μLEDs relative to AlInGaP μLEDs, room temperature emission spectra for 100×100 μm^2 devices at current densities of 20 and 100 A/cm^2 were taken for both InGaN and AlInGaP based μLEDs (fig. 4.1b). The AlInGaP μLEDs emitted at 631 nm with the FWHM of 11 nm, and the AlInGaP µLED emission spectra at 20 and 100 A/cm^2 were approximately identical with a difference of 1 nm in the peak wavelength and FWHM. The InGaN μLEDs yielded emission spectra with a peak wavelength of 647 nm and FWHM of 61 nm at 20 A/cm^2, a longer wavelength than the corresponding AlInGaP sample at the same current injection. However, at 100 A/cm^2 current injection the peak wavelength of the nitride sample blueshifted to 621 nm. Though still red emission, the InGaN μLEDs possess a shorter peak emission wavelength than AlInGaP μLEDs under high current injection. In addition to the main emission peak, a low-intensity peak at about 460 nm appears for both current injection levels. This peak is likely a result of recombination in the superlattice [63].

Devices fabricated from InGaN material showed a characteristic blueshift with increasing current density, where in contrast the AlINGaP devices exhibit extremely little blueshift. Even in optical EL images (fig. 4.1a), the emission can be seen as shifting from red to amber. However, the emission stays firmly in the red regime (>605 nm) throughout a wide range of current densities. indicating a true long-wavelength red emitter could be designed for a range of desired current density operations with slight tuning of the In content. According to Rec. 2020, the standard red primary color is considered to be 630 nm, yet the perceived hue from the EL image in fig. 4.1a appears to be slightly more orange than expected for its much longer nominal peak wavelength. The difference in perceived hue can be explained through both the FWHM of the InGaN μLEDs and the relative sensitivity of the human eye to different wavelengths [96, 97, 98]. Human eyes have three types of cone cells that are responsible for color perception, where the red cone cells have a peak sensitivity to a wavelength of approximately 564 nm. In the case of red emitters with narrow FWHM, perceived red emission would be consistent with the observed wavelength. However, as the emission FWHM broadens for red emitters, the perceived intensity of the emission wavelength, or color, is biased towards yellow due to peak eye sensitivity at much

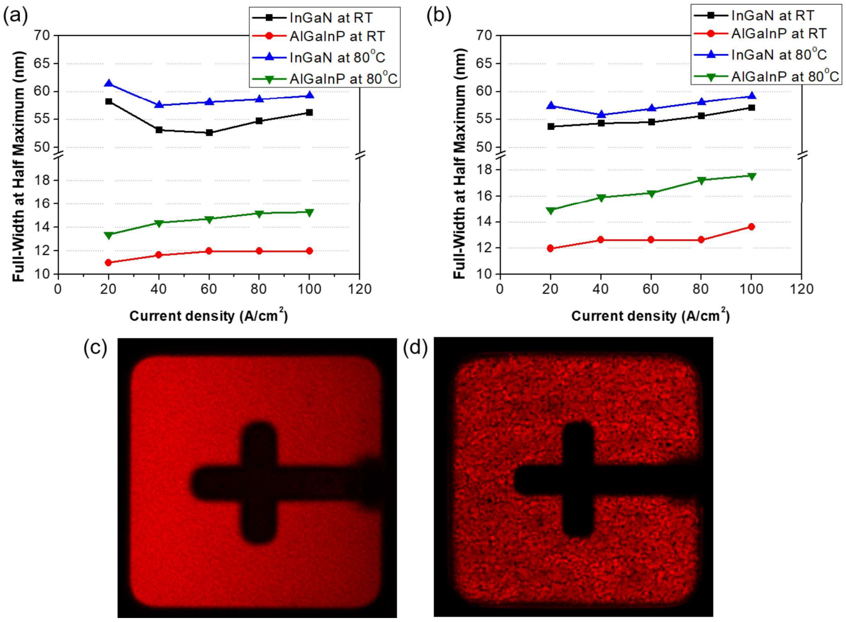

Figure 4.2: Current density dependence of emission FWHM for (a) 100×100 and (b) 40×40 μm^2 devices at both room temperature and 80°C. Confocal microscope images of (c) AlInGaP and (d) InGaN based devices indicating In distribution

shorter wavelengths than "true red" [97, 98]. From these considerations, the perceived hue of the InGaN µLEDs at 20 A/cm^2 is perceived as more orange or amber despite the actual peak wavelength being longer than the Rec. 2020 red primary color. Similar observations on long-wavelength InGaN devices using PL have also been reported [96].

In devices fabricated from both AlInGaP and InGaN material, the FWHM of the EL emission peak moderately increases both with temperature and current density (fig. 4.2). The broadening in FWHM is attributed to natural In alloy fluctuations in the QW. Confocal microscope images in fig. 4.2c and fig. 4.2d show In fluctuation and segregation for the InGaN device, leading to emission nonuniformity visible from the surface.

Since the FWHM of the emitting device is significant to color purity and position on the color gamut, the effect of temperature and device size on the EL emission FWHM is examined across a range of current densities. fig. 4.2a and fig. 4.2b indicate the behavior of the FWHM for both material systems across a broad current density range at room and elevated temperatures for selected device sizes. For the AlInGaP devices, the FWHM was below 20 nm for both device dimensions. Compared to other red emitters, namely self-emissive quantum dots, conventional organic-light-emitting diode (OLED) and liquid-crystal displays (LCDs) where the FWHM is about 30 nm, the AlInGaP devices yielded narrower FWHM, suggesting μLEDs could achieve purer red emission compared to these other sources in general [99, 100]. In the InGaN devices, slightly different behavior was observed. For the larger devices, the FWHM decreased and then increased gradually as current density increased. The FWHM of the smaller devices was narrower and widened with current density at a slightly slower rate than large devices, suggesting a more robust performance using μLEDs. In an absolute sense, the AlInGaP-based devices have a much narrower FWHM than InGaN devices; however, their change in FWHM with temperature greater than InGaN devices, and this effect is amplified at higher current densities. Additionally, comparing fig. 4.2c and fig. 4.2d emission nonuniformity can be seen in the InGaN device relative to the AlInGaP device. A small reduction in FWHM with decreasing device size in InGaN devices could be attributed from the carrier screening effect or the band-filling effect of the localized states with high-indium InGaN clusters [29, 101]. Conversely, for AlInGaP devices the emission FWHM increases with decreasing device size, an additional detriment to their weakening performance at small sizes. This observation further suggests that reducing InGaN device sizes could improve their optical performance and characteristics over larger devices, a useful feature for μLED applications.

AlInGaP devices emitted at a peak wavelength of 631 nm, shifting less than 2 nm with current density increasing from 20 to 100 A/cm^2 seen in fig. 4.3a. In contrast, InGaN devices had a significant blueshift in peak wavelength of approximately 33 nm over the same current density range. Peak wavelengths were converted into the CIE color coordinates, shown in fig. 4.3b, to determine the effect on the color gamut from the FWHM and current density injection. The Rec. 2020 red coordinate (0.708, 0.292) was used as a reference to determine the color emission of the devices from each material. Because the peak wavelength was nearly constant with current density for AlInGaP devices, the color coordinate at (0.698, 0.302) was similarly constant as current density increased. Additionally, the AlInGaP device emission coordinate was nearly identical to the Rec. 2020 coordinate. The color coordinate of InGaN µLEDs was heavily affected by the blueshift brought on with increasing current density, from (0.658, 0.308) at 20 A/cm^2 to (0.637, 0.341) at 100 A/cm^2, as well as the larger FWHM allowing more contribution to the CIE coordinates from shorter wavelengths.

In addition to the effect of FWHM on color purity, the peak wavelength is also an important factor in terms of color gamut. For AlInGaP, the peak wavelength remains relatively constant, with only a slight increase seen as the current density increased (fig. 4.3a). The slight increase in peak wavelength could be attributed to a junction temperature increase at high current density [102]. Conversely, a significant blueshift in the peak wavelength can be seen as the current density increases for InGaN devices This blueshift arises from the quantum-confined Stark effect (QCSE) caused by the piezoelectric field at the active

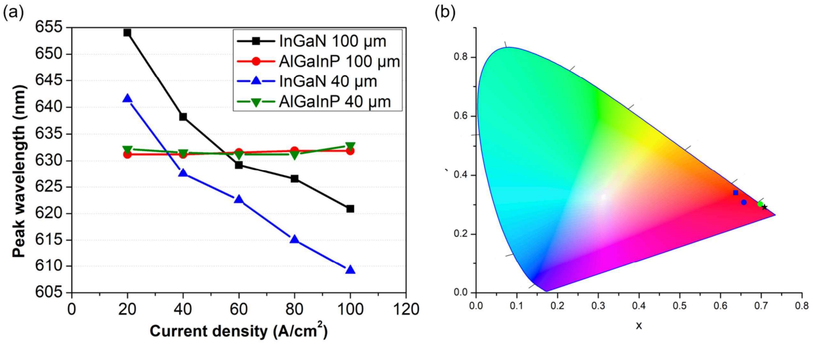

Figure 4.3: (a) The dependence of peak wavelength on current density of 100×100 and 40×40 μm^2 devices at room temperature. (b) The color coordinates plotted on the CIE 1931 diagram, where the Rec. 2020 red coordinate is indicated by a black star, the 100x100 μm^2 InGaN device at 20 and 100 A/cm^2 are represented a blue circle and square, respectively, and the 100×100 μm^2 AlInGaP device represented by a green square.

region; a well-studied phenomena for long-wavelength InGaN emitters [29, 96, 102, 103]. The InGaN device also emits at the same wavelength as the AlInGaP device at a given current density. Therefore, the critical developments necessary to utilize red InGaN μLEDs for display applications are to suppress the blueshift in wavelength with increasing current density and to minimize the FWHM, both feasible goals with further development time.

Many research avenues showing low blueshift and narrow FWHM in long-wavelength InGaN devices have been demonstrated, such as employing free-standing semi-polar GaN substrates [96, 104]. However, the scalability of semi-polar substrates remains difficult, where millions of devices are needed at high throughput and low cost. Methods to improve the FWHM of InGaN devices at long-wavelengths typically involve suppressing the In fluctuations mentioned above. Research groups have employed various methods of fluctuation suppression, including optimization of growth conditions during the QW growth [30, 76, 25], introduction of superior QW capping layers [105, 69], and improvement of

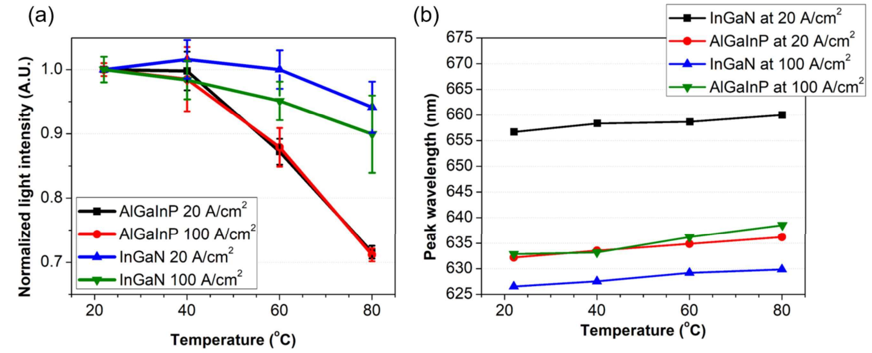

Figure 4.4: The dependence of (left) normalized light output power and (right) peak wavelength from 40×40 µm^2 AlInGaP and InGaN devices at 20 and 100 A/cm^2 on temperature

the QB growth in a MQW system [106, 76]. Since much focus is already being currently given to the reduction of FWHM in InGaN devices, this parameter will likely be reduced with further development time. Recently, reports on improved long-wavelength c-plane InGaN device performances have also been reported, arising from strain engineering methods [47, 107].

Despite the necessary and ongoing improvements in InGaN-based red devices, fig. 4.4a emphasizes that InGaN devices provided a relatively stable light output power with increasing temperature, whereas the optical power of AlInGaP devices sharply decreased. The InGaN devices yielded 5-10% reduction in light output power as temperature increased from room temperature to 80°C, depending on the different driving current densities (20 and 100 A/cm^2). In this experiment, the AlInGaP devices lost 13% and 30% of optical power at 60°C and 80°C, respectively, indicating a marked difference in the thermal performance characteristics of the device.

Apart from temperature-dependent light output power, the AlInGaP and InGaN devices also displayed different temperature-dependent wavelength characteristics (fig. 4.4b). The AlInGaP device emission wavelength redshifted with temperature, an effect more noticeable at higher current density operation. The redshift with increasing temperature was 0.069 and 0.097 nm/°C at 20 and 100 A/cm^2, respectively. Redshift in wavelength was also observed in the InGaN devices, similar to previous results that have been reported from larger LEDs with similar epitaxy structures [42, 40, 103]. To demonstrate this, the shifts in peak wavelength with temperature are compared for 100×100 and 40×40 μm^2 InGaN devices (fig. 4.5). The InGaN based devices, for both 40x40 and 100x100 μm^2 μLEDs, showed a small redshift behavior with temperature. AlInGaP devices demonstrated a temperature redshift of 0.0663 and 0.0942 nm/°C at 20 and 100 A/cm^2, respectively. The larger 100×100 μm^2 InGaN devices showed a small redshift rate of 0.005 and 0.0613 nm/°C at 20 and 100 A/cm^2. The other trends produced by the 40×40 μm^2 device yielded redshift rates of 0.0552, and 0.0555 nm/°C at 20 and 100 A/cm^2, respectively. These results illustrate a more thermally robust system with InGaN devices compared to AlInGaP devices.

Light output power is reduced with increasing temperature for both material systems, (i.e. "thermal droop") [102]. The decrease in light output power was more pronounced when operating the devices at 100 A/cm^2 (fig. 4.4a), most likely due to higher junction temperature and greater thermal droop effect at this larger current density. On the other hand, the AlInGaP devices showed the same trend with temperature independent of the applied current density, indicating that AlInGaP and InGaN devices have distinctive mechanisms for the optical power lost. At elevated temperatures, the fundamental luminous efficiency of AlInGaP emitters diminishes because of the direct-indirect (Γ-X) bandgap transition, where the carriers begin to increasingly occupy the indirect X-valley and result in significant indirect bandgap recombination [98]. Since this issue is fundamental to the electronic band structure of the AlInGaP material, developing improvements to growth conditions or device production will not yield a change in this bandgap transition. In this sense, the InGaN devices have a significant and fundamental advantage over AlInGaP devices due to its thermal performance. Redshift in peak wavelength was also noted (fig. 4.4b), which is attributed to bandgap shrinkage at elevated temperature [40, 98, 103]. However, this redshift is approximately half that of AlInGaP, indicating a more thermally stable system. Finally, the peak wavelength behavior with elevated temperature was investigated (fig. 4.5). As expected, elevated temperature causes a slight redshift in these InGaN-based devices. Smaller devices yield redshifted peak wavelength emission across the temperature range examined. Here again, the AlInGaP devices demonstrated larger redshift in emission compared to InGaN devices, At higher temperatures, InGaN offers a more stable power and emission wavelength output.

The optical comparisons between InGaN and AlInGaP µLEDs were discussed in terms of their device and material characteristics. Devices fabricated from the technologically mature AlInGaP showed a consistent peak wavelength emission at 631 nm and narrow FWHM less than 20 nm, with AlInGaP µLEDs offering outstanding color gamut factors according to Rec. 2020. In contrast, devices fabricated from the less mature InGaN red emitters still require improvement in terms of peak wavelength stability and wide FWHM, but offer significantly improved thermal performance at a fundamental material level. In terms of thermal performance, AlInGaP devices encountered a rapid decrease in light output

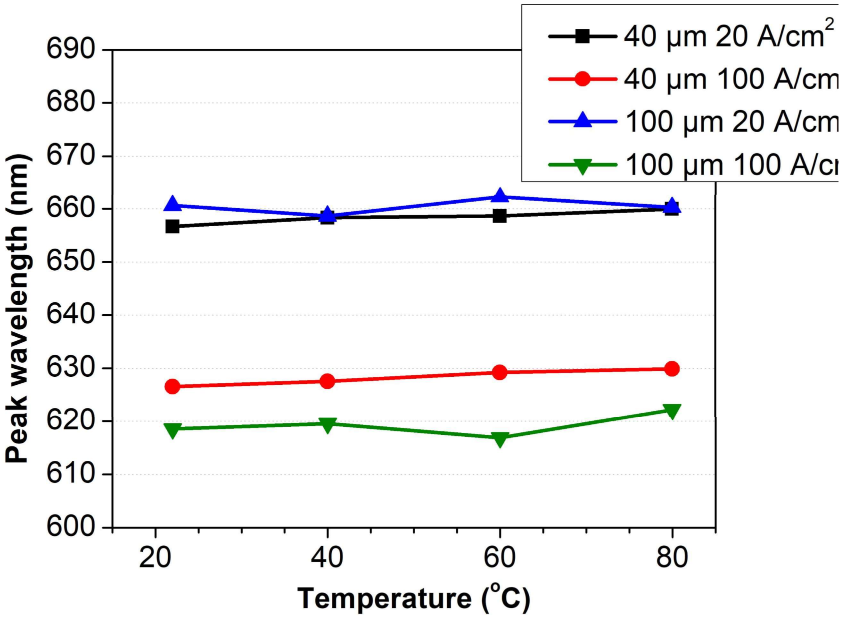

Figure 4.5: The dependence of peak wavelength of 100×100 and 40×40 μm^2 InGaN devices at 20 and 100 A/cm^2

power and redshift in emission wavelength with increasing temperature, while InGaN devices yielded more stable characteristics against elevated temperature. For InGaN devices, a shift in emission peak wavelength is driven by two competing mechanisms that can lead to blueshift or redshift elevated temperatures, ultimately causing very little emission wavelength shift with temperature for typical devices. In this sense, the InGaN-based devices have a fundamental material advantage over AlInGaP-based devices despite their shorter development time to date.

4.3 SoiTec InGaNOS and Substrate Design

Relaxed GaN and InGaN templates allow the enlargement of the material's lattice constant and have been previously used in a variety of forms to help mitigate strain in InGaN-based systems (e.g. growth on porous GaN, growth on semi-relaxed InGaN templates, etc.) [11, 108]. This allows for lowering of lattice mismatch difference between the high In% light emitting active region and the underlying materials. These changes yield numerous advantages in later growth such as QCSE reduction, lowering the risk of plastic deformation via defect formation and enhanced indium incorporation in the QWs. Such advantages over conventional GaN-on-Sapphire base layers are critical for optical devices emitting in the long wavelength visible range [109]. Even et al. [19] have shown a higher indium incorporation efficiency in InGaN heterostructures grown on partly-relaxed InGaN pseudo-substrates. The challenge in this InGaN growth, however, remains in the formation of V-pits. These V-pits are undesirable as they are uncontrolled in terms of density and formation onset and reduce crystal quality through defect propagation as the crystal is grown epitaxially [21].

Substrates employing a relaxed InGaN layer to achieve a larger lattice constant can be used to reduce these lattice mismatch stresses. In this work, relaxed InGaN substrates with an enlarged lattice constant are employed to grow high-In epilayers. The enlarged lattice constant employed by these relaxed InGaN substrates compared to GaN leads to a reduction in compressive stress during growth in the as-grown layers, most significantly the active region quantum QWs [11]. The compositional pulling effect also plays a role in these layers, where the incorporation efficiency of In decreases as strain becomes larger due to increasing lattice mismatch and resulting deformation energy of alloying the In atoms [12, 13, 14]. As a result, mitigation of the compositional pulling effect through strain reduction in the high-In layer directly leads to an improvement in In incorporation efficiency [15]. Additionally, the reduction in strain resulting from use of a relaxed InGaN substrate can also yield improved crystal quality in the QW through strain-generated defect reduction, resulting in higher PL efficiency than conventional GaN-on-sapphire growth [17, 18].

Relaxed InGaN Buffers (RIBs) have been used in a variety of forms to help mitigate strain. Lattice mismatch and strain are relieved as the LED is grown on the RIB with better lattice and thermal match, with the RIB absorbing some of the strain from the LED structure and ultimately causing lower strain and better In incorporation in the active region. This principle guided the use of SoiTec “semi-relaxed, semi-bulk” c-plane InGaN substrates for growth. These substrates employ nominally 8% In, with relaxation % tunable based on the separation of the proprietary “smart-cut” [110] slices which actually relax the substrate. This relaxation leads to an enlarged lattice parameter, changing the strain conditions to reduce compressive strain during QW growth, reducing the strain-induced compositional pulling effect [18] and allowing for better In incorporation. Despite the advantages of a relaxed InGaN substrate for lattice matching and In incorporation, the substrates are of inferior material quality, with extremely broad x-ray rocking curve peaks (fig. 4.6) indicating high dislocation density. Additionally, these substrates have many V-pits present; left unchecked, these pits propagate and enlarge through the entire diode, leading to extremely poor morphology. These effects will need to be carefully managed in order to take advantage of the benefits of the relaxed substrate.

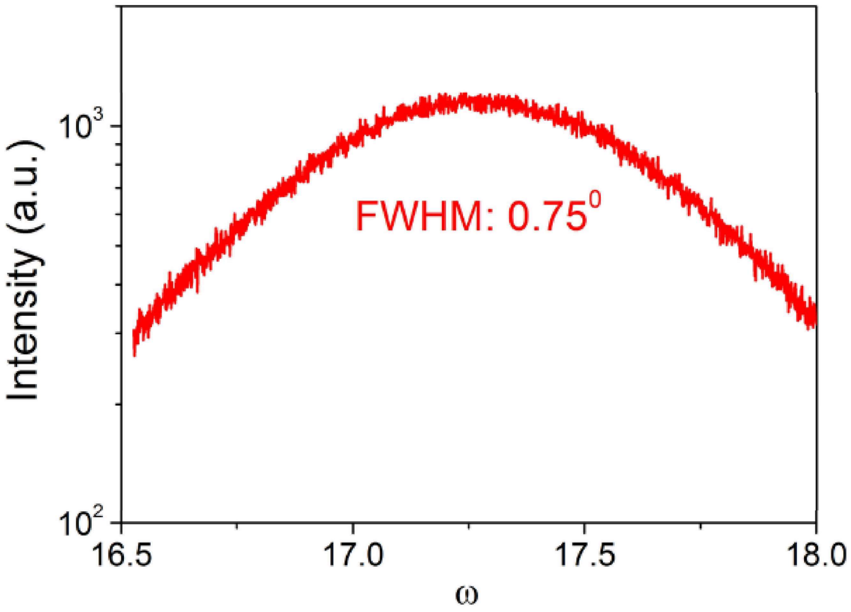

Figure 4.6: X-ray rocking curve of relaxed InGaNOS substrate. Large peak FWHM indicates poor crystal quality.

Chapter 5

Epitaxy of Thick InGaN Buffers to Achieve High Quality Material

5.1 Poor Quality Initial Structures and Interlayer Architecture

The substrates used in this work are provided by SOITEC, a private industry company, and will be referred to as "InGaNOS" substrates. They consist of 490x490 μm^2 InGaN mesas spaced 10 μm apart. Each InGaN mesa is 150 nm thick and has a lattice constant of 3.205 Å, transferred on top of a buried oxide on a 4-inch sapphire substrate. fig. 5.1(a) shows an image of the 4-inch substrate and fig. 5.1(b) shows a microscope image of the semi-relaxed mesas. These templates employ nominally 4 % In, with relaxation of 54% which is tunable using SOITEC's proprietary Smart-Cut technology. Finer details on the substrate process, fabrication and structural and optical quality can be found in ref [19]. From a structural perspective, the epi-ready InGaNOS substrates contain a density of pre-existing V-

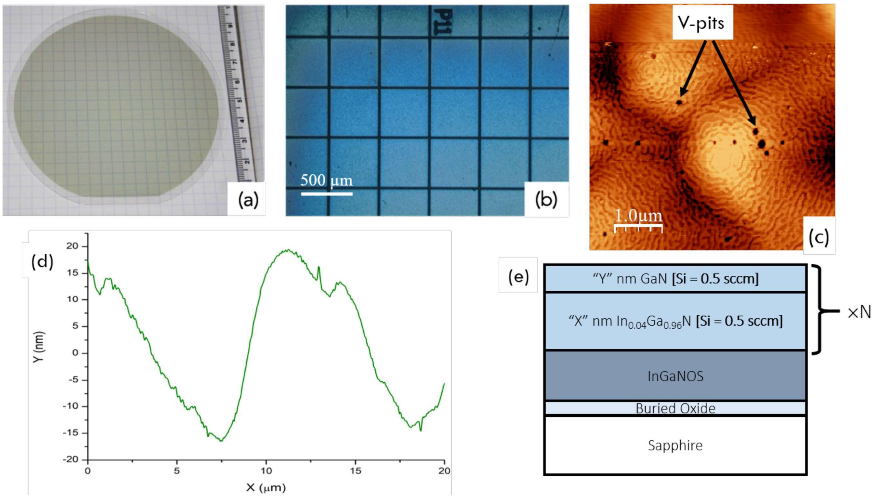

Figure 5.1: (a) photo of 4" InGaNOS wafer (b) Microscope image of relaxed InGaN "array" of 500μm^2 pitch on InGaNOS (c) 5x5 μm^2 AFM image of InGaNOS substrate, (d) line scan height profile over 20 μm of InGaNOS substrate, and (e) structure of base layer growths on substrates with N periods of X and Y nm of InGaN and GaN, respectively.

pits around 5x10^8 cm^{-2} (see fig. 5.1(c)), and possess (002) X-ray reflections FWHM around 2600 arcsec (not shown). Also as shown in fig. 5.1(c, d) the material exhibits a morphologically undulated surface with "peaks and valleys" having heights fluctuating between zero and up to 60 nm.

In order to improve the poor material quality of the substrate, an InGaN base layer would need to be grown. The Si-doped InGaN base layer optimization structures were grown by MOCVD at atmospheric pressure on the InGaNOS substrates in a horizontal two-flow reactor setup with vertical carrier gas subflow. Details on the design features of this reactor can be found elsewhere [66]. The objectives of such layers are: 1) maintain a smooth morphology, 2) ensure that the layers are silicon doped as they will later serve as the n-contact layers for the subsequent μLED growth and 3) fill pre-existing V-pits to avoid leakage paths in devices. Si concentrations of 5x10^{18} cm^{-3} are targetted for the n-type InGaN:Si region doping. The InGaN is grown at a constant growth rate of 3 Å/s, using TEGa, TMIn, and (NH_3) as the precursors for GaN and InGaN growth and Si_2H_6 as precursor for the silicon dopant with nitrogen and hydrogen as carrier gasses.

Since V-pits originate from the substrates and also need to be filled during InGaN:Si base layer growth (in addition to the previous concerns), a wide variety of growth conditions are examined to improve the morphology of InGaN base layers grown on the semi-relaxed InGaN substrates provided by SOITEC. Developing a general method to eliminate already-formed V-pits on relaxed InGaN substrates then allows for further development of long-wavelength InGaN-based devices on these substrates. The use of various growth stack architectures and GaN interlayer schemes are examined, the implementation of which was previously reported to improve the quality of thick InGaN layers [111]. After, V/III ratio and carrier gas identity and amount were examined to improve the roughness and reduce the number and size of the V-pits. Finally, increasing the growth temperature of the GaN interlayers is examined, eliminating any generated V-pits and creating a smooth morphology for later growth. By eliminating pits stemming from the substrate, all the benefits of the relaxed substrate are leveraged for further growth of long-wavelength devices.

Material quality will need to be carefully managed in order to take advantage of the benefits of the relaxed substrate during later growth. By growing initial, unoptimized thick InGaN layers directly on the templates, significant roughening is observed, which is likely associated with lateral In fluctuations causing a transition from 2D to 3D growth modes as indicated by Van Der Brock et al [112]. With employing thick InGaN layers, In segregation is also commonly observed, with two distinct composition regimes arising that

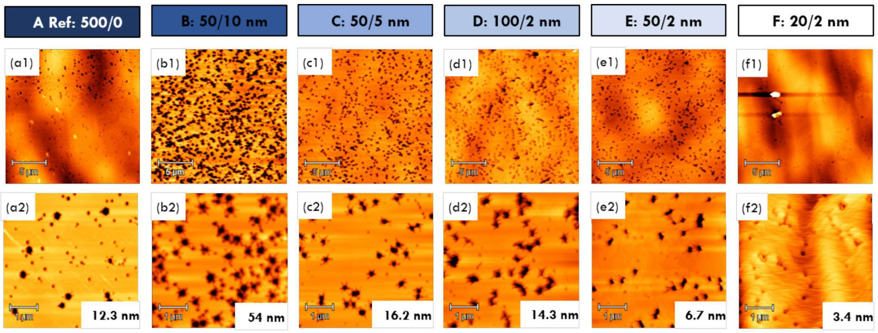

Figure 5.2: AFM images 20 μm x 20 μm (top row) and 5 μm x 5 μm (bottom row) of samples with different InGaN to GaN interlayer ratios, with the first number corresponding to the InGaN, and the second to the GaN interlayers' thickness, showing the V-pit density variation and RMS roughness value for each 5 μm x 5 μm scan. The total InGaN base layer thickness was 500 nm for A, 540 nm for B, 520 nm for C, 510 nm for D, 516 nm for E, and 506 nm for F, as close to 500 nm as periodicity will allow.

are easily measured by photoluminescence resulting in a double peak [111]. By adding periodic interlayers of GaN within the InGaN layers, the excess indium is absorbed/alloyed into the material, preventing a transition to a 3-dimensional growth mode and maintaining a planarized 2-dimensional growth mode, as shown by Pantzas et al, [111]. Different schemes of interlayer thicknesses as well as the InGaN layer/GaN interlayer thickness ratios are examined. For starting growth conditions, a "moderate" NH_3 flow of 3.2 SLM under N_2 carrier gas at 950°C are used for the base layer and interlayer growth. As shown in fig. 5.2(a), the reference growth of 500 nm of InGaN retains and enlarges the pre-existing V-pits, indicating a necessity for growth interlayers to improve poor morphology.

fig. 5.2(b-f) shows 20 μm x 20 μm (top row) and 5 μm x 5 μm (bottom row) AFM of the film surfaces of InGaN base layers containing GaN interlayers with varying interlayer thicknesses and InGaN:GaN layer thickness ratios: b) 5:1, 10 nm interlayer c) 10:1, 5 nm interlayer d) 50:1, 2 nm interlayer, e) 25:1, 2 nm interlayer f) 10:1, 2 nm interlayer. The resulting V-pit density for the InGaN base layer in each sample was a) 3.48e8, b) 3.72e8, c) 1.64e8, d) 2.24e8, e) 1.72e8, and f) 1.52e8 cm^{-2}. In developing the optimal thicknesses for the InGaN and interlayers, thinning both the InGaN layers and interlayers proved advantageous. Comparing samples with the same InGaN thicknesses but varying interlayer thicknesses (Samples B, C, E), the density and size of V-pits seems to decrease significantly with thinner interlayers, corresponding to a similar decrease in roughness. This indicates the reduction in interlayer thickness allows for avoiding the 3D growth mode while minimizing negative effects of nominally pure GaN growth, such as tension generation from the relatively smaller lattice parameter. These effects combined aid in suppressing some of the V-pit nucleation and propagation.

In addition, comparing samples with varying InGaN thicknesses but equal interlayer thicknesses (Samples D, E, F) shows a similar but independent decrease in pit size and density with decreasing InGaN thickness with an additional decrease in roughness. For both the InGaN layers and the GaN interlayers, reducing each layer thickness independently showed a monotonic decrease in both pit density and pit size creating more well-defined layer morphology. By reducing the InGaN thickness before a growth "reset" with a GaN interlayer, pit propagation and the amount of pits in this layer are reduced. Less surface riding In can accumulate and act as a surfactant to lower the energetic barrier of pit nucleation. Ultimately, a 500 nm total buffer thickness was targeted, and by changing the thickness of each period, the total number of periods was altered to maintain a constant overall thickness. With the overall thickness held constant, it is concluded that the introduction of GaN interlayers and subsequent thinning of the GaN interlayers and the InGaN buffer layer allowed for much stronger suppression of V-pit formation.

5.2 V/III Ratio and Carrier Gas

Once the thickness and periodicity limits of the base layer stack had been determined as a starting architecture, attention was turned to improving the InGaN base layers through V-pit reduction by optimization of the V/III ratio and the carrier gas identity and flow during deposition. For these samples, the 20/2 nm base layer architecture was adopted as it was the most superior architecture examined. Firstly, growing the GaN interlayers in H_2 rather than N_2 to improve growth morphology through impurity reduction [113, 114] and improved surface mobility through diffusion is attempted. Both growth in pure H_2 free from N_2 are examined, as well as a condition called the hydrogen “injection” condition of introducing 200 sccm H_2 in an otherwise entirely N_2 flow. From AFM results, use of H_2 in the GaN interlayers clearly decreases the density of V-pits over using only N_2 by approximately an order of magnitude (fig. 5.3, Samples F, G) from pit counting in a known, representative area. Among the conditions examined, the "hydrogen injection" condition, sample H, with 10% H_2 in the carrier gas during interlayer growth, appeared to show the largest improvement in morphology (fig. 5.3). Compared to the optimized InGaN architecture grown in pure N_2 (Sample F), the V-pit density and size for the "hydrogen injection" sample were reduced while retaining step-flow growth, a hallmark of improved epi design.

Next, the NH_3 flow is reduced in the entire base layer to increase Ga adatom surface mobility by employing a lower V/III ratio during base layer growth, leading to ad-

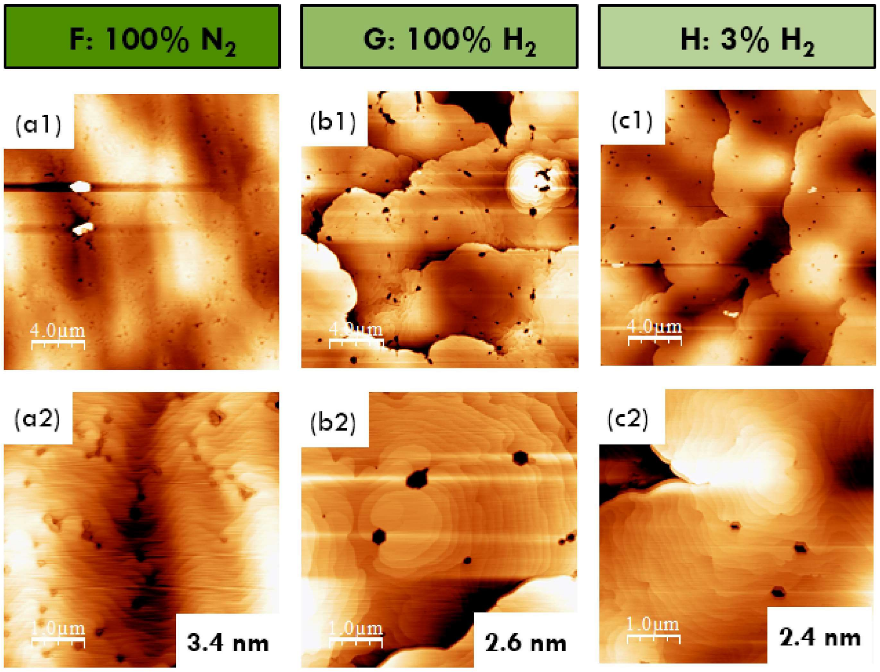

Figure 5.3: AFM images sized 20 μm x 20 μm (top row) and 5 μm x 5 μm (bottom row) of the 20/2 nm InGaN/GaN samples with varied H_2 carrier gas amounts during GaN interlayer deposition

ditional improvements to InGaN:Si layer morphology. These samples now employ the hydrogen injection condition in the interlayers in addition to the optimized architecture. In this case, the standard "moderate" starting condition of 3.2 SLM NH_3 is varied in both directions, examining 5 SLM and 1 SLM NH_3 flows. Reducing the NH_3 flow from 5 to 1 SLM showed a steady reduction in V-pit generation (fig. 5.4). this is attributed to an improved lateral mobility of surface adsorbed Ga and In species at low V/III ratio arising from this reduced NH_3 flow, leading to an enhancement of lateral growth on the V-pit sidewalls and subsequent V-pit size reduction. Sample K represents the lowest V/III ratio, the lowest V-pit density, and the lowest roughness measured of all samples in this series. It is determine that the V/III ratio and composition of the carrier gas are important factors in controlling V-pits and morphology. Also, from fig. 5.5, it is clear that the growth conditions also proportionally impact the optical properties of the material, where PL intensity has shown to improve as the density of V-pits is reduced.

With each successive improvement to the base layer architecture, the PL intensity noticeably increased, indicating a decreasing amount of nonradiative recombination centers (fig. 5.5). These nonradiative recombination centers typically consist of defects and impurities, and as a result their reduction directly results in an increase in quality of the material. This is further reflected in rocking curve measurements, reducing the FWHM of the (002) reflection from 2600 arcsec in the substrate to approximately 1150 arcsec noting a significant material improvement compared to the starting substrate.

As PL measurements were done at room temperature, no PL emission was observed from the thin GaN interlayers, likely due to thermal injection of the photo-generated

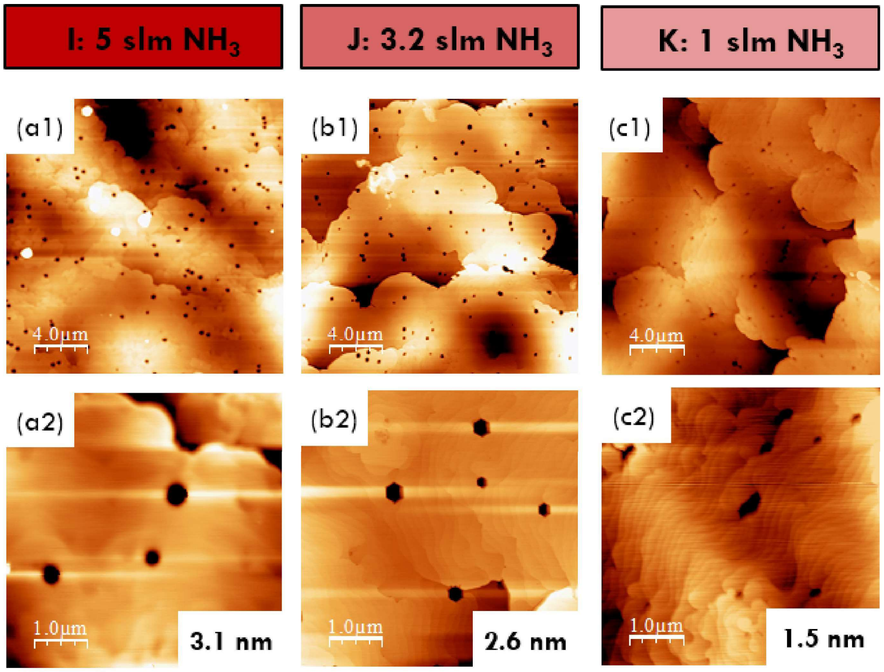

Figure 5.4: AFM images (20 μm x 20 μm (top row) and 5 μm x 5 μm (bottom row) of the 20/2 nm InGaN/GaN samples with varied V/III ratio.

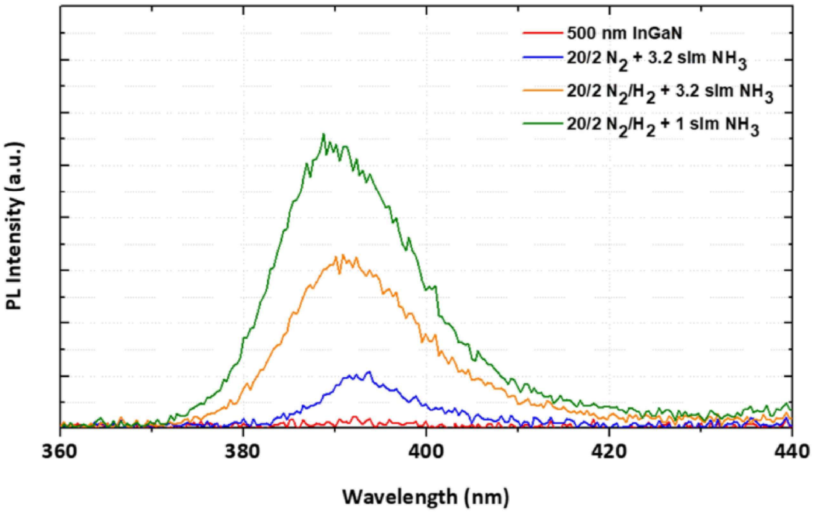

Figure 5.5: Photoluminescence spectra from selected base layer schemes and InGaN reference showing a single peak in the InGaN base layer region.

carriers into the smaller-bandgap and lower-potential thick InGaN layers where they radiatively recombined. For samples with thick interlayers (5 and 10 nm) no photoluminescence emission was observed at all due to the extremely poor material quality arising from a high density of V-pits. Reducing the InGaN layer thickness per period to its final value of 20 nm, along with thinning the interlayers to a final value of 2 nm, showed a remarkable decrease in overall V-pit size and density, vastly improving the crystal morphology and quality of the InGaN:Si base layers.

5.3 High Temperature Interlayers

In the following, the InGaN/GaN (20 nm/2 nm) interlayer design with GaN grown with 1 SLM of NH_3 and partial H_2 addition to the carrier gas are combined. The total buffer thickness is also increased to around 1200 nm to be more consistent with a typical device structure. As previously mentioned, in all of our previous series the whole InGaN/GaN buffer stack was grown at 950°C, while here the temperature of the GaN interlayers was increased to 1000°C, 1050°C and 1100°C. The AFM images of the surface of respective HT-GaN interlayer buffers are shown in fig. 5.6 (a-c).

It is clear that with the increase of the GaN interlayer growth temperature the V-pits are fully eliminated and a smooth surface is maintained even at a total stack thickness of 1200 nm, more than twice as thick as the previous InGaN base layer stacks. The elevated temperature during the IL growth results in significantly increased Ga adatom diffusion and increased incorporation on the V-pit sidewalls, filling them via enhanced lateral growth as

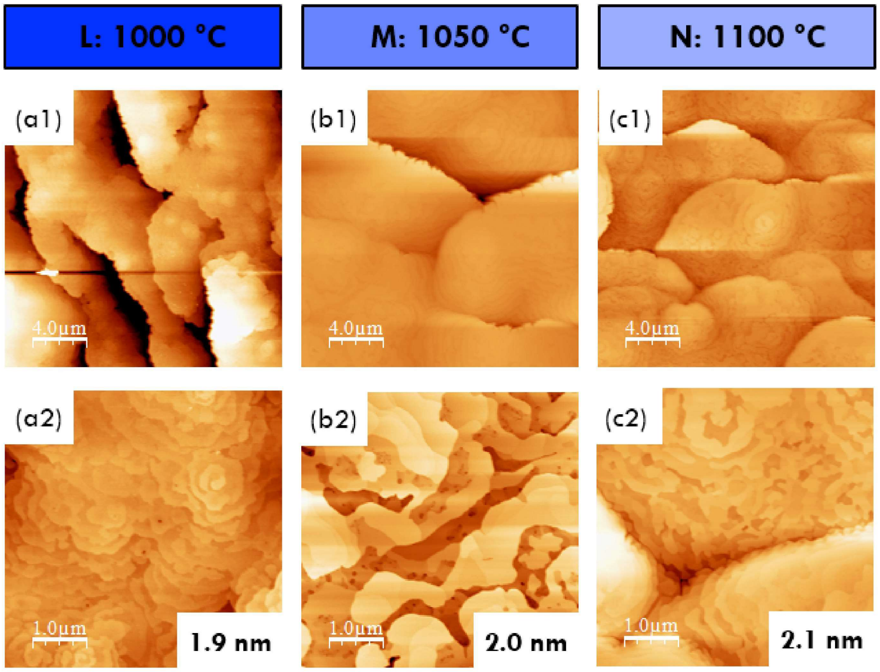

Figure 5.6: AFM images (20 μm x 20 μm (top row) and 5 μm x 5 μm (bottom row) of the samples with varied GaN interlayer temperature: (a) 1000°C, (b) 1050°C and (c) 1100°C.

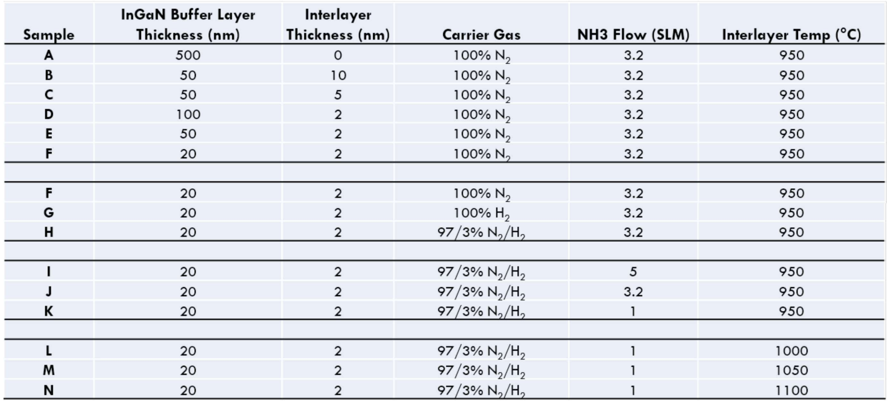

Sample	InGaN Buffer Layer Thickness (nm)	Interlayer Thickness (nm)	Carrier Gas	NH3 Flow (SLM)	Interlayer Temp (°C)
A	500	0	100% N_2	3.2	950
B	50	10	100% N_2	3.2	950
C	50	5	100% N_2	3.2	950
D	100	2	100% N_2	3.2	950
E	50	2	100% N_2	3.2	950
F	20	2	100% N_2	3.2	950
F	20	2	100% N_2	3.2	950
G	20	2	100% H_2	3.2	950
H	20	2	97/3% N_2/H_2	3.2	950
I	20	2	97/3% N_2/H_2	5	950
J	20	2	97/3% N_2/H_2	3.2	950
K	20	2	97/3% N_2/H_2	1	950
L	20	2	97/3% N_2/H_2	1	1000
M	20	2	97/3% N_2/H_2	1	1050
N	20	2	97/3% N_2/H_2	1	1100

Figure 5.7: Summary of growth conditions for each sample examined across all studies. Experiment sets are separated for clarity, with sample F reproduced as it was in the study.

previously seen with reduced V/III ratio. Varying the GaN interlayer temperatures showed little to no effect on the In content of the base layer, suggesting that the temperature ramp for the interlayer growth did not cause any significant indium desorption from the InGaN layers that make up the majority of the base layer. All 3 HT-GaN interlayer samples showed a removal of V-pits, although sample L, grown at 1000°C appeared to have the best morphology in terms of roughness and retained step-flow growth typical of high-quality MOCVD grown films. Further optimization may be needed to determine the best temperature of the HT-GaN interlayer samples in terms of later device performance. However, structurally and morphologically Sample L appears to possess a slight advantage over samples M and N grown at higher temperatures. A summary of all the sets of conditions examined is available in fig. 5.7.

To further investigate the mechanism behind the V-pits closing, the surface morphology is examined after only a set number of periods to determine any change in V-pit density. Using buffer growths interrupted after 1, 2, 5, and 15 periods of InGaN/GaN, AFM images were taken of the surface to monitor size and elimination of V-pits (fig. 5.8). Multiple AFM images for each sample were taken, using pit counting for each to calculate the statistical average pit density for each sample. The samples with 1, 2, 5, and 15 periods of growth, across all measurements taken on the sample, correspond to an average V-pit density of 1.24e8, 7.07e7, 1.40e7, and 0 cm^{-2} respectively. A clear trend in pit reduction can be seen as additional periods are grown, and V-pits are fully eliminated after 15 periods of InGaN/GaN growth as no pits were seen across multiple sample scans. Since a significant reduction in V-pit density occurs after even the first period when HT-GaN interlayers are employed, pits must begin closing immediately. This provides strong support to the hypothesis that the elevated temperature leads to enhanced Ga adatom diffusion and increased lateral growth rate, as this effect would be immediate and continuous through each period added.

Finally, high angular annular dark field imaging (HAADF) is employed on the buffer layers as shown in fig. 5.9(a) to gain insight to the structural quality of the buffer. The image shows a cross-sectional HAADF image of the optimized buffer structure in the [1-100] zone axis. The image contrast is dependent on the variation of the atomic mass numbers in the heteroepitaxial structure. The layers containing indium show much brighter contrast while the pure GaN interlayers show darker contrast. From this, sharp InGaN/GaN interfaces in the buffer and absence of any propagating V-pits can be seen. In addition, the thicknesses of the InGaN layers and GaN interlayers are measured as 20 nm and 2 nm, respectively, consistent with our XRD measurements and our targeted thickness values.

Also, fig. 5.9(b) shows a reciprocal space map measured along the GaN (-1-124) reflection for the sample M (GaN-IL grown at 1050°C) demonstrating a fully coherent 1200

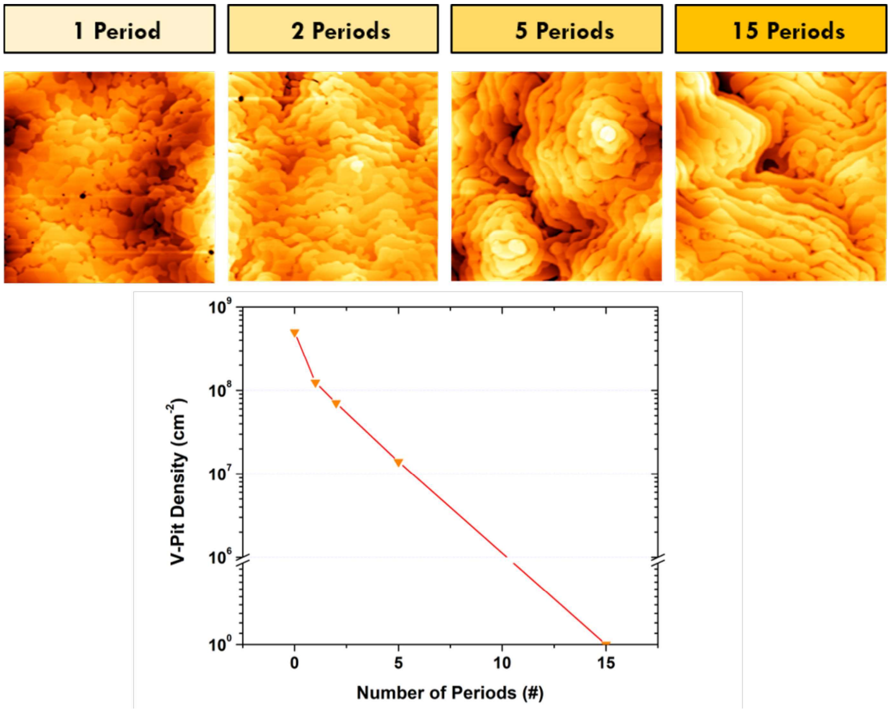

Figure 5.8: (top) 5 μm x 5 μm AFM images of growths interrupted after a specified number of InGaN/GaN periods grown. (bottom) Plot of V-pit density reduction with number of periods grown. Zero periods is the initial substrate pit density of 5e8 cm^{-2}. The 1, 2, 5, and 15 period samples correspond to a V-pit density of 1.24e8, 7.07e7, 1.40e7, and 0 cm^{-2} respectively

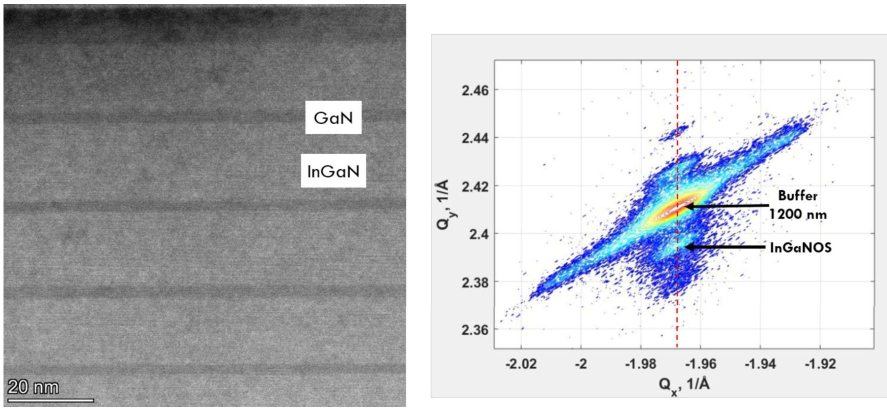

Figure 5.9: (a) HAADF image of the buffer InGaN layers and GaN interlayers showing sharp interfaces. (b) Interface at higher magnification. (c) RSM of the 1200 nm buffer with HT-GaN interlayers displaying vertically aligned peaks.

nm buffer layer the vertically aligned peaks. The growth is strained to the InGaNOS substrate without relaxation and with a slightly higher In content than the substrate.

One aspect that remains not fully understood is the "peaks and valleys" surface morphology seen in almost all growths which is clearly visible from the AFM images shown in fig. 5.6. They are characterized by island-like domains with edge depths that could vary from 10 nm up to 80 nm. This is likely due to the initial surface morphology of the substrates (see fig. 5.1(c)(d)), which is also characterized by these longer-range variations in surface height. During growth, this morphology often gets amplified as the thickness increases. Another possible explanation for this morphology is step bunching arising from local surface misorientations that result from the template, creating these large edge depths. When compared with the morphology of a co-loaded reference GaN-on-Sapphire template with the same stack, a very smooth surface and step flow growth is obtained (not shown) without any signs of surface undulation as seen on the InGaNOS substrates.

5.4 Blue and Green Test LEDs

I examine the application of these periodic InGaN/GaN base layer structures on relaxed substrates in the growth of μLEDs to enable emission across the entire visible spectra. Employing an InGaN/GaN interlayer structure with high temperature (HT) GaN interlayers, where the elevated temperature has shown to improve Ga surface diffusion and both fill pre-existing V-defects and suppress their subsequent formation [115], working μLED devices with appreciable electroluminescence emission across the visible range are enabled. For μLEDs grown on these InGaN/GaN base layers, a significant reduction in the V-defect density and an improvement to crystal quality results in appreciable electroluminescence readily visible even by eye. These resulting μLED devices were analyzed in terms of their emission spectra and current-voltage response to determine a baseline device performance and ensure diode-like behavior. Compared to previous devices grown on lower quality base layers, long-wavelength electroluminescence is enabled showing a significant increase to the emitted light intensity, achieving working μLED devices.

As the buffer region is developed, LED devices on the experimental buffers are grown and tested. These devices yield another indicator of material quality as higher quality buffers directly lead to better devices. Initially, our most advanced green active region was simply applied to our developed buffer replacing the AlGaN cap with a GaN cap and mimicked the buffer structure as a p-InGaN/GaN region. By co-loading the relaxed substrates with a bulk GaN substrate then testing both, one can visualize the difference in In incorporation as the emission wavelength changes, noting the much longer wavelength emission in the relaxed substrates. Occasionally, device architecture was optimized beyond the buffer layer as higher quality buffers were achieved. Since the p-InGaN/p-GaN region architecture is based on that of the n-buffer, many of the changes leading to improvements in the buffer were attempted on this region as well. LEDs on our most optimal buffer were examined with a p-InGaN/p-GaN region grown in both N_2 and H_2 conditions, electrically testing the resulting LEDs. However, in both cases, the LEDs fabricated displayed an immense amount of forward and reverse leakage current (fig. 5.10) that ultimately led to turn on at very high current density, heat generation, and catastrophic failure from the p-contact degrading. Significant current is seen under the turn-on voltage, likely from injection through the V-pits. Since the pits are generated in the substrate and then later terminate in the p-region, a direct injection path between the p-region and substrate would exist. Coupled with the low hole mobility in p-GaN, this injection path leads to leakage current and nonradiative recombination at the p-contact, generating heat until the contact fails. Due to the high leakage and rapid failure, comparison between LEDs with differing p-region conditions becomes very difficult here, and indicates the focus moving forward will remain on the buffer and reducing the V-pits in it.

I have examined growth conditions to optimize crystal quality and morphology of the InGaN:Si base layers grown atop "semi-relaxed" InGaN substrates to develop a path to workable long wavelength LED and μLED devices. By implementing GaN interlayers and replacing a single InGaN:Si layer with an InGaN:Si/GaN:Si periodic layer stack and examining the total thicknesses of the InGaN/GaN stacks, along with altering V/III and carrier gas ratios during deposition, a growth scheme for low roughness and reduced V-pit

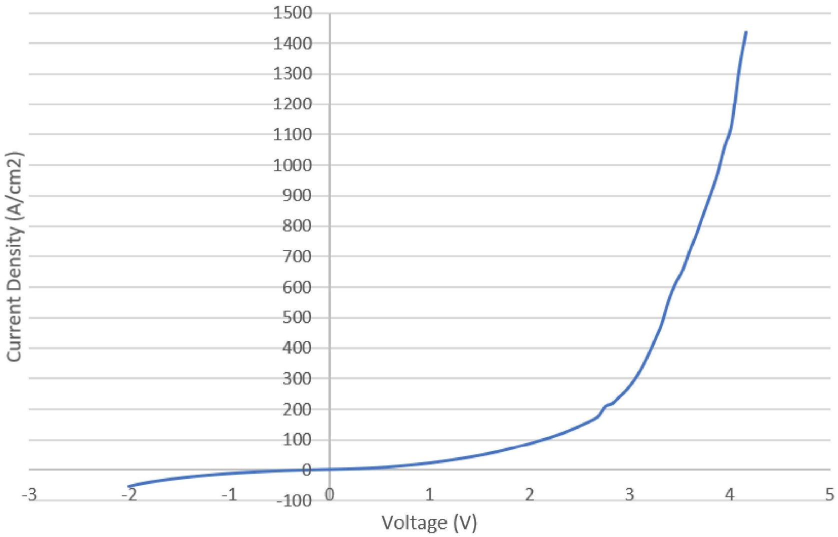

Figure 5.10: Current-voltage diagram of 80x80 μm^2 LED on relaxed substrate. Significant current density seen below turn-on and in reverse direction.

densities is developed. Finally, high-temperature GaN interlayers are used in the base layer stack to fully eliminate the V-pits. As such, the relaxed InGaN templates examined in this work are poised to offer an approach to superior In incorporation by leveraging the better lattice matching and lower material strain, while using the large fundamental knowledge base of MOCVD GaN/InGaN growth to reduce and eliminate morphological issues.

Chapter 6

Design and Epitaxy of Efficient Red LED Structures

6.1 Device Improvements From Better Buffer Material

μLEDs were fabricated from the two types of base layers, pitted (Sample A) and pit-free (Sample B), to compare the resulting electrical performance. fig. 6.1 shows AFM images of the 1200 nm base layer from Samples A and B, where growth was interrupted immediately before reaching the active region. In the non-HT interlayer, the images clearly indicate a high density of pits present after the growth of the base layer. In contrast, introduction of HT-GaN interlayers results in a total elimination of pits, creating a smooth surface with only the macro step-edges remaining. While the Si n-doping level is different between the two samples, it is likely unrelated to the propagation or filling of V-pits since these are kinetically controlled processes. Additionally, our work previously reported conditions for

V-pit elimination at higher n-doping levels than presented here, and these conditions were independent of Si doping. Despite being ineffective in controlling V-pits and lacking a contribution to their propagation in material grown on InGaNOS substrates, higher Si doping is expected to slightly reduce crystal quality in other ways due to its antisurfactant behavior [116].

Current density-voltage (JV) behavior for different size μLEDs grown on each type of base layer are shown in fig. 6.2 to illustrate these differences in electrical performance. The electroluminescence spectra for the fabricated devices is also shown, delineating the green wavelength emission at approximately 540 nm. Comparing the JV curves between μLEDs grown on the pitted vs. pit-free base layers, it is clear there is significant forward current below the turn-on voltage for the pitted samples while the pit-free samples appear to have little current at corresponding voltages. For both samples, 1.0 V is chosen as the forward voltage to determine the leakage current, as it was far below the turn-on voltage and large enough to generate forward leakage current in measurable amounts for both samples.

Leakage current for the pitted vs. pit-free base layer was compared for both device sizes, calculating a current density from the device size. The forward leakage current density decreased significantly for the devices grown on the Sample B pit-free buffer. From our measurements, the leakage current density at 1V for the 60 μm device dropped from 0.243 A/cm^2 to 6.74x10^{-3} A/cm^2 and the 80 μm^2 device dropped from 1.64 A/cm^2 to 1.84x10^{-3} A/cm^2 A/cm^2. Another notable factor of device performance is the lower dynamic resistance of the pit-free device, which is inversely related to the slope of JV plot after turn-on. The LED from the pit-free buffer qualitatively has a lower resistance than the LED from the pitted

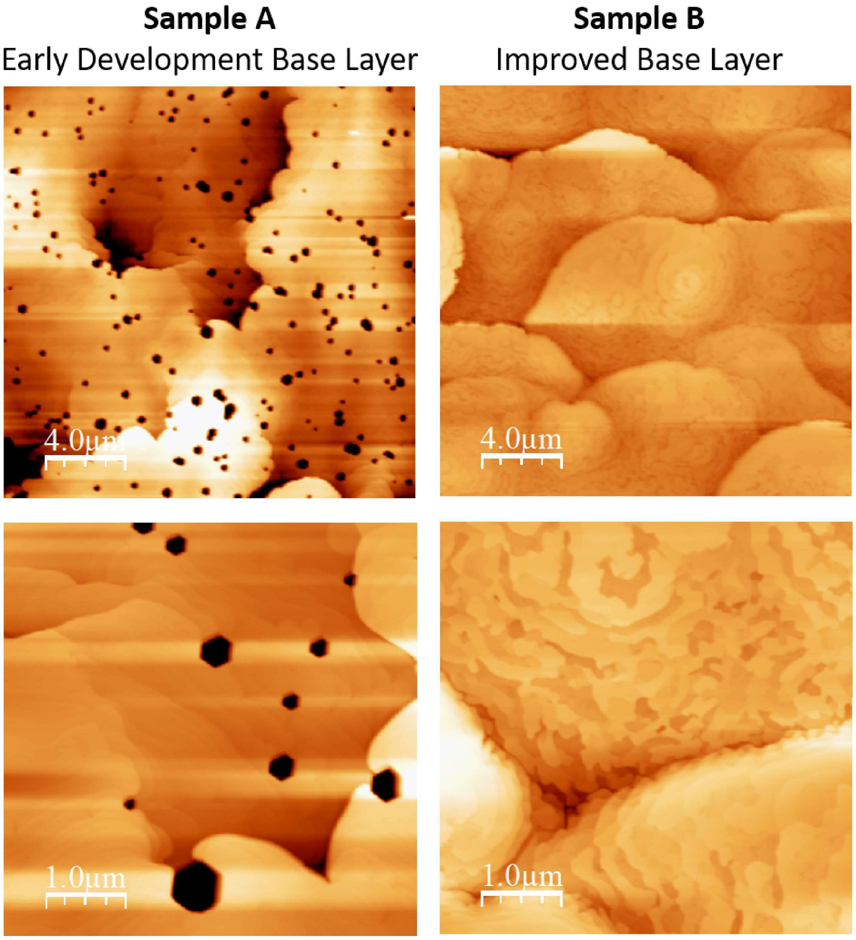

Sample A
Early Development Base Layer

Sample B
Improved Base Layer

Figure 6.1: AFM images 20 μm x 20 μm (top row) and 5 μm x 5 μm (bottom row) for a) standard 1200 nm InGaN/GaN base layer containing pits and b) 1200 nm thick InGaN/GaN base layer with HT-GaN interlayers with V-pits fully eliminated. Images taken immediately prior to active region growth.

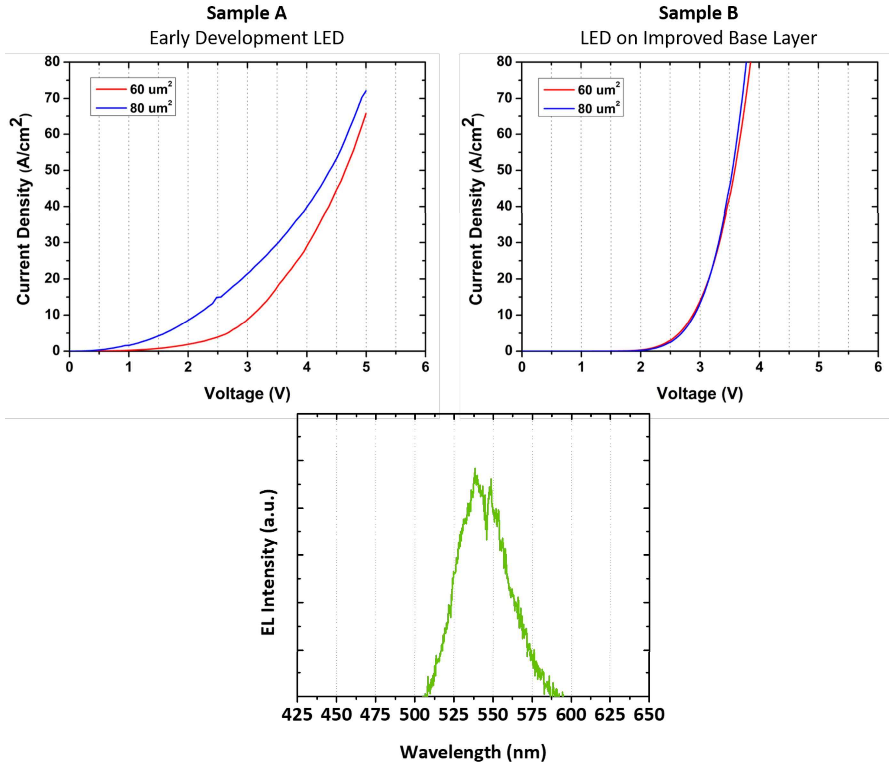

Sample A
Early Development LED

Sample B
LED on Improved Base Layer

Figure 6.2: Current Density-Voltage (JV) behavior of μLEDs containing a base layer (left) with pits (right) free from pits. Both 60 μm^2 and 80 μm^2 size devices are shown for each sample. (bottom) Representative EL emission spectra of μLED devices

buffer, which results in higher current density achieved at the same voltage. The significant leakage reduction and lower dynamic resistance is attributed to the elimination of V-pits, other growth defects, and nonradiative recombination centers, resulting in smooth layers and sharp interfaces from the improved growth architecture.

Improving the base layer morphology and eliminating the V-pits improves the electrical performance of μLEDs fabricated from these base layers by causing a significant reduction in leakage current. Since pits originate in the substrate, they can propagate through the entire device structure beginning at the n-type base layer through the active region and into the p-type region. While n-type and intrinsic GaN and InGaN grow conformally to the {10-11} semipolar V-pit facets [80] at a reduced growth rate [117, 64], the p-type InGaN and GaN instead act as a "filling layer" for the V-pits and planarize the surface [63]. A lower polarization barrier also exists on the semipolar sidewall planes by definition, as the polarization is coaxial with the c-axis, resulting in only a component of the total polarization being present in the [10-11] direction. Since less resulting polarization exists at the pit sidewall, the polarization barrier present at each interface is lowered, allowing superior charge flow at the pit [7, 78]. After the p-type material is grown, V-pits present in the epi result in an electrical path bypassing the active region. The exact mechanism for charge transfer or nonradiative recombination in the V-pit is currently under investigation.

I have examined the growth conditions for growth of thick InGaN/GaN:Si base layer structures on semi-relaxed substrates, significantly improving growth morphology and enabling fabrication of initial μLEDs. With a periodic interlayer structure of InGaN with HT-GaN interlayers, a method to significantly improve the crystal quality of the base layer is developed. With this growth method, V-pits present before the active region beginning in the substrate are eliminated and other crystal defects are significantly reduced alongside lower interface roughness. The morphological improvement of the base layer growth leads to a significant improvement to fabricated μLEDs operated under forward bias, reducing both leakage current and dynamic resistance, naturally improving device performance. The LEDs on higher quality, pit-free base layers possess much lower forward leakage current and dynamic resistance than their counterparts on pitted base layers, owing to the reduction in available leakage pathways and resulting improvement to crystal quality.

6.2 Extending to Long Wavelengths

For realizing μLEDs with emission extending to longer wavelengths, base layers and LEDs were grown by MOCVD at atmospheric pressure on the InGaNOS substrates. The Si concentration for the n-type InGaN/GaN:Si base layer doping is nominally 5x10^{18} cm^{-3}. A Mg concentration of 1.5x10^{20} cm^{-3} is employed for the p-type InGaN/GaN:Mg region doping. Multiple LEDs are investigated, each with different emission wavelength, on the same base layers. Base layers were grown at a temperature of nominally 950°C for the InGaN regions and 1050°C for the GaN interlayers. This InGaN/GaN base layer is the n-contact layer for the subsequently grown LED device. Once base layers were grown, active regions (ARs) consisting of 5 periods of 2.8 nm thick InGaN QWs, 2 nm AlGaN cap layers with 10% Al content, and 10 nm GaN QBs consisting of a 4 nm lower temperature (LT) portion and 6 nm higher temperature (HT) portion are regrown. Details on the active region

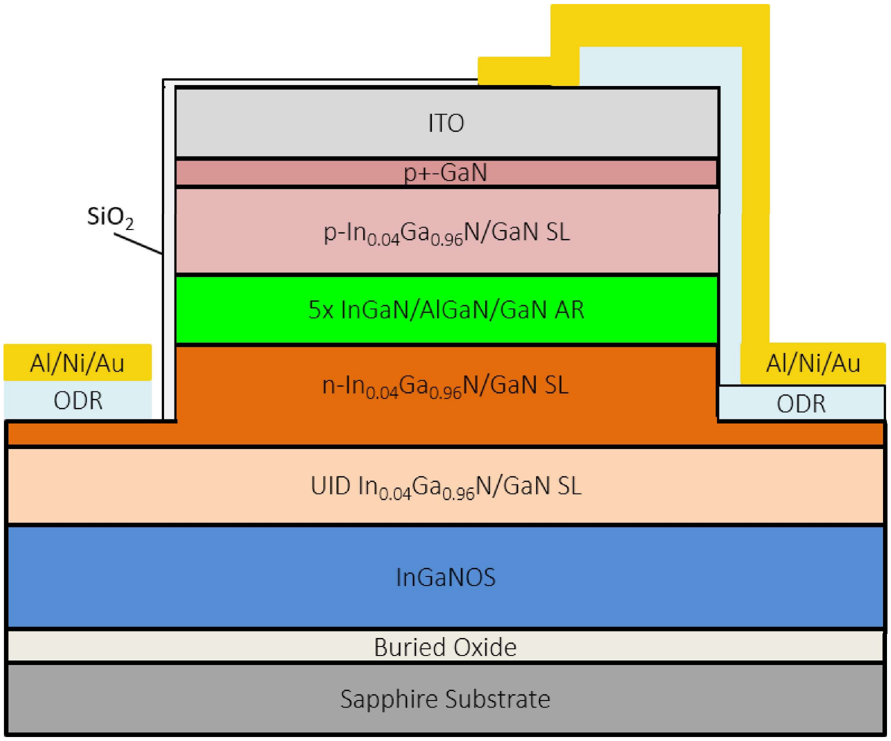

Figure 6.3: Cross-sectional schematic of finished fabricated device with epilayer sections labelled.

structure can be found elsewhere [118]. The p-contact layer for both structures consisted of a 5 period Mg-doped InGaN/GaN (20 nm InGaN and 2 nm GaN interlayers) structure with a nominal thickness of 110 nm grown isothermally.

To realize working LED devices with appreciable electroluminescence emission and operation lifetime, low defect density must be present in the epitaxy, especially when considering large defects such as V-defects or metallic In inclusions. Since the semi-relaxed InGaN substrates used here have a high density of V-defects, material quality must be significantly improved during the epitaxy to realize robust LED devices. In previous work, fully eliminating the V-defects in the InGaN base layers originating in the substrates through periodically growing high temperature (HT) GaN interlayers under partial H_2 carrier gas injection in the InGaN base layer is reported, leading to significant structural improvement [115]. This improvement can also be noted in fig. 6.4 which clearly shows the full elimination of V-defects on the optimized base layer. The improved epitaxy methods and the elimination of V-defects allows the benefits of the relaxed substrate to be leveraged into LED devices. Notably, the electrical and optical characteristics of the devices significantly improved when V-defects were eliminated, allowing a variety of EL emission wavelengths to be demonstrated.

Electrical characteristics were compared between LEDs grown on early development, V-defect base layers and optimized base layers free from V-defects through their current density-voltage (JV) behavior. fig. 6.5 compares two devices to examine their electrical behavior relative to each other. These devices only differ in the growth of the base layer, where the active region and p-type layers are otherwise equivalent. For both samples, the leakage current density at a forward voltage of 2.0 V can be compared, as it is below the turn-on voltage and large enough to generate measurable forward leakage current for both samples. It is clear that even at a low forward bias of 2 V significant current density measuring in the tens of A/cm^2 is achieved in the μLED device with the V-defect layer. Specifically, the μLED device fabricated with the high V-defect density base layer yields a leakage current density of 13.3 A/cm^2 while the device fabricated with the optimized base layer yields 0.629 A/cm^2 at 2.0 V of forward bias. The μLED device with the optimized base layer displays JV behavior more typical of an LED. The optimized base layer sample has a much lower forward leakage current and well defined turn-on with a linear region in the current density-voltage

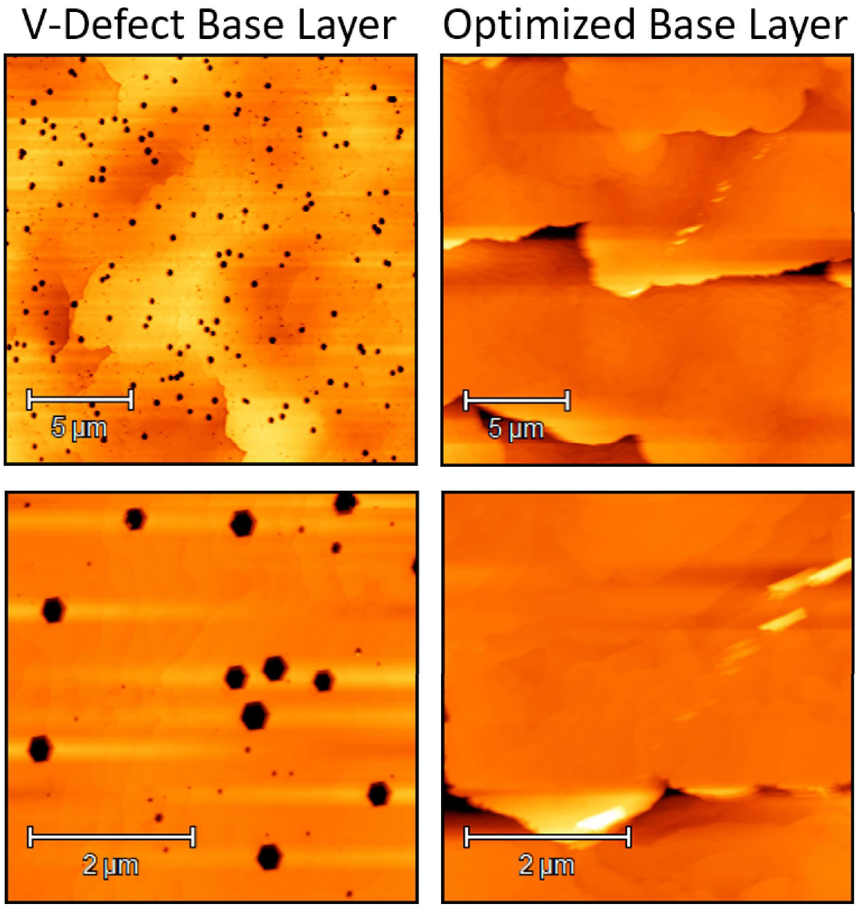

Figure 6.4: (Top) 20x20 μm and (bottom) 5x5 μm AFM scans for base layers containing V-defects and for optimized base layers.

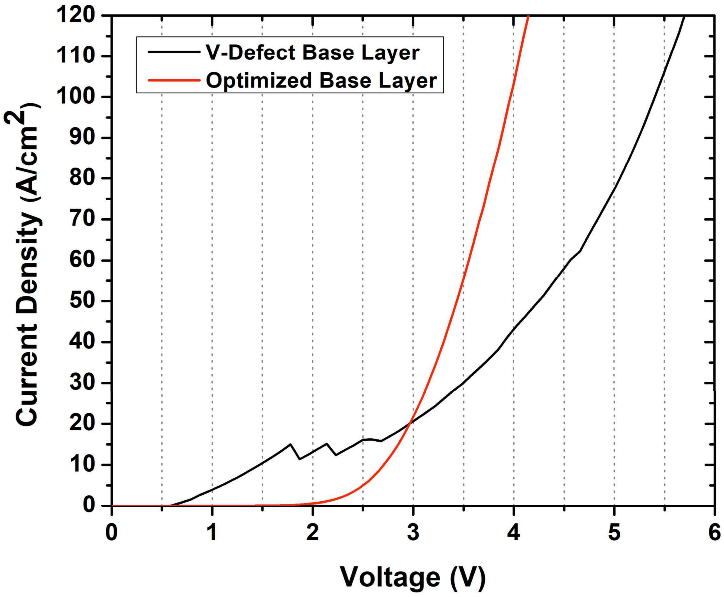

Figure 6.5: Current density-voltage behavior for selected 80x80 μ m^2 devices indicating improvement with base layer optimization.

response.

The electroluminescence emission spectra of μLED devices fabricated from the two types of base layers examined here, V-defect and optimized, were also compared. fig. 6.6 contains the electroluminescence spectra of the same two devices present in fig. 6.5 in order to make a clear comparison between them. The peak wavelength of the μLEDs grown on V-defect base layer and optimized base layers are nearly identical, 549 and 551 nm respectively, making the comparison between the samples reasonable. Under identical injection conditions of 35 A/cm^2, identical device size of 80x80 μm^2, and identical measurement setup, the μLED fabricated from the optimized base layer causes the absolute EL intensity to increase by more than an order of magnitude with a much more well-defined Gaussian

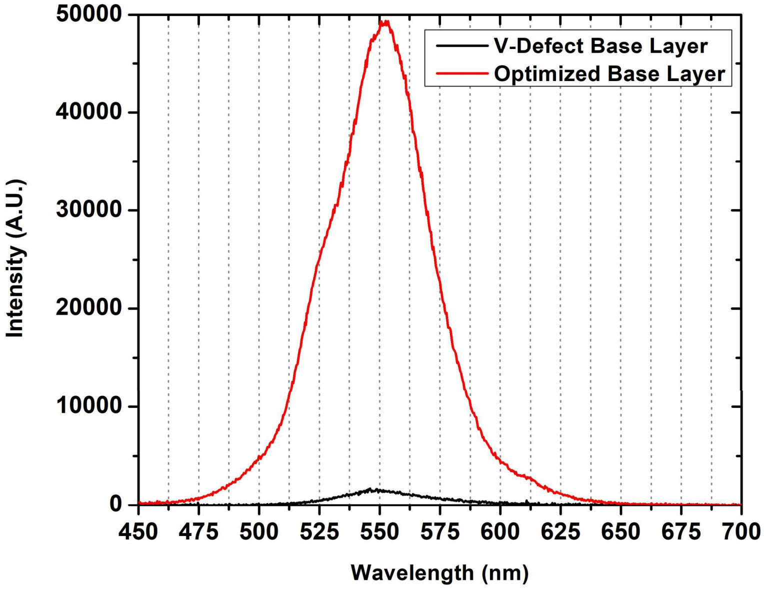

Figure 6.6: Electroluminescence spectra generated from two devices of nearly identical wavelength, one on a V-defect base layer and the other on an optimized base layer. Equal size devices were used (80x80 μm^2) at equal current density injection of 35 A/cm^2 for equivalent comparison. Intensity increases by approximately a factor of 30.

peak. The FWHM of the V-defect base layer and optimized base layer μLEDs' emission peak is 41 nm and 49 nm, respectively. A small shoulder can be noted in the spectra for the device with the optimized base layer which is attributed to In fluctuation in the QW at this long wavelength emission.

Beyond significantly improving to the electrical characteristics and performance of μLED devices at a given wavelength, the optimized base layer design enables the realization of a broad range of emission wavelengths, from cyan to deep red. The emission of the devices was generally controlled through QW growth temperature to achieve the desired emission wavelength. fig. 6.7 shows the normalized EL emission spectra of nine selected

μLED devices containing optimized base layers with peak emission wavelength ranging from 470 nm to 645 nm. These spectra were taken at equal current density, 20 A/cm^2, with the exception of the 470 nm emitting device taken at 30 A/cm^2 to achieve adequate light collection on an early LED sample. Generally, the full-width at half maximum (FWHM) of the emission peaks steadily increases with increasing wavelength emission. For devices with a peak emission at or below 580 nm, a single peak is observed with a relatively Gaussian shape. For devices with peak emission above 580 nm, multiple peaks can be seen in the emission as "shoulders" to the main peak or as closely grouped peaks that overlap. The broadening emission is attributed to likely microstructural inhomogeneity in the highest indium content samples. Similarly, the FWHM of the EL emission peak to increase with wavelength, from 23 nm for the 470 nm emitting device to 89 nm for the multi-peak 645 nm emitting device.

The significant improvement to μLED devices in terms of diode behavior, leakage current, and electroluminescence intensity can be attributed to the higher quality epitaxy, specifically from the elimination of V-defects in the base layer and resulting improvements to layer morphology. V-defects in the base layer must be managed to avoid propagation through the epitaxial structure to create large defect regions, or from forming leakage pathways. Since the majority V-defects originate in the substrate, these V-defects propagate through the entire device structure beginning at the n-type base layer through the active region and into the p-type region, widening as growth proceeds. Since V-defects form and widen from kinetically-limited growth, they can be filled at higher growth temperatures with different V/III ratios and carrier gasses such that there is sufficient mass transport to

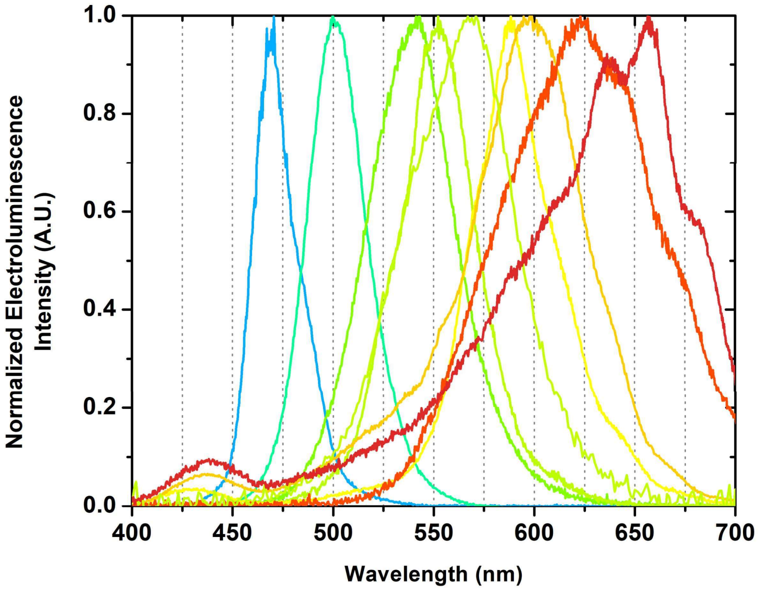

Figure 6.7: Normalized electroluminescence spectra from a large selection of grown and fabricated devices. All spectra were taken with 100 ms integration time and at 20 A/cm^2 with the exception of the 470 nm emitting device taken at 30 A/cm^2 to achieve adequate light collection.

the V-defect sidewalls (fig. 6.4). The V-defects in these devices are eliminated in the intrinsic and n-type regions when the lateral ingrowth growth of the defects becomes dominant over widening and propagation, consequently causing planarization of the growth surface. Eliminating the V-defects improves the electrical performance of μLEDs fabricated using these base layers by directly leading to a significant reduction in leakage current and improving diode behavior. In the same way, EL emission intensity of a μLED device with an optimized base layer also increases by over an order of magnitude- a factor of 30- at equivalent current density compared to a μLED device on a V-defect base layer (fig. 6.6).

A significant improvement to electrical performance can be attributed to the general improvement to crystal morphology by elimination of V-defects, optimizing growth conditions, and elimination of leakage paths. As shown in fig. 6.5, the leakage current density at voltages below the turn-on voltage measures in the tens of A/cm^2 for the device on the V-defect buffer as a result of a high V-defect density propagating from the substrate and its detrimental effect on morphology. Here, turn-on voltage is defined as the voltage where light can be detected initially, corresponding to when the JV response curve becomes superlinear beyond the leakage current regime. The high leakage currents demonstrated here below device turn-on recombine nonradiatively, quickly causing these devices to fail under operation through self-destruction of the metal contacts or open-circuit failure within the device. For these initial devices with poor morphology and unoptimized growth conditions, many of the devices on the processed sample would fail immediately beyond moderate voltages (in the 4-5 V range), or alternatively after a relatively short period continued operation on the order of seconds to minutes. Conversely, the optimized base layer free of V-defects yielded devices with much lower leakage currents, and improved diode behavior. These devices had a somewhat high series resistance represented by the inverse of the slope of the linear region in fig. 6.5, but it is greatly reduced compared to the μLED on the V-defect base layer. While some leakage current is naturally still present even in the V-defect-free μLED, this is attributed to other non-radiative recombination centers that arise from impurities or defects from crystal growth. Additionally, these devices were capable of operation at forward biases exceeding 7 V even after multiple testing cycles, as well as continuous operation on the order of hours without failure. The trend of a marked lifetime difference between devices grown on V-defect base layers and optimized base layers held true for all wavelength devices examined. The optimized base layer μLED device displays a lower operating voltage, lower series resistance, lower leakage current, and more robust lifetime and operation. In nearly all metrics, the electrical performance of μLED devices is improved.

In a similar vein, the optical characteristics of the device also significantly improve with optimization of the base layer. Electroluminescence spectra of identically sized μLED devices grown on the optimized base layer under identical current injection, measurement geometry, and integration time is presented in fig. 6.6, where the EL intensity of the μLED device on the optimized base layer increases by a factor of 30 compared to the V-defect base layer, indicating a marked increase in radiative efficiency of the device.

Additionally, these two devices have nearly identical emission wavelength, making the devices comparable. A small shoulder peak is visible in the peak from the optimized base layer μLED which is attributed to minor In fluctuation in the QW from the high In content required to achieve this long wavelength. This in turn also causes the FWHM to increase with increasing EL emission intensity, as seen in these samples. Generally, improvements in μLED devices resulting from an optimized base layer enable a wide variety of μLED devices to be realized with high brightness.

The emission wavelengths represented by the devices displayed in fig. 6.7 are remarkable for two reasons: first the range of wavelengths represented is quite wide, and second the emission range extends quite far into the long-wavelength visible regime compared to typical III-nitride devices. At a moderate operation current density of 20 A/cm^2, devices with a 175 nm range of peak wavelengths have been realized, covering most of the visible spectrum including the entire long-wavelength red area. Reduction of the compositional pulling effect by the semi-relaxed substrate and optimized base layer, as mentioned above, improved In incorporation in the QW. This development enables peak EL emission into the amber, red, and crimson regime. Devices with peak EL emission in the red regime, specifically at or above 600 nm, are typically extraordinarily difficult to realize with III-nitride materials due to the requirement of low temperature during QW growth for sufficient In incorporation [23, 29]. Realization of working devices with measurable emission is then inhibited as a result of increasing defect density, In segregation, and poor growth morphology [119]. In contrast, here higher growth temperatures can be employed due to the higher In incorporation in the QW enabled by the semi-relaxed substrates and reduction of the compositional pulling effect. This same effect enables the use of higher QW growth temperatures while maintaining the same emission wavelength.

As peak emission wavelength becomes longer, the FWHM widens as expected from increasing In fluctuation. Additionally, a small peak around 425 nm becomes more intense at longer wavelengths. This peak is attributed to charge injection through the low density of V-defects commonly generated in the lower QWs [59] into the V-defect-free n-InGaN buffer region where they recombine. The V-defects allow charge transport through the sidewall where the polarization barrier is reduced and the path conductivity is increased [62, 78]. At very long wavelengths, larger In fluctuations can be seen as small shoulders in the 620 nm emission μLED and as a close cluster of multiple peaks in the 645 nm emission μLED. At the longest visible wavelengths, some In phase separation in the QW becomes difficult to avoid. These issues arising from high-In QW growth- namely extended defect generation, In segregation, and related effects such as V-defect sidewall injection leakage- must be mitigated through optimization of the growth conditions in the QW and QW capping layers. Since defect generation is predominately in the form of V-pits, a similar growth approach to that used in the V-defect-free base layer could be applied to the QW. These growth conditions would suppress V-defect nucleation and close any V-defects that happen to form, as previously seen in the predominately InGaN base layer. At the same time, the leakage current from the V-defect sidewall into the base layer causing undesired short-wavelength emission would be eliminated. For suppression of In segregation, further development of the AlGaN capping layer to prevent In desorption during growth and thermal protection during later high temperature layer growth is necessary for a more homogeneous alloy layer. Since low growth temperatures must be used for increasingly higher In QW growth, but the GaN QB growth remains at the same temperature, the temperature difference between the two layers increases with increasing In content. The role of the QW capping layer then becomes even more crucial with longer wavelength LEDs requiring higher QW In contents.

Development of both of these aspects of μLED devices has already begun. Despite these difficulties, current realization of a III-nitride device emitting such long wavelengths with appreciable electroluminescence emission at a moderate current density has been achieved using these semi-relaxed substrates and optimized base layers, a feat not typically achieved with conventional GaN-on-sapphire growth.

I examined the application of V-defect free buffer layers on semi-relaxed InGaN substrates to growth and fabrication of III-Nitride LEDs with a wide range of emission wavelengths. The V-defect elimination directly leads to a significant reduction in leakage current in fabricated μLEDs operated under forward bias, which naturally improves device performance and diode-like characteristics. This material quality benefit also significantly increases the electroluminescence intensity of the light emission for otherwise equivalent devices. The resulting improvement to crystal quality in the base layers enables a very broad range of electroluminescence emission wavelengths from LEDs that employ them. This development presents significant progress toward highly efficient long-wavelength c-plane LEDs grown on relaxed substrates, a major step toward the ultimate goal of RGB devices on the same wafer using all III-Nitride devices.

6.3 p-Type Architecture and High Power Devices

In this work, high-performance μLEDs with red emission utilizing an InGaN base layer with thin GaN interlayers and optimized p-type InGaN/GaN superlattice structure grown on relaxed InGaN substrates are demonstrated, leading to improved light output power and EQE. Fabricated devices are analyzed in terms of their emission spectra, current density-voltage (JV) behavior, and their packaged device EQE results to determine improvements in light output power and efficiency, assuming a light extraction efficiency (LEE) of approximately 30% for a rudimentary surface-mounted and encapsulated package. Finally, atomic probe tomography (APT) is employed to measure the In content of the QW region, yielding some insight into the magnitude of the reduction of the compositional pulling effect and its effect on In incorporation. Compared to previous published devices, 609 nm red electroluminescence with a significant increase to the light output power are realized, achieving working μLED devices with an EQE approaching 1% at this long wavelength.

One drawback to the use of relaxed InGaN substrates is the poor crystal quality and rough morphology of the substrate InGaN layer that must be recovered with further growth. Specifically, the substrates used in this work contain a native V-defect density of 5x10^8 cm^{-2}, but generally the substrate defect density will be dependent on the starting InGaN material. Additionally, further growth must take strain management into account with respect to the increased lattice constant, as a pure GaN layer would undergo tensile stress under this growth condition and eventually crack with sufficient thickness. In our previous work, a base layer scheme consisting of a InGaN/GaN buffer/interlayer structure is developed, designed to fully eliminate the V-defects and achieve high crystal quality. These base layers employ optimized growth conditions for buffer and interlayer thicknesses, temperatures, V/III ratio, and carrier gasses [115]. This base layer was also designed to match the lattice constant of the substrate, maintaining the relaxed strain state present initially. With a base layer free from V-defects and with good morphology, the advantages of the relaxed

InGaN substrate and increased lattice constant can be used in the realization of μLED devices [120]. Importantly, the reduction of the compositional pulling effect resulting from the reduction in strain during growth can then be applied to QW growth, allowing for higher temperatures to be used while still achieving high In content in a red-emitting device.

To characterize the performance of the fabricated μLED devices, the basic electrical behavior of a representative device and its emission characteristics are first examined. The current density-voltage response is seen in fig. 6.8, along with a more specific look at the low current-density range near the turn-on region of the device. From fig. 6.8a, typical diode-like behavior can be clearly visualized across a wide voltage range. An optical image of the device under operation at a moderate current density of 20 A/cm^2 can also be seen in the inset image in fig. 6.8a. While the resistance of the LED may be somewhat high at a value of 2695 Ω at 20 A/cm^2 corresponding to 3.45 V, significant current density is accessible in the examined bias range. Furthermore, extremely low leakage current density can be seen, with only 2.81 mA at -5V bias. The turn-on voltage of the device (seen more clearly in fig. 6.8b) is 2.6V, determined from the regression of the linear region of the JV curve in the low-current-density regime shown in fig. 6.8b. Finally, the EL emission spectra for the device is shown in fig. 6.8c, indicating red emission at 609 nm at a current density injection of 7 A/cm^2 corresponding to 3.01 V. At this wavelength the EL emission spectra has a FWHM of 74 nm and a single peak, relatively broad but a broadness typical of long-wavelength LEDs [39]. This broad FWHM typically present in the red-emitting LEDs is a result of significant In fluctuation, which worsens as the In mole fraction in the QW increases [71, 72, 45]. These parameters were reproducible throughout multiple operation cycles and after continuous

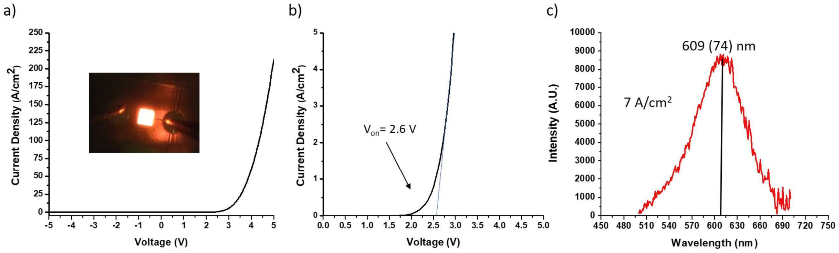

Figure 6.8: a) Current density-voltage (JV) behavior for fabricated device from -5V to 5V with inset optical image of device electroluminescence at 20 A/cm^2. b) The same JV curve focused on low-current-density regime; turn-on voltage indicated. c) Electroluminescence (EL) emission spectra of device operating at 7 A/cm^2 with peak wavelength and FWHM identified.

high-current operation. Here, red emission is achievable and detectable even at low current density injection of 7 A/cm^2 near the LED turn-on and emits a clearly visible EL peak.

Selected on-chip devices were encapsulated into device packages to ascertain the power and efficiency of a finished, packaged device module in an integrating sphere. The light output power steadily increases with current density injection for a representative device, steadily becoming more sublinear (fig. 6.9b) with increasing current density. This lower power is due to both a small heating effect under continuous operation as well as the increasing effect of Auger recombination at increasing current density. Rather than a steady increase mimicking the shape of the power curve, the EQE curve takes on a "droop" shape typical of nitride LEDs. A peak EQE value is typically reached at low to moderate current densities, followed by a steady decline in EQE as current density is increased. The peak EQE of the device is 0.83%, occurring at a wavelength of 609 nm and a current density value of 7 A/cm^2 corresponding to 3.01 V. Despite the strain reduction benefits of the relaxed substrate with enlarged lattice constant, the remaining strain still present in the QW

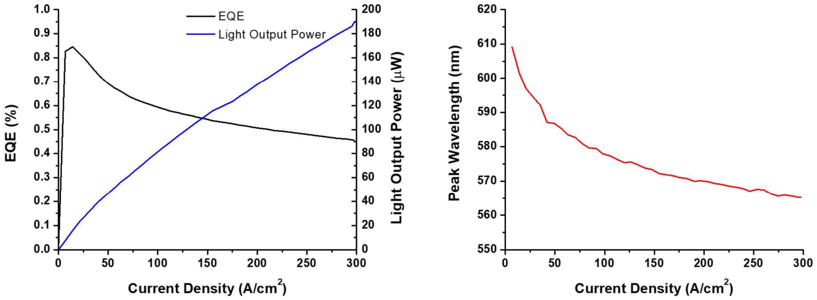

Figure 6.9: Plots of EQE and peak wavelength for selected representative 80x80 μm^2 device.

results in unresolved piezoelectric fields, leading to the QCSE, higher Auger recombination, and ultimately leading to EQE droop. However, red emission from a μLED device with EQE approaching 1% shows that the optimized growth methods for the device epilayers show improved device performance.

To further characterize the active region of these devices and confirm the true In content present when grown on relaxed substrates, APT was performed on the LED sample. The reconstruction of the APT tip sample is shown in fig. 6.10a, where the active region can be seen as alternating layers of high-In InGaN QWs, AlGaN capping layers, and GaN QBs. Furthermore, the lower buffer regions can be seen as having a defined layer structure of InGaN regions and thin GaN interlayers. fig. 6.10b then further characterizes these regions, with the group-III content plotted for Ga, In, and Al corresponding to the sample reconstruction. Since the purpose of the GaN interlayer is to prevent the transition to a 3D growth mode by eliminating the surface riding In that increases as growth proceeds, some slight In nonuniformity in each individual InGaN layer can be seen surrounding these GaN interlayers. Both the quantitative atomic composition profile and spatial reconstruction are

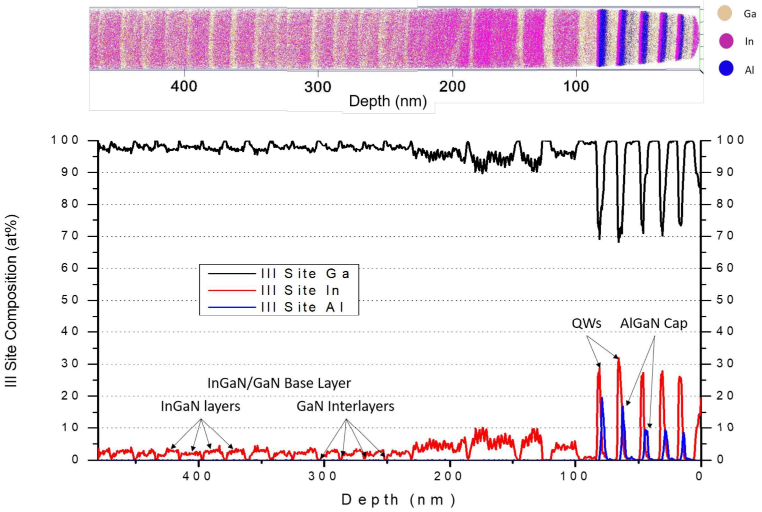

Figure 6.10: a) Reconstruction of the analyzed APT tip for III-site atoms. b) Corresponding group III composition profile of the sample in atomic percentage.

in agreement, especially visible in the nominally pure GaN regions, i.e. the thin interlayers in the base layer region below the QWs, and GaN QBs. In the QWs, an In content of up to 32% can be seen even with the high QW growth temperature (810°C) used during growth. Despite each QW having nominally identical growth conditions, their In contents fluctuate slightly. However, the AlGaN capping layers unexpectedly have Al content of either approximately 10% or 20% despite also having identical growth conditions. Capping layers were expected to contain 10% Al, and the reason for the discrepancy in Al content of the capping layers of first two QWs is currently under investigation. It should also be noted that the two higher-Al capping layers also reside above the two higher-In QWs, QW1 and QW2 at 28.8% and 32.0% In, respectively while QWs 3, 4, and 5 have a measured In content of 26.2%, 26.9%, and 26.3%, respectively, with 10% Al capping layers.

The design of the epitaxial growth scheme (fig. 6.11a) enables these high-efficiency red μLEDs through the use of an optimized base layer to preserve material quality before growth of the active region, high temperatures during QW growth, and optimized p-type superlattice. The InGaN/GaN base layer design allows for elimination of V-defects prior to the active region, and significantly improves the crystal quality of the almost entire InGaN-based device despite the increased difficulty when growing an InGaN alloy [115]. Additionally, this base layer design allows the benefit of the substrate's enlarged lattice constant to be leveraged in the active region to reduce the compositional pulling effect, increasing the In incorporation efficiency as the effective strain at the growth interface decreases. As a result of reducing the compositional pulling effect, the In incorporation during QW growth is significantly increased, enabling high In content up to 32% (fig. 6.10) resulting in red emission from the QW. Additionally, the significantly improved In incorporation from strain management allows the use of increased temperatures during QW growth while achieving the same In content. In this case 810°C can be used to achieve an In content that results in red emission, much higher than typical QW growth temperatures used for conventionally grown red-emitting μLEDs [29]. Notably, the 810°C QW growth temperature used here for a red-emitting LED on InGaNOS is more typical of a green-emitting LED grown on conventional sapphire in the same reactor. Finally, the p-type design also employs an InGaN/GaN structure similar to that of the base layer, but in this case with thinner InGaN periods than previously fabricated LEDs for improved crystal quality due to less ternary alloy growth and higher power. With these aspects of epitaxial growth design all optimized, the overall growth scheme is tailored for high-In InGaN growth and superior device performance.

Devices fabricated from samples using this epitaxial design yield state of the art

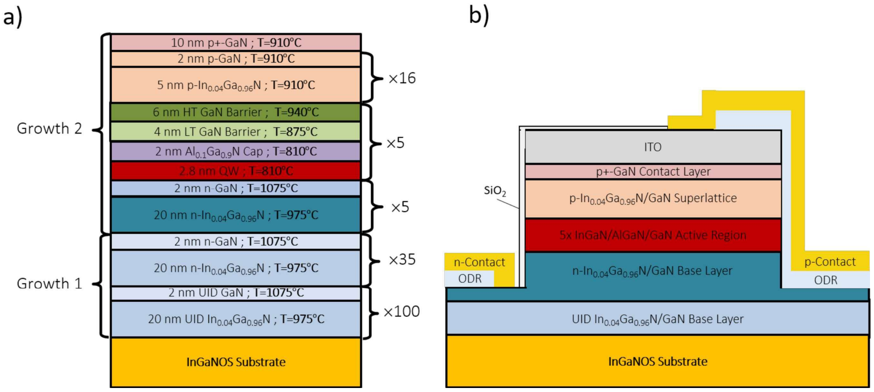

Figure 6.11: a) Epitaxial structure of the as-grown LEDs with labelled growth parameters and periodicity. b) Corresponding fabricated device structure.

electrical and optical emission characteristics for red-emitting InGaN μLEDs grown on relaxed substrates. The turn-on voltage determined from the JV plot in fig. 6.8a and 6.8b is quite low at a value of 2.6 V. This turn-on voltage is especially low considering the photon voltage of 2.03 eV for 609 nm emission, indicating little barrier to carrier transport. This is further supported by the low voltage, 3.45 V, present at an injection current density of 20 A/cm^2. Even considering the relatively high dynamic resistance of the device under operation, the low turn-on and operational voltages indicate good charge transport to the QW even at a bias similar to the expected band gap energy. Additionally, the EL emission spectrum at 7 A/cm^2 shows a clear peak at 609 nm, a red-emitting device. At such long peak wavelengths, the FWHM of the emission spectra is also quite high at 74 nm. High FWHM is to be expected at long wavelengths, as the alloy fluctuation naturally present during the growth of InGaN becomes more extreme with increasing In content [121, 70].

Most strikingly, devices yielded improved power and efficiency at long wavelengths. From integrating sphere measurements of optoelectrical device performance (fig. 6.9a), typical devices possess an EQE of 0.83%, higher than other reported red-emitting III-N devices beyond simple proof of concept devices [41, 122]. Notably, this EQE value is achieved even with only basic packaging with unoptimized LEE. High EQE has been reported on some red devices employing relaxation via V-defects, [21] but only with large-area devices grown on Si substrates rather than μLEDs on sapphire like those reported here. The high efficiency of the device while maintaining long-wavelength red emission represents a record performance for III-N devices grown on relaxed substrates. In short, the characteristic droop shape confirms the defect density of the device is sufficiently low, allowing a high enough carrier density to be achieved in the QW to display Auger-dominated recombination. Similarly, the power increases nearly linearly with current density injection, with some roll-off present in the droop regime. Examining the output across the same current density range, the emission wavelength becomes shorter with increasing current density, resulting in an expected "blueshift" to the emission due to screening of polarization-related electric fields. This example of blueshift yields 40 nm of peak wavelength shift over 300 A/cm^2, with about 20 nm of shift between 0 and 50 A/cm^2. Though this blueshift occurs throughout the measurement range examined, the small shift over the typical operation range (often targeted to be less than 10 A/cm^2 for μLEDs) indicates good control over the strain and resulting net electric field that causes carrier screening. Ultimately, the measured high efficiency value, typical power and efficiency behavior, and well-managed characteristic blueshift indicate high-performance devices for red-emitting μLEDs.

Finally, the true sample structure can be seen in the APT reconstruction of the sample in fig. 6.10a. The base layer InGaN/GaN scheme can be clearly viewed from this reconstruction, as can the active region structure, indicating good layer structure present throughout the growth. Benefits of the increased substrate lattice constant and resulting reduction in the compositional pulling effect can be directly seen through APT measurement and reconstruction, where the high-In content of the QW is confirmed. Despite the high growth temperature of the QW for red emission, an average QW In content of 28.1% was measured along with a maximum QW In content of 32.0%, consistent with the red emission. Unexpectedly, the Al content present in the capping layer of QW1 and QW2 is elevated to approximately 20% despite possessing the same growth conditions. Each QW in the active region possessed identical growth conditions, where the capping layers are calibrated to 10%. Interestingly, higher In contents were seen in the wells corresponding to the highest Al capping layers, suggesting that the capping layer may play an important role in further retention of In in the QW. It is hypothesized that the higher Al content capping layer allows for increased thermal protection of the high-In QW during later high temperature growth of the QB and p-type region. With the QW better thermally protected, less In desorption occurs as a result of thermal degradation. Typically, the temperature used here during QW growth would result in much lower In content, more similar to the content of a green-emitting LED. Especially when considering the growth temperature, this APT measurement conclusively confirms the improved In incorporation in the QW through strain management from an increased lattice constant.

6.4 Active Region Development and Fatal Substrate Flaw

With the success of realizing working long-wavelength μLEDs with high brightness by altering the p-type region, attention was turned to characterization and improvement of the active region. Here, each layer in the device is identified and optical and electrical behavior of the active region of our devices is characterized, including a measurement of the IQE. A standard room-temp PL measurement is performed to estimate the emission wavelength of the device optically pumped, and μLEDs are processed to measure the EL at a desired current injection (fig. 6.12). Each InGaN-containing region can be identified by its room-temperature PL emission wavelength, as the wavelength can be approximated by the In contents expected for each region. Similarly, the EL measurements yields the emission wavelength with carrier transport effects included, here measured at a specific current density injection, as it comes from a sample fully processed into a device. These samples were grown identically, so the PL and EL measurements are characterizing identical devices as as-grown material as well as fully fabricated and processed devices.

With the PL emission peaks identified at room temperature for as-grown samples, low-temperature PL (LT-PL) was used to estimate the radiative efficiency of the active region, typically used as an analog for IQE of the emitting QW active region. By taking a baseline-corrected PL spectra at each point in a laser power sweep, the spectra can then be integrated across a wavelength range known to contain the QW emission peak to yield an integrated intensity curve. This method is repeated for each laser power point, and at multiple temperatures between room temperature and cryogenic conditions (fig. 6.13). This integrated

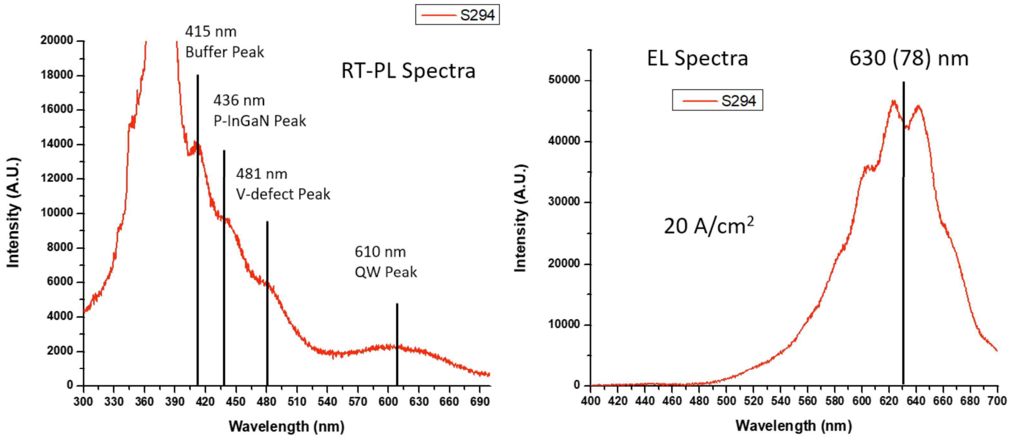

Figure 6.12: (left) RT-PL of best device growth with each peak position identified and layer identity shown in the spectrum. (right) EL spectra of this same growth sample processed into a device.

intensity curve can then be normalized to the highest laser power at cryogenic condition, in this case 14K. In order to estimate the IQE, the assumption that no nonradiative emission will occur at cryogenic conditions due to the lack of available phonons is used. As a result, it is assumed that the normalization point will possess 100% radiative efficiency/IQE. While this assumption holds less true as the cryogenic temperature used rises, the measurement nonetheless still offers a reasonably close approximation of the IQE. Using this method, our measurements indicate the active region of our red-emitting devices possesses 23% IQE. This metric is especially relevant as many other research groups use a similar measurement procedure, allowing fair IQE comparisons between devices from different research groups and approaches and yielding finer, measurable insight to the significant improvement to our devices.

Unfortunately, further experiments began to yield worse results in all metrics, with

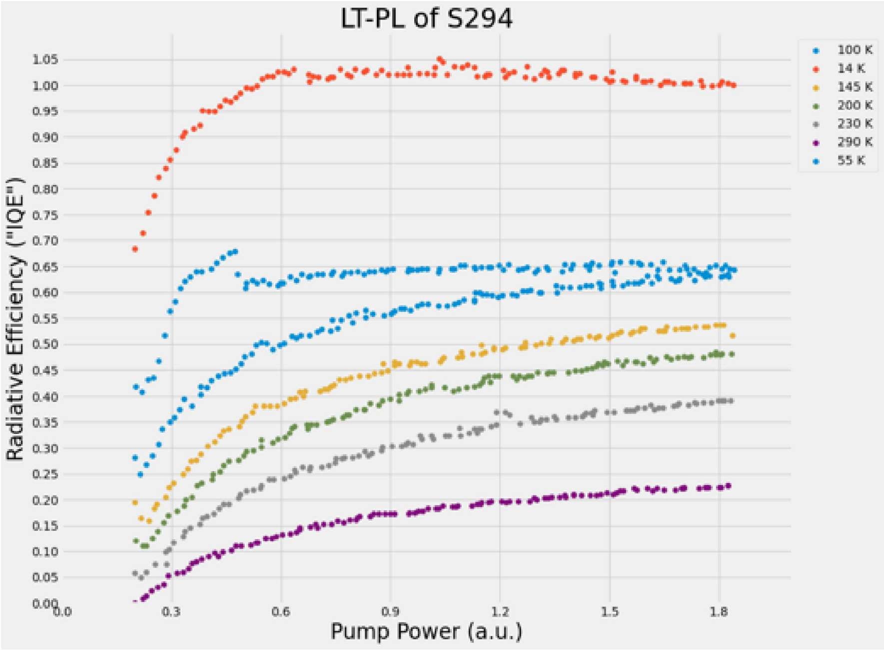

Figure 6.13: LT-PL radiative efficiency measured across all laser powers at all temperatures to estimate the IQE. Only the QW emission peak is integrated. Radiative efficiency normalized to lowest temperature and highest laser power point.

the device performances and crystal morphology previously achieved being unrecoverable. Even when attempting to reproduce the previous samples that yielded high performance at long wavelengths, these performances could no longer be achieved in working devices. To troubleshoot this issue, our buffer layers are more heavily characterized, which had not been altered since they had been optimized for V-defect elimination. During this investigation, it was found the buffers had significantly lower crystal quality, measured through x-ray rocking curve. From rocking curve analysis, the FWHM of the peak had increased by 50%, indicating a sharp decrease to material quality from higher defect density. Since no change had been made to the growth conditions, attention was turned to the substrates for any changes, characterizing them in the same way. Using the same rocking curve analysis (fig. 6.14), it was determined the substrate quality was much worse than for the previously received substrate wafers. While previous substrates were received with a FWHM of approximately 2600 arcsec for the 002 reflection rocking curve, the current batch of substrates had a measured FWHM ranging from 4700 to 5800 arcsec, more than twice that of the previous substrates used to make high-performance devices.

This low substrate crystal quality, combined with the inability to recover this crystal quality in an efficient manner with the buffer layer growth, precludes any significant further research progress. Previous buffer quality was not ideal at a FWHM of 600 arcsec in 002 reflection after growth, but would still allow for realization of bright μLED devices. In this case, buffer growth would have to be altered significantly to achieve the same crystal quality as previous buffers, likely requiring much thicker growths to recovery the morphology, and causing a number of issues with strain management. Additionally, additional substrates

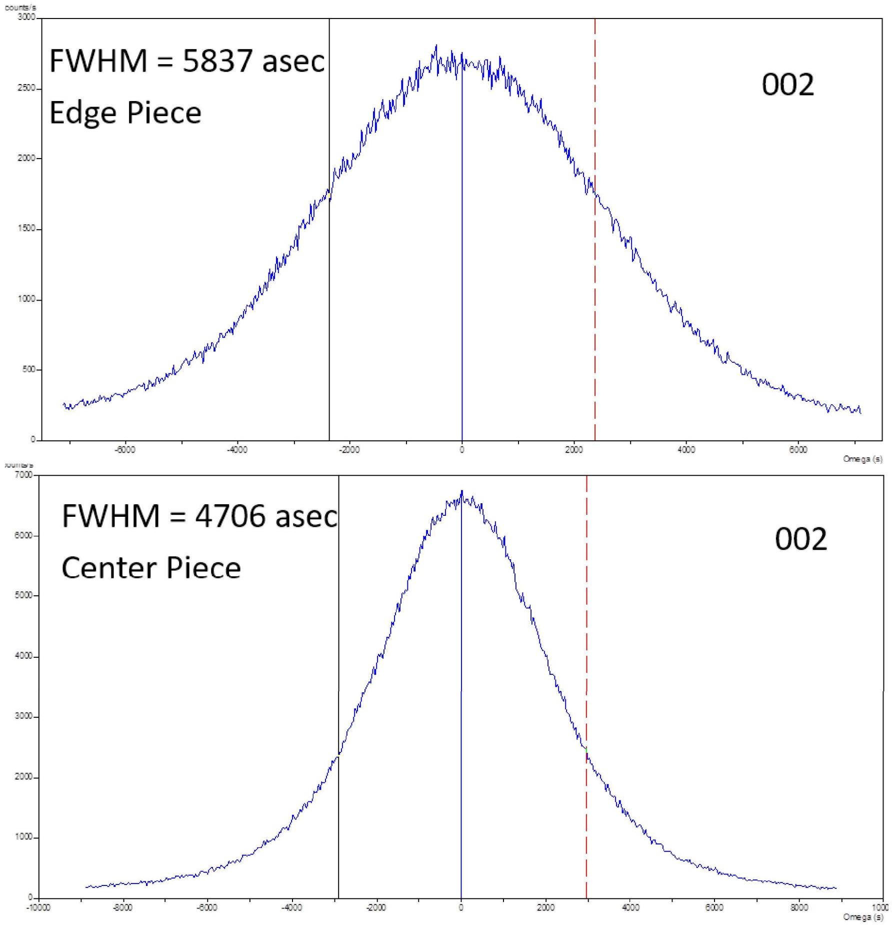

Figure 6.14: Rocking curve of 002 reflection for substrate pieces taken from the center and edge of the large substrate wafer. FWHM is noted

were no longer available, and the ability to produce more of original the substrates with reasonable crystal quality was no longer present. With only these lower quality substrates available, and their demonstrated inability to produce comparable working devices, the project was ended here. With no possible progress left, the partnership ended between UCSB and SOITEC that funded this project.

Chapter 7

Conclusions and Future Directions

In summary, bright red-emitting III-nitride μLED devices have been realized through employing a relaxed InGaN substrate and optimized p-layer design. Employing an InGaNOS substrate with increased lattice constant allows for increased In incorporation in the QW due to reducing the compositional pulling effect, resulting in 609 nm red emission possible at elevated QW growth temperatures. Combining this substrate with an InGaN/GaN base layer scheme for maintaining the relaxed lattice constant, defect reduction, and strain management, improved crystal morphology can also be achieved for the device. The average alloy content in the red-emitting QW is measured to be 28.1% In, with a maximum of 32.0%, yet the QWs were grown at elevated temperatures more typical of a shorter-wavelength LED. The improved p-type region design improves the crystal quality and morphology compared to previous designs, and in turn it is hypothesized that this improves the p-type charge transport in the region. Combined, these two improvements result in long-wavelength 80x80 μm^2 μLEDs emitting at 609 nm with an appreciable peak EQE of 0.83% at 7 A/cm^2 and

3.01 V. The developments presented here represent significant progress toward highly efficient long-wavelength c-plane III-nitride devices and a major step toward realization of RGB sources using all III-Nitride materials.

.1 Making Figures

Figures were made predominately using Origin 8 with standard saved formatting choices. These formatting choices included bold font, bold axes labels, 2pt line thicknesses, bold legend, size 18pt font, horizontal grid lines on major axes with dashed style and gray, translucent color. Other figures were created using Excel using the standard in-built tools for data visualization. For these figures, only horizontal grid lines were used, but the remaining style choices were unchanged.

.2 Measurement and Data Collection

Atomic Force Microscopy (AFM) was used to investigate the surface morphology after the growth of the InGaN base layers under different growth conditions. AFM measurements were performed using an Asylum MFP-3D system operating in tapping mode. X-Ray Diffraction (XRD) was used to determine crystal quality, In content, and thickness of epitaxially grown layers when possible. Composition of InGaN and thickness of the layers is determined using $\omega - 2\theta$ scans while crystal quality is determined by the FWHM of a (002) reflection measured in a rocking curve scan. These measurements were performed using an Panalytical MRD PRO Materials Research Diffractometer employing a 2.2 kW Philips ceramic sealed tube source with a wavelength of 1.5405 Å corresponding to Cu K_α transitions. Transmission electron microscopy (TEM) was employed using Focused Ion Beam (FIB) techniques to prepare samples. TEM imaging was used to investigate interface abruptness and structural features of buried layers. TEM imaging was carried out using ThermoFisher Talos 200X S/TEM, operated at 200 kV. FIB sample preparation was performed with a FEI Helios Dualbeam Nanolab 650. Atom probe tomography (APT) was performed to determine the In content of the QWs in these devices. Sample preparation was performed by coating the epi samples with 200 nm Ni metal, and a small section of the sample was removed using focused ion beam (FIB) with a FEI Helios Dualbeam Nanolab 650 to create an APT tip for analysis. APT measurements were then performed using an Imago LEAP 3000X HR Atom Probe Microscope. All optical emission measurements were collected using an optical fiber and OceanOptics spectrometer, and/or a calibrated silicon photodetector positioned vertically above the devices. Confocal microscope images were taken using a Leica SP8 Resonant Scanning Confocal Microscope.

.3 Processing Follower

.4 A Message to Future Grad Students

I think everybody has their own version of advice about how to be a better graduate student and find success, or how to manage your self-perception, or some "motivational" words for getting through it. I'll spare anybody who actually reads this. No matter who you are or what your journey has been, my message is the same: always be aware of the

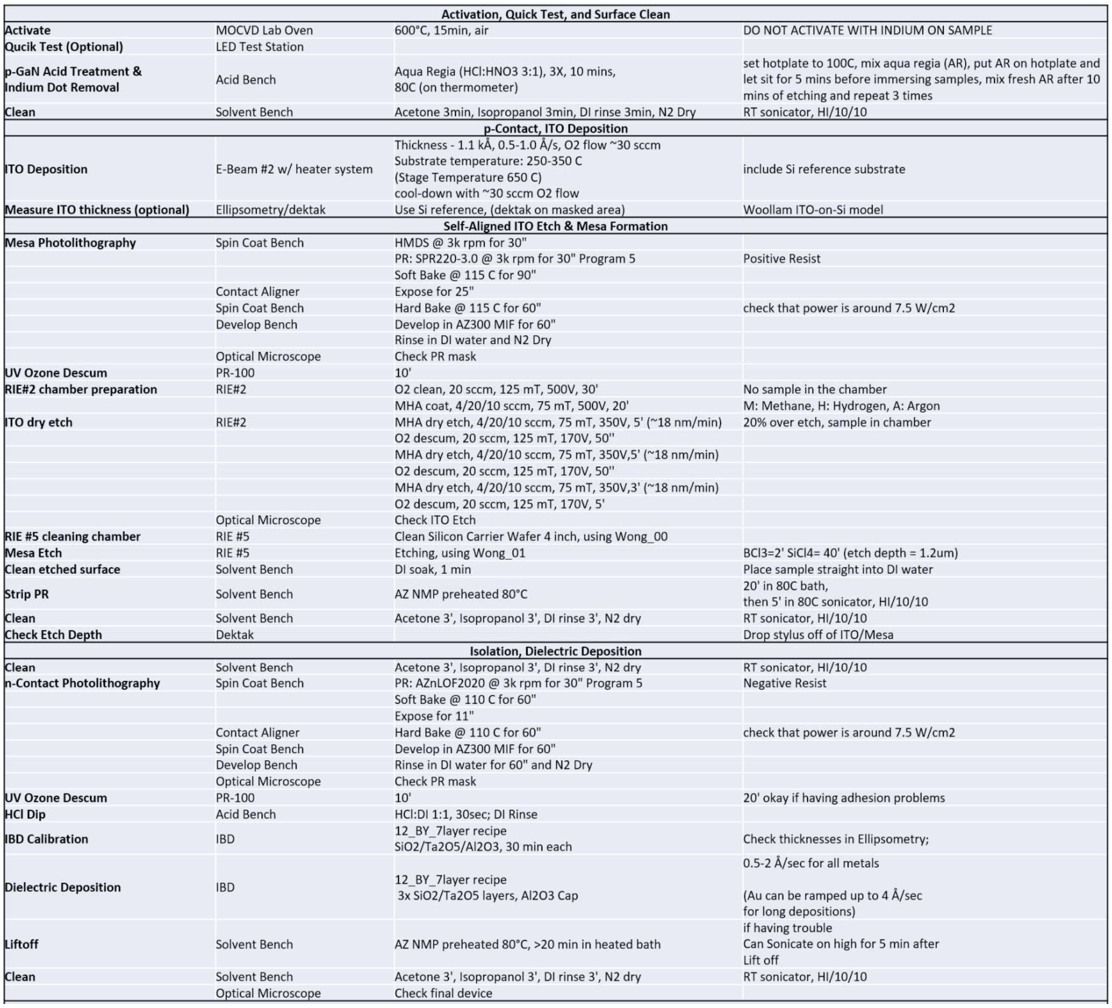

Activation, Quick Test, and Surface Clean			
Activate	MOCVD Lab Oven	600°C, 15min, air	DO NOT ACTIVATE WITH INDIUM ON SAMPLE
Qucik Test (Optional)	LED Test Station		
p-GaN Acid Treatment & Indium Dot Removal	Acid Bench	Aqua Regia (HCl:HNO3 3:1), 3X, 10 mins, 80C (on thermometer)	set hotplate to 100C, mix aqua regia (AR), put AR on hotplate and let sit for 5 mins before immersing samples, mix fresh AR after 10 mins of etching and repeat 3 times
Clean	Solvent Bench	Acetone 3min, Isopropanol 3min, DI rinse 3min, N2 Dry	RT sonicator, HI/10/10
p-Contact, ITO Deposition			
ITO Deposition	E-Beam #2 w/ heater system	Thickness - 1.1 kÅ, 0.5-1.0 Å/s, O2 flow ~30 sccm Substrate temperature: 250-350 C (Stage Temperature 650 C) cool-down with ~30 sccm O2 flow	include Si reference substrate
Measure ITO thickness (optional)	Ellipsometry/dektak	Use Si reference, (dektak on masked area)	Woollam ITO-on-Si model
Self-Aligned ITO Etch & Mesa Formation			
Mesa Photolithography	Spin Coat Bench	HMDS @ 3k rpm for 30"	
		PR: SPR220-3.0 @ 3k rpm for 30" Program 5	Positive Resist
		Soft Bake @ 115 C for 90"	
	Contact Aligner	Expose for 25"	
	Spin Coat Bench	Hard Bake @ 115 C for 60"	check that power is around 7.5 W/cm2
	Develop Bench	Develop in AZ300 MIF for 60"	
		Rinse in DI water and N2 Dry	
	Optical Microscope	Check PR mask	
UV Ozone Descum	PR-100	10'	
RIE#2 chamber preparation	RIE#2	O2 clean, 20 sccm, 125 mT, 500V, 30'	No sample in the chamber
		MHA coat, 4/20/10 sccm, 75 mT, 500V, 20'	M: Methane, H: Hydrogen, A: Argon
ITO dry etch	RIE#2	MHA dry etch, 4/20/10 sccm, 75 mT, 350V, 5' (~18 nm/min)	20% over etch, sample in chamber
		O2 descum, 20 sccm, 125 mT, 170V, 50''	
		MHA dry etch, 4/20/10 sccm, 75 mT, 350V,5' (~18 nm/min)	
		O2 descum, 20 sccm, 125 mT, 170V, 50''	
		MHA dry etch, 4/20/10 sccm, 75 mT, 350V,3' (~18 nm/min)	
		O2 descum, 20 sccm, 125 mT, 170V, 5'	
	Optical Microscope	Check ITO Etch	
RIE #5 cleaning chamber	RIE #5	Clean Silicon Carrier Wafer 4 inch, using Wong_00	
Mesa Etch	RIE #5	Etching, using Wong_01	BCl3=2' SiCl4= 40' (etch depth = 1.2um)
Clean etched surface	Solvent Bench	DI soak, 1 min	Place sample straight into DI water
Strip PR	Solvent Bench	AZ NMP preheated 80°C	20' in 80C bath, then 5' in 80C sonicator, HI/10/10
Clean	Solvent Bench	Acetone 3', Isopropanol 3', DI rinse 3', N2 dry	RT sonicator, HI/10/10
Check Etch Depth	Dektak		Drop stylus off of ITO/Mesa
Isolation, Dielectric Deposition			
Clean	Solvent Bench	Acetone 3', Isopropanol 3', DI rinse 3', N2 dry	RT sonicator, HI/10/10
n-Contact Photolithography	Spin Coat Bench	PR: AZnLOF2020 @ 3k rpm for 30" Program 5	Negative Resist
		Soft Bake @ 110 C for 60"	
		Expose for 11"	
	Contact Aligner	Hard Bake @ 110 C for 60"	check that power is around 7.5 W/cm2
	Spin Coat Bench	Develop in AZ300 MIF for 60"	
	Develop Bench	Rinse in DI water for 60" and N2 Dry	
	Optical Microscope	Check PR mask	
UV Ozone Descum	PR-100	10'	20' okay if having adhesion problems
HCl Dip	Acid Bench	HCl:DI 1:1, 30sec; DI Rinse	
IBD Calibration	IBD	12_BY_7layer recipe SiO2/Ta2O5/Al2O3, 30 min each	Check thicknesses in Ellipsometry;
Dielectric Deposition	IBD	12_BY_7layer recipe 3x SiO2/Ta2O5 layers, Al2O3 Cap	0.5-2 Å/sec for all metals (Au can be ramped up to 4 Å/sec for long depositions)
Liftoff	Solvent Bench	AZ NMP preheated 80°C, >20 min in heated bath	if having trouble Can Sonicate on high for 5 min after Lift off
Clean	Solvent Bench	Acetone 3', Isopropanol 3', DI rinse 3', N2 dry	RT sonicator, HI/10/10
	Optical Microscope	Check final device	

Sidewall Recovery; Dielectric Deposition			
Clean	Solvent Bench	Acetone 3', Isopropanol 3', DI rinse 3', N2 dry	RT sonicator, HI/10/10
Sidewall Deposition	ALD	TDMAS-150W/O*-300C recipe 500 cycles SiO2; Load spectator Si	Check thicknesses in Ellipsometry;
Clean	Solvent Bench	Acetone 3', Isopropanol 3', DI rinse 3', N2 dry	
p/n-Pads, Metal Deposition			
Clean	Solvent Bench	Acetone 3', Isopropanol 3', DI rinse 3'	RT sonicator, HI/10/10
p/n-Pad Metal Photolithography	Spin Coat Bench	PR: AZnLOF2020 @ 3k rpm for 30" Program 5	Negative Resist
		Soft Bake @ 110 C for 60"	
		Expose for 11"	
	Contact Aligner	Hard Bake @ 110 C for 60"	check that power is around 7.5 W/cm2
	Spin Coat Bench	Develop in AZ300 MIF for 60"	
	Develop Bench	Rinse in DI water for 60" and N2 Dry	
	Optical Microscope	Check PR mask	
UV Ozone Descum	PR-100	10'	20' okay if having adhesion problems
HF Dip	Acid Bench	BHF; 15 seconds	
p/n-Pad Metal Deposition	E-Beam #4	Al/Ni/Au, 5000/1000/5000Å	0.5-2 Å/sec, may use >5000Å if desired (may improve voltage when probing, and make it easier to wire-bond)
Liftoff	Solvent Bench	AZ NMP preheated 80°C, >20 min in heated bath,	if having trouble sonicate in heated bath on LO/0/0 NEVER ON HIGH!!
Clean	Solvent Bench	Acetone 3', Isopropanol 3', DI rinse 3', N2 dry	RT sonicator, LO/0/0 NEVER ON HIGH!!
	Optical Microscope	Check final device	
ITO Etch (p-CTLMs)			
ITO (CTLM) Photolithography	Spin Coat Bench	HMDS @ 3k rpm for 30"	
		PR: AZnLOF2020 @ 3k rpm for 30" Program 5	Negative Resist
		Soft Bake @ 110 C for 60"	
	Contact Aligner	Expose for 11"	
	Spin Coat Bench	Hard Bake @ 110 C for 60"	check that power is around 7.5 W/cm2
	Develop Bench	Develop in AZ300 MIF for 60"	
		Rinse in DI water and N2 Dry	
	Optical Microscope	Check PR mask	
UV Ozone Descum	PR-100	10'	
RIE#2 chamber preparation	RIE#2	O2 clean, 20 sccm, 125 mT, 500V, 30'	No sample in the chamber
		MHA coat, 4/20/10 sccm, 75 mT, 500V, 20'	M: Methane, H: Hydrogen, A: Argon
ITO dry etch	RIE#2	MHA dry etch, 4/20/10 sccm, 75 mT, 350V, 5' (~18 nm/min)	20% over etch
		O2 descum, 20 sccm, 125 mT, 170V, 50''	
		MHA dry etch, 4/20/10 sccm, 75 mT, 350V,5' (~18 nm/min)	
		O2 descum, 20 sccm, 125 mT, 170V, 50''	
		MHA dry etch, 4/20/10 sccm, 75 mT, 350V,3' (~18 nm/min)	
		O2 descum, 20 sccm, 125 mT, 170V, 5'	
	Optical Microscope	Check ITO Etch	
Strip PR	Solvent Bench	AZ NMP preheated 80°C	20' in 80C bath, then 5' in 80C sonicator, LO/0/0 NEVER ON HIGH!!
Clean	Solvent Bench	Acetone 3', Isopropanol 3', DI rinse 3', N2 dry	RT sonicator, LO/0/0 NEVER ON HIGH!!
Check Etch Depth	Dektak		Drop stylus off of ITO into CTLM gap

institutions you work with and work for. People love to pretend science, technology, and engineering are all inherently neutral, and they simply are not. Thinking these things are neutral is how people carelessly distance themselves from the effects of their work. It is not simply a small cast of bad actors "misusing" the technology we work to create. The technology we create has an intended use by an intended user, and either of these intentions can be horrific if looked at uncritically.

I ask anybody who works in our field to please strongly consider who and what your work will go toward, the impact of the technology, and who intends to own and use it. We have an ethical and moral responsibility to withhold our work and knowledge from projects and institutions that enable greater suffering regardless of their temptations. Plenty of defense contractors will offer you a great salary to help develop weapons to further global conflicts for profit, or tech companies to develop improved surveillance that will undoubtedly be turned against us, or logistics companies developing more efficient and exploitative ways to extract more labor from workers. Keep in mind how these institutions treat their employees and the functions they perform outside what you work on. Your support cannot be divided into only one part of an institution- the whole will benefit from your support. So don't.

List of Figures

List of Tables

Bibliography

[1] James M. Gee, Jeffrey Y. Tsao, and Jerry A. Simmons. Prospects for LED lighting. *Third International Conference on Solid State Lighting*, 5187(4):227, 2004.

[2] F. A. Ponce and D. P. Bour. Nitride-based semiconductors for blue and green light-emitting devices, 1997.

[3] Jonathan J. Wierer and Nelson Tansu. III-Nitride Micro-LEDs for Efficient Emissive Displays. *Laser and Photonics Reviews*, 13(9):1–15, 2019.

[4] Shuji Nakamura. The roles of structural imperfections in ingan-based blue light-emitting diodes and laser diodes. *Science*, 281(5379):956–961, 1998.

[5] H. Zhang, E. J. Miller, E. T. Yu, C. Poblenz, and J. S. Speck. Measurement of polarization charge and conduction-band offset at InxGa1xN/GaN heterojunction interfaces. *Applied Physics Letters*, 84(23):4644–4646, 2004.

[6] Ursula M.E. Christmas, A. D. Andreev, and D. A. Faux. Calculation of electric field and optical transitions in InGaN/GaN quantum wells. *Journal of Applied Physics*, 98(7), 2005.

[7] A. E. Romanov, T. J. Baker, S. Nakamura, and J. S. Speck. Strain-induced polarization in wurtzite III-nitride semipolar layers. *Journal of Applied Physics*, 100(2):1–10, 2006.

[8] N. G. Young, R. M. Farrell, S. Oh, M. Cantore, F. Wu, S. Nakamura, S. P. DenBaars, C. Weisbuch, and J. S. Speck. Polarization field screening in thick (0001) InGaN/GaN single quantum well light-emitting diodes. *Applied Physics Letters*, 108(6):1–6, 2016.

[9] Min Ho Kim, Martin F. Schubert, Qi Dai, Jong Kyu Kim, E. Fred Schubert, Joachim Piprek, and Yongjo Park. Origin of efficiency droop in GaN-based light-emitting diodes. *Applied Physics Letters*, 91(18):183507, 2007.

[10] T. L. Song, S. J. Chua, E. A. Fitzgerald, P. Chen, and S. Tripathy. Strain relaxation in graded InGaN/GaN epilayers grown on sapphire. *Applied Physics Letters*, 83(8):1545–1547, 2003.

[11] Shubhra S Pasayat, Chirag Gupta, Dillon Acker-James, Daniel A Cohen, Steven P DenBaars, Shuji Nakamura, Stacia Keller, Umesh K Mishra, et al. Fabrication of relaxed ingan pseudo-substrates composed of micron-sized pattern arrays with high fill factors using porous gan. *Semiconductor Science and Technology*, 34(11):115020, 2019.

[12] M. Hao, H. Ishikawa, T. Egawa, C. L. Shao, and T. Jimbo. Anomalous compositional pulling effect in InGaN/GaN multiple quantum wells. *Applied Physics Letters*, 82(26):4702–4704, 2003.

[13] S. Pereira, M. R. Correia, E. Pereira, K. P. O'Donnell, C. Trager-Cowan, F. Sweeney, and

E. Alves. Compositional pulling effects in (formula presented) layers: A combined depth-resolved cathodoluminescence and Rutherford backscattering/channeling study. *Physical Review B - Condensed Matter and Materials Physics*, 64(20):1–5, 2001.

[14] Yasutoshi Kawaguchi, Masaya Shimizu, Masahito Yamaguchi, Kazumasa Hiramatsu, Nobuhiko Sawaki, Wataru Taki, Hidetaka Tsuda, Noriyuki Kuwano, Kensuke Oki, Tsvetanka Zheleva, and Robert F. Davis. The formation of crystalline defects and crystal growth mechanism in InxGa1 - xN/GaN heterostructure grown by metalorganic vapor phase epitaxy. *Journal of Crystal Growth*, 189-190:24–28, 1998.

[15] A. Even, G. Laval, O. Ledoux, P. Ferret, D. Sotta, E. Guiot, F. Levy, I. C. Robin, and A. Dussaigne. Enhanced in incorporation in full InGaN heterostructure grown on relaxed InGaN pseudo-substrate. *Applied Physics Letters*, 110(26), 2017.

[16] D. Cooper, V. Boureau, A. Even, F. Barbier, and A. Dussaigne. Determination of the internal piezoelectric potentials and indium concentration in InGaN based quantum wells grown on relaxed InGaN pseudo-substrates by off-axis electron holography. *Nanotechnology*, 31(47), 2020.

[17] D. M. Van Den Broeck, D. Bharrat, Z. Liu, N. A. El-Masry, and S. M. Bedair. Growth and Characterization of High-Quality, Relaxed InyGa1yN Templates for Optoelectronic Applications. *Journal of Electronic Materials*, 44(11):4161–4166, 2015.

[18] J. Däubler, T. Passow, R. Aidam, K. Köhler, L. Kirste, M. Kunzer, and J. Wagner. Long

wavelength emitting GaInN quantum wells on metamorphic GaInN buffer layers with enlarged in-plane lattice parameter. *Applied Physics Letters*, 105(11), 2014.

[19] A Even, G Laval, O Ledoux, P Ferret, D Sotta, E Guiot, F Levy, IC Robin, and A Dussaigne. Enhanced in incorporation in full ingan heterostructure grown on relaxed ingan pseudo-substrate. *Applied Physics Letters*, 110(26):262103, 2017.

[20] Shinji Saito, Rei Hashimoto, Jongil Hwang, and Shinya Nunoue. InGaN light-emitting diodes on c-face sapphire substrates in green gap spectral range. *Applied Physics Express*, 6(11):111004, 2013.

[21] Fengyi Jiang, Jianli Zhang, Longquan Xu, Jie Ding, Guangxu Wang, Xiaoming Wu, Xiaolan Wang, Chunlan Mo, Zhijue Quan, Xing Guo, Changda Zheng, Shuan Pan, and Junlin Liu. Efficient ingan-based yellow-light-emitting diodes. *Photon. Res.*, 7(2):144–148, Feb 2019.

[22] Michel Khoury, Hongjian Li, Bastien Bonef, Tom Mates, Feng Wu, Panpan Li, Matthew S Wong, Haojun Zhang, Jie Song, Joown Choi, et al. 560 nm ingan micro-leds on low-defect-density and scalable (20-21) semipolar gan on patterned sapphire substrates. *Optics Express*, 28(12):18150–18159, 2020.

[23] I. Hsiu Ho and G. B. Stringfellow. Solid phase immiscibility in GaInN. *Applied Physics Letters*, 69(18):2701–2703, 1996.

[24] X. H. Wu, C. R. Elsass, A. Abare, M. MacK, S. Keller, P. M. Petroff, S. P. Denbaars, J. S. Speck, and S. J. Rosner. Structural origin of V-defects and correlation with

localized excitonic centers in InGaN/GaN multiple quantum wells. *Applied Physics Letters*, 72(6):692–694, 1998.

[25] Toshiki Hikosaka, Tomonari Shioda, Yoshiyuki Harada, Koichi Tachibana, Naoharu Sugiyama, and Shin ya Nunoue. Impact of InGaN growth conditions on structural stability under high temperature process in InGaN/GaN multiple quantum wells. *Physica Status Solidi (C) Current Topics in Solid State Physics*, 8(7-8):2016–2018, 2011.

[26] Yuh Renn Wu, Ravi Shivaraman, Kuang Chung Wang, and James S. Speck. Analyzing the physical properties of InGaN multiple quantum well light emitting diodes from nano scale structure. *Applied Physics Letters*, 101(8):083505, 2012.

[27] Rei Hashimoto, Jongil Hwang, Shinji Saito, and Shinya Nunoue. High-efficiency yellow light-emitting diodes grown on sapphire (0001) substrates. *Physica Status Solidi (C) Current Topics in Solid State Physics*, 11(3-4):628–631, 2014.

[28] M Takeguchi, MR McCartney, and David J Smith. Mapping in concentration, strain, and internal electric field in ingan/gan quantum well structure. *Applied Physics Letters*, 84(12):2103–2105, 2004.

[29] Jong Il Hwang, Rei Hashimoto, Shinji Saito, and Shinya Nunoue. Development of InGaN-based red LED grown on (0001) polar surface. *Applied Physics Express*, 7(7):1–4, 2014.

[30] Yongbing Zhao and Panpan Li. Toward Ultra-Low Efficiency Droop in C-Plane Polar

InGaN Light-Emitting Diodes by Reducing Carrier Density with a Wide InGaN Last Quantum Well. *Applied Sciences*, 9(3004), 2019.

[31] Yuge Huang, En Lin Hsiang, Ming Yang Deng, and Shin Tson Wu. Mini-LED, Micro-LED and OLED displays: present status and future perspectives. *Light: Science and Applications*, 9(1), 2020.

[32] Taeil Jung, Jung Hun Choi, Seung Ho Jang, and Seung Jun Han. Review of micro-light-emitting-diode technology for micro-display applications. *Digest of Technical Papers - SID International Symposium*, 50(Book 1):442–446, 2019.

[33] Matthew S. Wong, Shuji Nakamura, and Steven P. DenBaars. Review—Progress in High Performance III-Nitride Micro-Light-Emitting Diodes. *ECS Journal of Solid State Science and Technology*, 9(1):015012, 2020.

[34] Jacob Day, J. Li, D. Y.C. Lie, Charles Bradford, J. Y. Lin, and H. X. Jiang. III-Nitride full-scale high-resolution microdisplays. *Applied Physics Letters*, 99(3):1–4, 2011.

[35] Johannes Herrnsdorf, Jonathan J.D. McKendry, Shuailong Zhang, Enyuan Xie, Ricardo Ferreira, David Massoubre, Ahmad Mahmood Zuhdi, Robert K. Henderson, Ian Underwood, Scott Watson, Anthony E. Kelly, Erdan Gu, and Martin D. Dawson. Active-matrix GaN micro light-emitting diode display with unprecedented brightness. *IEEE Transactions on Electron Devices*, 62(6):1918–1925, 2015.

[36] Tingzhu Wu, Chin Wei Sher, Yue Lin, Chun Fu Lee, Shijie Liang, Yijun Lu, Sung Wen Huang Chen, Weijie Guo, Hao Chung Kuo, and Zhong Chen. Mini-LED and

Micro-LED: Promising candidates for the next generation display technology. *Applied Sciences (Switzerland)*, 8(9), 2018.

[37] Sung-Wen Huang Chen, Chih-Chiang Shen, Tingzhu Wu, Zhen-You Liao, Lee-Feng Chen, Jia-Rou Zhou, Chun-Fu Lee, Chih-Hao Lin, Chien-Chung Lin, Chin-Wei Sher, Po-Tsung Lee, An-Jye Tzou, Zhong Chen, and Hao-Chung Kuo. Full-color monolithic hybrid quantum dot nanoring micro light-emitting diodes with improved efficiency using atomic layer deposition and nonradiative resonant energy transfer. *Photonics Research*, 7(4):416, 2019.

[38] Ye Liu, Bo Wu, Yi-Chieh Wang, Ekembu K. Tanyi, and Li-Jing Cheng. Red emission carbon dots for microLED application. (September 2019):14, 2019.

[39] Y. Robin, S. Y. Bae, T. V. Shubina, M. Pristovsek, E. A. Evropeitsev, D. A. Kirilenko, V. Yu Davydov, A. N. Smirnov, A. A. Toropov, V. N. Jmerik, M. Kushimoto, S. Nitta, S. V. Ivanov, and H. Amano. Insight into the performance of multi-color InGaN/GaN nanorod light emitting diodes. *Scientific Reports*, 8(1):1–8, 2018.

[40] Zhe Zhuang, Daisuke Iida, and Kazuhiro Ohkawa. Effects of size on the electrical and optical properties of InGaN-based red light-emitting diodes. *Applied Physics Letters*, 116(17):173501, 2020.

[41] Daisuke Iida, Zhe Zhuang, Pavel Kirilenko, Martin Velazquez-Rizo, and Kazuhiro Ohkawa. High-color-rendering-index phosphor-free InGaN-based white light-

emitting diodes by carrier injection enhancement via V-pits. *Applied Physics Letters*, 117(17), 2020.

[42] Daisuke Iida, Zhe Zhuang, Pavel Kirilenko, Martin Velazquez-Rizo, Mohammed A. Najmi, and Kazuhiro Ohkawa. 633-nm InGaN-based red LEDs grown on thick underlying GaN layers with reduced in-plane residual stress. *Applied Physics Letters*, 116(16), 2020.

[43] Jeong-Tak Oh, Sang-Youl Lee, Yong-Tae Moon, Ji Hyung Moon, Sunwoo Park, Ki Yong Hong, Ki Young Song, Chanhyoung Oh, Jong-In Shim, Hwan-Hee Jeong, June-O Song, Hiroshi Amano, and Tae-Yeon Seong. Light output performance of red AlGaInP-based light emitting diodes with different chip geometries and structures. *Optics Express*, 26(9):11194, 2018.

[44] J. S. Speck and S. F. Chichibu. Nonpolar and Semipolar Group III Nitride-Based Materials. *MRS Bulletin*, 34(05):304–312, 2011.

[45] Hongjian Li, Michel Khoury, Bastien Bonef, Abdullah I. Alhassan, Asad J. Mughal, Ezzah Azimah, Muhammad E.A. Samsudin, Philippe De Mierry, Shuji Nakamura, James S. Speck, and Steven P. DenBaars. Efficient Semipolar (11-22) 550 nm Yellow/Green InGaN Light-Emitting Diodes on Low Defect Density (11-22) GaN/Sapphire Templates. *ACS Applied Materials and Interfaces*, 9(41):36417–36422, 2017.

[46] Blane Baker and Colby Lojka. Superbright Green InGaN Single-Quantum-Well- Structure Light-Emitting Diodes. *Jpn. J. Appl. Phys*, 34:1332–1335, 1995.

[47] Kazuhiro Ohkawa, Tomomasa Watanabe, Masanori Sakamoto, Akira Hirako, and Momoko Deura. 740-nm emission from InGaN-based LEDs on c-plane sapphire substrates by MOVPE. *Journal of Crystal Growth*, 343(1):13–16, 2012.

[48] X. A. Cao, J. M. Teetsov, M. P. D'Evelyn, D. W. Merfeld, and C. H. Van. Electrical characteristics of InGaN/GaN light-emitting diodes grown on GaN and sapphire substrates. *Applied Physics Letters*, 85(1):7–9, 2004.

[49] G. Parish, S. Keller, S. P. Denbaars, and U. K. Mishra. SIMS investigations into the effect of growth conditions on residual impurity and silicon incorporation in GaN and AlxGa1-xN. *Journal of Electronic Materials*, 29(1):15–20, 2000.

[50] David Holec, Yucheng Zhang, D. V.Sridhara Rao, Menno J. Kappers, Clifford McAleese, and Colin J. Humphreys. Equilibrium critical thickness for misfit dislocations in III-nitrides. *Journal of Applied Physics*, 104(12), 2008.

[51] Theeradetch Detchprohm, Kazumasa Hiramatsu, Kenji Itoh, and Isamu Akasaki. Relaxation process of the thermal strain in the gan /α-ai2o3 heterostructure and determination of the intrinsic lattice constants of gan free from the strain. *Japanese Journal of Applied Physics*, 31(10):L1454–L1456, 1992.

[52] X. H. Wu, C. R. Elsass, A. Abare, M. MacK, S. Keller, P. M. Petroff, S. P. Denbaars, J. S. Speck, and S. J. Rosner. Structural origin of V-defects and correlation with

localized excitonic centers in InGaN/GaN multiple quantum wells. *Applied Physics Letters*, 72(6):692–694, 1998.

[53] J. Elsner, R. Jones, P. K. Sitch, V. D. Porezag, M. Elstner, Th Frauenheim, M. I. Heggie, S. öberg, and P. R. Briddon. Theory of Threading Edge and Screw Dislocations in GaN. *Physical Review Letters*, 79(19):3672–3675, 1997.

[54] Lisa Sugiura. Dislocation motion in GaN light-emitting devices and its effect on device lifetime. *Journal of Applied Physics*, 81(4):1633–1638, 1997.

[55] Tomoya Sugahara, Maosheng Hao, Metalorganic Chemical, Vapor Deposition, Maosheng Hao, Tomoya Sugahara, Masashi Tsukihara, Yoshiki Naoi, Mingda Li, and Graphene-buffered Sapphire. Direct Evidence that Dislocations are Non- Radiative Recombination Centers in GaN. *Japanese Journal of Applied Physics*, 37:398–400, 1998.

[56] Tomoya S Ugahara, Maosheng H Ao, Tao W Ang, Daisuke N Akagawa, Yoshiki N Aoi, and Katsusi N Ishino. Role of Dislocation in InGaN Phase Separation. *Japanese Journal of Applied Physics*, 37(10):1195–1198, 1998.

[57] E. L. Piner, M. K. Behbehani, N. A. El-Masry, F. G. McIntosh, J. C. Roberts, K. S. Boutros, and S. M. Bedair. Effect of hydrogen on the indium incorporation in InGaN epitaxial films. *Applied Physics Letters*, 70(4):461–463, 1997.

[58] Nikhil Sharma, Paul Thomas, David Tricker, and Colin Humphreys. Chemical map-

ping and formation of v-defects in ingan multiple quantum wells. *Applied Physics Letters*, 77(9):1274–1276, 2000.

[59] K. Watanabe, J. R. Yang, S. Y. Huang, K. Inoke, J. T. Hsu, R. C. Tu, T. Yamazaki, N. Nakanishi, and M. Shiojiri. Formation and structure of inverted hexagonal pyramid defects in multiple quantum wells InGaN/GaN. *Applied Physics Letters*, 82(5):718–720, 2003.

[60] A. M. Sánchez, M. Gass, A. J. Papworth, P. J. Goodhew, P. Singh, P. Ruterana, H. K. Cho, R. J. Choi, and H. J. Lee. V-defects and dislocations in InGaN/GaN heterostructures. *Thin Solid Films*, 479(1-2):316–320, 2005.

[61] Jaekyun Kim, Joosung Kim, Youngjo Tak, Suhee Chae, Jun Youn Kim, and Youngsoo Park. Effect of v-shaped pit size on the reverse leakage current of InGaN/GaN light-emitting diodes. *IEEE Electron Device Letters*, 34(11):1409–1411, 2013.

[62] Yufeng Li, Weihan Tang, Ye Zhang, Maofeng Guo, Qiang Li, and Xilin Su. Nanoscale characterization of v-defect in ingan / gan qws leds using near-field scanning optical microscopy. *Nanomaterials*, 9(633), 2019.

[63] Jianli Zhang, Xiaolan Wang, Junlin Liu, Chunlan Mo, Xiaoming Wu, and Guangxu Wang. Study on Carrier transportation in InGaN based green LEDs with V-pits structure in the active region. *Optical Materials*, 86(September):46–50, 2018.

[64] M. Shiojiri, C. C. Chuo, J. T. Hsu, J. R. Yang, and H. Saijo. Structure and formation

mechanism of V defects in multiple InGaN/GaN quantum well layers. *Journal of Applied Physics*, 99(7), 2006.

[65] Fengyi Jiang, J Ianli Z Hang, L X U Ongquan, J I E D Ing, G Uangxu W Ang, X W U Iaoming, X Iaolan W Ang, C M O Hunlan, Z Hijue Q Uan, X I N G G Uo, C Hangda Z Heng, S Huan P An, and J Unlin L Iu. Efficient InGaN-based yellow-light-emitting diodes. *Photonics Research*, 7(2):144–148, 2019.

[66] Shuji Nakamura, Yasuhiro Harada, and Masayuki Seno. Novel metalorganic chemical vapor deposition system for GaN growth. *Applied Physics Letters*, 58(18):2021–2023, 1991.

[67] D.H. Kang, Jae Chul Song, Dong Wook Kim, J.S. Kim, Kannappan Santhakumar, and Cheul Ro Lee. Growth and Evaluation of GaN Grown on Patterned Sapphire Substrates. *Advanced Materials Research*, 29-30:351–354, 2009.

[68] C. Haller, J. F. Carlin, G. Jacopin, D. Martin, R. Butté, and N. Grandjean. Burying non-radiative defects in InGaN underlayer to increase InGaN/GaN quantum well efficiency. *Applied Physics Letters*, 111(26), 2017.

[69] Abdullah. I. Alhassan, Nathan. G. Young, Robert. M. Farrell, Christopher. Pynn, Feng. Wu, Ahmed. Y. Alyamani, Shuji Nakamura, Steven. P. DenBaars, and James. S. Speck. Development of high performance green c-plane III-nitride light-emitting diodes. *Optics Express*, 26(5):5591, 2018.

[70] Tsung Jui Yang, Ravi Shivaraman, James S. Speck, and Yuh Renn Wu. The influence

of random indium alloy fluctuations in indium gallium nitride quantum wells on the device behavior. *Journal of Applied Physics*, 116(11), 2014.

[71] Marcel Filoche, Marco Piccardo, Yuh Renn Wu, Chi Kang Li, Claude Weisbuch, and Svitlana Mayboroda. Localization landscape theory of disorder in semiconductors. I. Theory and modeling. *Physical Review B*, 95(14):1–18, 2017.

[72] Marco Piccardo, Chi Kang Li, Yuh Renn Wu, James S. Speck, Bastien Bonef, Robert M. Farrell, Marcel Filoche, Lucio Martinelli, Jacques Peretti, and Claude Weisbuch. Localization landscape theory of disorder in semiconductors. II. Urbach tails of disordered quantum well layers. *Physical Review B*, 95(14):1–12, 2017.

[73] S. Keller, S. F. Chichibu, M. S. Minsky, E. Hu, U. K. Mishra, and S. P. DenBaars. Effect of the growth rate and the barrier doping on the morphology and the properties of InGaN/GaN quantum wells. *Journal of Crystal Growth*, 195(1-4):258–264, 1998.

[74] L. W. Wu, S. J. Chang, T. C. Wen, Y. K. Su, J. F. Chen, W. C. Lai, C. H. Kuo, C. H. Chen, and J. K. Sheu. Influence of Si-doping on the characteristics of InGaN-GaN multiple quantum-well blue light emitting diodes. *IEEE Journal of Quantum Electronics*, 38(5):446–450, 2002.

[75] Eun Hyun Park, David Nicol Hun Kang, Ian T. Ferguson, Soo Kun Jeon, Joong Seo Park, and Tae Kyung Yoo. The effect of silicon doping in the selected barrier on the electroluminescence of InGaN/GaN multiquantum well light emitting diode. *Applied Physics Letters*, 90(3):1–4, 2007.

[76] Kenji Uchida, Tao Tang, Shigeo Goto, Tomoyoshi Mishima, Atsuko Niwa, and Jun Gotoh. Spiral growth of InGaN/InGaN quantum wells due to Si doping in the barrier layers. *Applied Physics Letters*, 74(8):1153–1155, 1999.

[77] T. Wang, H. Saeki, J. Bai, T. Shirahama, M. Lachab, S. Sakai, and P. Eliseev. Effect of silicon doping on the optical and transport properties of InGaN/GaN multiple-quantum-well structures. *Applied Physics Letters*, 76(13):1737–1739, 2000.

[78] Daesung Kang, Jeong-Tak Oh, June-O Song, Tae-Yeon Seong, Michael Kneissl, and Hiroshi Amano. Hole injection mechanism in the quantum wells of blue light emitting diode with V pits for micro-display application. *Applied Physics Express*, pages 0–9, 2019.

[79] Shengjun Zhou, Xingtong Liu, Han Yan, Yilin Gao, Haohao Xu, Jie Zhao, and Zhijue Quan. The effect of nanometre-scale V-pits on electronic and optical properties and efficiency droop of diodes. *Scientific Reports*, (February):1–12, 2018.

[80] Mi Hyang Sheen, Sung Dae Kim, Jong Hwan Lee, Jong In Shim, and Young Woon Kim. V-pits as Barriers to Diffusion of Carriers in InGaN/GaN Quantum Wells. *Journal of Electronic Materials*, 44(11):4134–4138, 2015.

[81] Hongjian Li, Matthew S Wong, Michel Khoury, Bastien Bonef, Haojun Zhang, YiChao Chow, Panpan Li, Jared Kearns, Aidan A Taylor, Philippe De Mierry, et al. Study of efficient semipolar (11-22) ingan green micro-light-emitting diodes on high-quality (11-22) gan/sapphire template. *Optics Express*, 27(17):24154–24160, 2019.

[82] Jong-Il Hwang, Rei Hashimoto, Shinji Saito, and Shinya Nunoue. Development of ingan-based red led grown on (0001) polar surface. *Applied Physics Express*, 7(7):071003, 2014.

[83] Theeradetch Detchprohm, Mingwei Zhu, Yufeng Li, Liang Zhao, Shi You, Christian Wetzel, Edward A Preble, Tanya Paskova, and Drew Hanser. Wavelength-stable cyan and green light emitting diodes on nonpolar m-plane gan bulk substrates. *Applied Physics Letters*, 96(5):051101, 2010.

[84] A Dussaigne, B Damilano, N Grandjean, and J Massies. In surface segregation in ingan/gan quantum wells. *Journal of Crystal Growth*, 251(1-4):471–475, 2003.

[85] Jin Seo Im, H Kollmer, J Off, A Sohmer, F Scholz, and A Hangleiter. Reduction of oscillator strength due to piezoelectric fields in g a n/a l x ga 1- x n quantum wells. *Physical Review B*, 57(16):R9435, 1998.

[86] Yuji Zhao, Shinichi Tanaka, Qimin Yan, Chia-Yen Huang, Roy B Chung, Chih-Chien Pan, Kenji Fujito, Daniel Feezell, Chris G Van de Walle, James S Speck, et al. High optical polarization ratio from semipolar (20 2¯ 1¯) blue-green ingan/gan light-emitting diodes. *Applied Physics Letters*, 99(5):051109, 2011.

[87] Hongjian Li, Michel Khoury, Bastien Bonef, Abdullah I Alhassan, Asad Jahangir Mughal, Ezzah Azimah, Muhammad EA Samsudin, Philippe De Mierry, Shuji Nakamura, James Speck, et al. Efficient semipolar (11-22) 550 nm yellow/green ingan

light-emitting diodes on low defect density (11-22) gan/sapphire templates. *ACS Applied Materials & Interfaces*, 9(41):36417–36422, 2017.

[88] Michel Khoury, Hongjian Li, Panpan Li, Yi Chao Chow, Bastien Bonef, Haojun Zhang, Matthew S Wong, Sergio Pinna, Jie Song, Joowon Choi, et al. Polarized monolithic white semipolar (20–21) ingan light-emitting diodes grown on high quality (20–21) gan/sapphire templates and its application to visible light communication. *Nano Energy*, 67:104236, 2020.

[89] Michel Khoury, Hongjian Li, Haojun Zhang, Bastien Bonef, Matthew S Wong, Feng Wu, Daniel Cohen, Philippe De Mierry, Philippe Vennegues, James S Speck, et al. Demonstration of electrically injected semipolar laser diodes grown on low-cost and scalable sapphire substrates. *ACS applied materials & interfaces*, 11(50):47106–47111, 2019.

[90] Matthew S. Wong, Jared A. Kearns, Changmin Lee, Jordan M. Smith, Cheyenne Lynsky, Guillaume Lheureux, Hyoshik Choi, Jinwan Kim, Chaehon Kim, Shuji Nakamura, James S. Speck, and Steven P. DenBaars. Improved performance of AlGaInP red micro-light-emitting diodes with sidewall treatments. *Optics Express*, 28(4):5787, 2020.

[91] Matthew S. Wong, David Hwang, Abdullah I. Alhassan, Changmin Lee, Ryan Ley, Shuji Nakamura, and Steven P. DenBaars. High efficiency of III-nitride micro-light-emitting diodes by sidewall passivation using atomic layer deposition. *Optics Express*, 26(16):21324, 2018.

[92] Ryan T. Ley, Jordan M. Smith, Matthew S. Wong, Tal Margalith, Shuji Nakamura, Steven P. Denbaars, and Michael J. Gordon. Revealing the importance of light extraction efficiency in InGaN/GaN microLEDs via chemical treatment and dielectric passivation. *Applied Physics Letters*, 116(25), 2020.

[93] Matthew S. Wong, Changmin Lee, Daniel J. Myers, David Hwang, Jared A. Kearns, Thomas Li, James S. Speck, Shuji Nakamura, and Steven P. Denbaars. Size-independent peak efficiency of III-nitride micro-light-emitting-diodes using chemical treatment and sidewall passivation. *Applied Physics Express*, 12(9), 2019.

[94] David Hwang, Asad Mughal, Christopher D. Pynn, Shuji Nakamura, and Steven P. DenBaars. Sustained high external quantum efficiency in ultrasmall blue III-nitride micro-LEDs. *Applied Physics Express*, 10(3), 2017.

[95] François Olivier, Sauveur Tirano, Ludovic Dupré, Bernard Aventurier, Christophe Largeron, and François Templier. Influence of size-reduction on the performances of GaN-based micro-LEDs for display application. *Journal of Luminescence*, 191:112–116, 2017.

[96] Y. Robin, M. Pristovsek, H. Amano, F. Oehler, R. A. Oliver, and C. J. Humphreys. What is red? on the chromaticity of orange-red InGaN/GaN based LEDs. *Journal of Applied Physics*, 124(18), 2018.

[97] R. W. G Hunt and M.R. Pointer. *Measuring Colour*. John Wiley & Sons, The Atrium, Southern Gate, Chichester, West Sussex, PO19 8SQ, United Kingdom, 4 edition, 2011.

[98] Fred Schubert. *LEDs 2nd Edition*. Cambridge University Press, New York, 2 edition, 2006.

[99] Yu Ho Won, Oul Cho, Taehyung Kim, Dae Young Chung, Taehee Kim, Heejae Chung, Hyosook Jang, Junho Lee, Dongho Kim, and Eunjoo Jang. Highly efficient and stable InP/ZnSe/ZnS quantum dot light-emitting diodes. *Nature*, 575(7784):634–638, 2019.

[100] Hai Wei Chen, Jiun Haw Lee, Bo Yen Lin, Stanley Chen, and Shin Tson Wu. Liquid crystal display and organic light-emitting diode display: present status and future perspectives. *Light: Science and Applications*, 7(3):17168, 2018.

[101] Yong Gon Seo, Kwang Hyeon Baik, Hooyoung Song, Ji-Su Son, Kyunghwan Oh, and Sung-Min Hwang. Orange a-plane InGaN/GaN light-emitting diodes grown on r-plane sapphire substrates. *Optics Express*, 19(14):12919, 2011.

[102] Chan Hyoung Oh, Jong In Shim, and Dong Soo Shin. Current- And temperature-dependent efficiency droops in InGaN-based blue and AlGaInP-based red light-emitting diodes. *Japanese Journal of Applied Physics*, 58(SC), 2019.

[103] Daisuke Iida, Zhe Zhuang, Pavel Kirilenko, Martin Velazquez-Rizo, and Kazuhiro Ohkawa. Demonstration of low forward voltage InGaN-based red LEDs. *Applied Physics Express*, 13(3), 2020.

[104] Yuji Zhao, Sang Ho Oh, Feng Wu, Yoshinobu Kawaguchi, Shinichi Tanaka, Kenji Fujito, James S. Speck, Steven P. DenBaars, and Shuji Nakamura. Green semipolar

(2021) InGaN light-emitting diodes with small wavelength shift and narrow spectral linewidth. *Applied Physics Express*, 6(6), 2013.

[105] Abdullah I. Alhassan, Robert M. Farrell, Burhan Saifaddin, Asad Mughal, Feng Wu, Steven P. DenBaars, Shuji Nakamura, and James S. Speck. High luminous efficacy green light-emitting diodes with AlGaN cap layer. *Optics Express*, 24(16):17868, 2016.

[106] Zi Hui Zhang, Swee Tiam Tan, Zhengang Ju, Wei Liu, Yun Ji, Zabu Kyaw, Yilmaz Dikme, Xiao Wei Sun, and Hilmi Volkan Demir. On the effect of step-doped quantum barriers in InGaN/GaN light emitting diodes. *IEEE/OSA Journal of Display Technology*, 9(4):226–233, 2013.

[107] Shubhra S. Pasayat, Chirag Gupta, Matthew S. Wong, Yifan Wang, Shuji Nakamura, Steven P. Denbaars, Stacia Keller, and Umesh K. Mishra. Growth of strain-relaxed InGaN on micrometer-sized patterned compliant GaN pseudo-substrates. *Applied Physics Letters*, 116(11), 2020.

[108] A Dussaigne, F Barbier, B Samuel, A Even, R Templier, F Lévy, O Ledoux, M Rozhavskaia, and D Sotta. Strongly reduced v pit density on inganos substrate by using ingan/gan superlattice. *Journal of Crystal Growth*, page 125481, 2020.

[109] J Däubler, T Passow, R Aidam, K Köhler, L Kirste, M Kunzer, and J Wagner. Long wavelength emitting gainn quantum wells on metamorphic gainn buffer layers with enlarged in-plane lattice parameter. *Applied Physics Letters*, 105(11):111111, 2014.

[110] B. Aspar, M. Bruel, M. Zussy, and A. M. Cartier. Transfer of structured and patterned thin silicon films using the Smart-cut® process. *Electronics Letters*, 32(21):1985–1986, 1996.

[111] K Pantzas, Y El Gmili, J Dickerson, S Gautier, L Largeau, O Mauguin, G Patriarche, S Suresh, T Moudakir, C Bishop, et al. Semibulk ingan: A novel approach for thick, single phase, epitaxial ingan layers grown by movpe. *Journal of Crystal Growth*, 370:57–62, 2013.

[112] D. Van Den Broeck, D. Bharrat, Z. Liu, N. A. El-Masry, and S. M. Bedair. Characterization of high-quality, relaxed inyga1yn templates for optoelectronic applications. *Journal of Electronic Materials*, 44:4161–4166, 2015.

[113] Michel Khoury, Olivier Tottereau, Guy Feuillet, Philippe Vennéguès, and Jesus Zúñiga-Pérez. Evolution and prevention of meltback etching: Case study of semipolar gan growth on patterned silicon substrates. *Journal of Applied Physics*, 122(10):105108, 2017.

[114] O. Schön, B. Schineller, M. Heuken, and R. Beccard. Comparison of hydrogen and nitrogen as carrier gas for movpe growth of gan. *Journal of Crystal Growth*, 189/190:335–339, 1998.

[115] Ryan Christopher White, Michel Khoury, Feng Wu, Stacia Keller, Mariia Rozhavskaia, David Sotta, Shuji Nakamura, and Steven P DenBaars. MOCVD growth of thick V-

pit-free InGaN films on semi-relaxed InGaN substrates. *Semiconductor Science and Technology*, 2020.

[116] Stacia Keller and Steven P. DenBaars. Metalorganic chemical vapor deposition of group III nitrides - A discussion of critical issues. *Journal of Crystal Growth*, 248(SUPPL.):479–486, 2003.

[117] Romain Bouveyron, Mrad Mrad, and Matthew Charles. V-pit pinning at the interface of high and low-temperature gallium nitride growth. *Japanese Journal of Applied Physics*, 58:0–5, 2019.

[118] Cheyenne Lynsky, Ryan C. White, Yi Chao Chow, Wan Ying Ho, Shuji Nakamura, Steven P. DenBaars, and James S. Speck. Role of V-defect density on the performance of III-nitride green LEDs on sapphire substrates. *Journal of Crystal Growth*, 560-561(December 2020):126048, 2021.

[119] Torsten Langer, Andreas Kruse, Fedor Alexej Ketzer, Alexander Schwiegel, Lars Hoffman, Holger Jonen, Heiko Bremers, Uwe Rossow, and Andreas Hangleiter. Origin of the "green gap": Increasing nonradiative recombination in indium-rich GaInN/GaN quantum well structures. *Physica Status Solidi (C) Current Topics in Solid State Physics*, 8(7-8):2170–2172, 2011.

[120] Ryan C. White, Michel Khoury, Matthew S. Wong, Hongjian Li, Cheyenne Lynsky, Michael Iza, Stacia Keller, David Sotta, Shuji Nakamura, and Steven P. DenBaars. Realization of III-Nitride c-Plane microLEDs Emitting from 470 to 645 nm on Semi-

Relaxed Substrates Enabled by V-Defect-Free Base Layers. *Crystals*, 11(10):1168, 2021.

[121] K. G. Belyaev, M. V. Rakhlin, V. N. Jmerik, A. M. Mizerov, Ya V. Kuznetsova, M. V. Zamoryanskaya, S. V. Ivanov, and A. A. Toropov. Phase separation in InxGa1-xN (0.10 < x < 0.40). *Physica Status Solidi (C) Current Topics in Solid State Physics*, 10(3):527–531, 2013.

[122] Zhe Zhuang, Daisuke Iida, Martin Velazquez-Rizo, and Kazuhiro Ohkawa. 606-nm InGaN Amber Micro-Light-Emitting Diodes with an On-Wafer External Quantum Efficiency of 0.56%. *IEEE Electron Device Letters*, 42(7):1029–1032, 2021.